NONLINEAR SILICON PHOTONICS: EXTENDING PLATFORMS, CONTROL, AND APPLICATIONS

A Dissertation

Presented to the Faculty of the Graduate School

of Cornell University

in Partial Fulfillment of the Requirements for the Degree of

Doctor of Philosophy

by

Steven Andrew Miller

May 2017

NONLINEAR SILICON PHOTONICS: EXTENDING PLATFORMS, CONTROL, AND APPLICATIONS

Steven Andrew Miller, Ph.D.

Cornell University 2017

Silicon photonics is a revolutionary technology that enables the control of light inside a silicon chip and holds promise to impact many applications from data center optical interconnects to optical sensing and even quantum optics. The tight confinement of light inside these chips greatly enhances light-matter interactions, making this an ideal platform for nonlinear photonics. Recently, microresonator-based Kerr frequency comb generation has become a prevalent emerging field, enabling the generation of a broadband optical pulse train by inputting a low-power continuous-wave laser into a low-loss chip-scale microcavity. These chip-scale combs have a wide variety of applications, including optical clocks, optical spectroscopy, and data communications. Several important applications in biological, chemical and atmospheric areas require combs generated in the visible and mid-infrared wavelength ranges, where there has been far less research and development compared with the near-infrared. Additionally, most platforms widely for combs are passive, limiting the ability to control and optimize the frequency combs.

In this dissertation, we set out to address these shortcomings and introduce new tunability as well as wavelength flexibility in order to enable new applications for microresonator frequency combs. The silicon nitride platform for near-infrared combs is generally a passive platform with limited tuning capabilities. We overcome dispersion limitations in the visible range by leveraging the

second-order nonlinearity of silicon nitride and demonstrate visible comb lines. We then further investigate the second-order nonlinearity of silicon nitride by measuring the linear electro-optic effect, a potential tuning mechanism. Finally, we introduce thermal tuning onto the silicon nitride platform and demonstrate tuning of the resonance extinction and dispersion of a micro-cavity using a coupled cavity design. We also address the silicon mid-infrared frequency comb platform. The transparency range of the traditional silicon platform prohibits operation beyond 4 μm wavelength. Here we show that a silicon photonics platform can be leveraged for broadband mid-infrared operation without introducing complexity in fabrication. Both an air-clad and fully suspended silicon platform can enable broadband, low-loss propagation and comb generation as high as 6 μm. We demonstrate a high quality factor resonator near 4 μm wavelength, more than an order of magnitude higher than the traditional platform. Finally, we discuss future avenues of research building on the work presented here.

BIOGRAPHICAL SKETCH

Steven Andrew Miller was born on Long Island in 1989. Growing up, Steven developed a passion for science as well as a passion for music. He began playing the trumpet at age 7, and studied classical and jazz music throughout school and college in addition to his school studies. During this time, he won several regional competitions as well as an international competition. After graduating from high school, Steven attended Hofstra University, where he studied electrical engineering. During this time, he gained experience in a diverse set of areas. He attended a summer school in Denmark on renewable energy, and collaborated on research in wireless communications and biomedical ultrasound. Steven also spent two summers at the NSF Research Experiences for Undergraduates (REU) program in the MIRTHE Center for Mid-Infrared technologies at Princeton University where he worked on environmental sensor networks as well as laser material processing. This experience at Princeton sparked Steven's interest in photonics and led him to pursue this area of graduate study. He graduated summa cum laude from Hofstra University in 2012 with a B.S. in Electrical Engineering and a minor in Mathematics. He then came to Cornell University to pursue his Ph.D. studying integrated photonics under the guidance of Professor Michal Lipson. There, his research has focused on integrated nonlinear optics and microresonator frequency combs. In 2015, Steven moved along with the entire Lipson Nanophotonics Group (formerly Cornell Nanophotonics Group) from Ithaca to Columbia University in the City of New York. At Columbia, Steven has continued his research in developing microresonator frequency combs.

To my parents, Lynn and Douglas, my brother, David, and in memory of my grandmother, Betty Hollenberg.

ACKNOWLEDGEMENTS

First and foremost, I would like to thank my advisor, Professor Michal Lipson. She is a formidable researcher, an incredible role model, and a great advisor. Her positive energy is what I admire most about her, along with her endless creativity and vision. Michal has been the world's leader in her field for more than a decade, and shows no signs of slowing down. Just the opposite actually: after moving to Columbia, it has been incredible to see her moving in so many new and exciting directions. She is essentially superhuman – I'm not sure how she does it. It has been a great privilege to have her as my graduate advisor and absorb some of the qualities that set her apart from the rest.

I would also like to thank the other members of my committee, Professor Alexander Gaeta and Professor Ehsan Afshari. Alex has been an inspiration as an amazing physicist and person. Ehsan has given me a different perspective outside of optics which is very valuable. I have had the privilege of collaborating with Dr. Paul Chevalier from the research group of Professor Federico Capasso, and Dr. Boris Desiatov from the research group of Professor Marko Loncar at Harvard University. They have provided their insights as well as aided in experiments with their mid-IR quantum cascade lasers.

I would like to thank the funding sources that have contributed to this work, including the National Science Foundation Graduate Research Fellowship (NSF GRF), the Cornell University Jacobs Fellowship, the Defense Advanced Research Projects Agency (DARPA), the Intelligence Advanced Research Projects Agency (IARPA), the Air Force Office of Scientific Research (AFOSR), and the Intel Corporation.

I would also like to thank the members of the Gaeta Group, for their close collaboration throughout. In particular, Dr. Yoshitomo Okawachi has taught me

a great deal about frequency combs, and experimentation. Mengjie Yu has been a wonderful colleague and friend to have down in the mid-IR lab. Dr. Michael Lamont developed the early Matlab code for dispersion simulations that have served as a basis for my simulations, as well as frequency comb simulation code. I would also like to thank Dr. Sven Ramelow and Dr. Alessandro Farsi for their establishment of the Quantum Journal Club/Cake Club, a very inviting forum for expanded learning in quantum optics and other interesting special topics.

I am eternally grateful to the amazing members of the Lipson Nanophotonics Group (formerly Cornell Nanophotonics Group) with whom I have had the privilege of working, learning, and growing throughout graduate school. This group is special because it functions somewhat like a family. Coming into the group in my first year, I had very little experience, so I am thankful to these individuals for their generous help. Thank you to Dr. Carl Poitras for your encouragement and for saving the day all the time to keep things running so smoothly. Thank you to Dr. Lian-Wee Luo, Dr. Bishu Guha, Dr. Mian Zhang, Dr. Raphael St. Gelais, Dr. Mohammad Soltani, Dr. Shreyas Shah, Dr. Yoon Ho Daniel Lee and Dr. Mohamad Amin Tadayon for being a huge inspiration for me as insightful, creative scientists. Special thanks goes to Dr. Lawrence Tzuang for helping me ramp up in the beginning, for insightful discussions that taught me so much, and for playing some great music together. A special thanks also goes to Dr. Austin Griffith for laying the groundwork for our mid-IR work as well as always being someone I could discuss research with, help with simulations, or have some espresso. To Romy Fain, my fellow batch mate, it has been a great ride, and a pleasure to have shared this experience with you. To Avik Dutt, you've always been someone I can count on for advice on simulations, fundamental physics discussions and lab experiments. Your puns are also

second-to-none. To Chris Phare, you are an immense source of knowledge, and your deep intuition of physics and engineering has taught me a great deal. To Gaurang Bhatt, thank you for all our discussions on science, music, philosophy, and life in general. I would also like to thank all other current lab mates, Brian Stern, Moshe Zadka, Ipshita Datta, William Ji, Oscar Jimenez, Brian Lee, Euijae Shim, Dr. Tong Lin, Dr. You-Chia Chang, Dr. Samantha Roberts, and Dr. Utsav Dave for the pleasure of sharing learning and working alongside all of you.

There are a few individuals who have impacted my life the most during graduate school, and to whom I am forever indebted. First is Dr. Jaime Cardenas. He has taught me an incredible amount about fabrication as well as a great deal about integrated photonics. Without him, this group would not be what it is today. Jaime's keen intuition and incredible level of creativity have made him an amazing role model for me throughout graduate school as well as everyone who has overlapped with him in the group. Discussions and debates with Jaime around the office have always been interesting and informative. In addition, Jaime and his wife, Cecilia, have been wonderful friends and generous hosts for many fantastic group gatherings. Next, I would like to thank Dr. Kevin Luke. You have been one of my closest colleagues as well as one of my very close friends since I first moved to Ithaca. As a fellow silicon nitride guy, you helped me learn the ropes to ramp up in the beginning, and remained someone fantastic to work with who I could always ask for help or advice. You've also shown me an entirely new way of looking at the world, and reinforced the importance of work-life balance. Lastly, I would like to thank Aseema Mohanty. You have become one of my closest friends, someone I can talk to about most anything in work and in life. You've helped me to grow and better understand the world as well as better understand myself.

Finally, I must thank my family and friends for their support throughout my time in graduate school. To my close friends in Ithaca, Dr. Suren Jayasuriya, Howie Joress, Levon Atoyan, Tayyar Rzayev, Ved Gund and Derek Maseloff, you've all been there for fun times, late-night philosophical discussions, and reinforced the importance of work-life balance. I'm finishing graduate school a very different person than when I began in large part due to all of you. To my family, thank you to my parents for their eternal love, support, and encouragement. And last but not least, thank you to my brother, David, who is someone I've always looked up to for inspiration, advice, and support. Words cannot express my love and appreciation for my family, friends, colleagues and mentors who have shaped who I have become and where I am headed. I consider myself lucky to have the privilege of thanking all the people mentioned above, with whose help I have gotten here today.

TABLE OF CONTENTS

CHAPTER 1

INTRODUCTION

1.1 Integrated Silicon Photonics

The field of integrated photonics has enabled unprecedented control of the flow and properties of light at the chip scale. Throughout much of the last two decades, micro and nanofabrication technologies have fueled the enormous growth of this field. Many basic functionalities of integrated photonics stem from free-space optics, which has been developed over the course of several centuries. However, owing to the small length scales that are unique to such devices, there have been many exciting new functionalities that could not have been achieved without developments on an integrated scale. Much of the recent expansion in capabilities have been driven by the prospect of silicon-based, Complementary Metal Oxide Semiconductor (CMOS)-compatible photonics for meeting the demand for high-bandwidth, low-power integrated optical data interconnection for high-performance computing and data centers. Silicon-based photonics takes full advantage of the extensive semiconductor manufacturing infrastructure, enabling the prospect of low-cost chip-scale photonics systems. Particularly throughout the last decade, advancements in photonics for telecommunications and data-communications have led to an expansion into a wide variety of application fields, including chemical and biological sensing, spectroscopy, biomedical imaging, nonlinear optics, quantum optics, opto-genetics, lidar, and display technologies. There is now an extensive and versatile set of building-block components, devices, and materials available as a ”photonics toolbox” that are actively used for these applications. As such, the field has

progressed to the point at which industries have taken up the development of silicon photonics beyond the laboratory to real products. This began in the telecom and datacom industries, and took nearly a decade or more of development before products were ready or near-ready for primetime. We are now at an interesting time in which photonics technologies in other application areas will continue to mature beyond the photonics laboratory into biology and chemistry labs, medical clinics, quantum computers, virtual/augmented reality devices, robotics, and self-driving cars.

1.2 Nonlinear Optics

Nonlinear optics is the study of nonlinear light-matter interactions and the resulting phenomena, including the generation of new frequencies (colors) of light, ultra-short pulses and photon-photon interactions, among others. In the majority of light-matter interactions that occur in our daily lives, light transmits through, diffracts, scatters, reflects off, or is absorbed by objects in a linear fashion. These interactions can affect amplitude, phase, propagation direction, and polarization of light, but frequency (wavelength, color) is not affected. Thus, red light that passes through a window doesn't come out blue on the other side. However, under the right conditions, with the right piece of glass, this can actually occur via a nonlinear optical process. All nonlinear optical processes require several necessary conditions, first of which is a high optical intensity. The invention of the laser was therefore a critical point for the field of nonlinear optics, as lasers provide a high intensity, coherent beam of light at a single frequency, contrasting the incoherent broadband emission from thermal light sources. Pulsed lasers provide even higher peak intensities than continuous wave lasers, and

are thus ubiquitous in the field. Optical intensity is equal to the power per unit area of a beam, so technologies such as optical fibers and integrated optics that tightly confine light are valuable tools that have enabled demonstrations of many new phenomena. In general, high powered, pulsed lasers require expensive technologies, which somewhat limits the scope of research and applications of nonlinear optics. However, fiber and integrated photonics can enable nonlinear optics using low-power, continuous wave lasers, thus allowing for more fundamental research as well as development of real-world applications.

One such development will be the focus of this dissertation: microresonator optical frequency combs. This research area has enabled a way of generating a frequency comb spectrum, corresponding to short pulses in time, by using a relatively low power continuous wave laser source and a photonic micro-chip. The development of these devices has great potential for applications in optical frequency metrology, optical clocks, optical spectroscopy, arbitrary waveform generation, astronomical calibration, as well as telecommunications. Both the understanding of physical dynamics as well as functionality and experimental quality of these frequency combs have progressed significantly in the past several years. Further research is needed to expand the wavelength span as well as wavelength range of these frequency combs for applications of octave spanning frequency combs in the visible, near-IR, and mid-IR range.

1.3 Organization

This dissertation focuses on the advancement of microresonator frequency combs both in wavelength range and functionality, enabling a wider array of

applications as well as more versatile capabilities. Chapters 2 and 3 present a background context for the following work, and offer intuitive explanations of many concepts to enable a deeper understanding. In Chapter 2, we introduce the fundamental principles of integrated photonics. We introduce the concepts of propagating waveguide modes as well as resonators. An overview of the characteristics of relevant materials and wavelength regimes is also explored for broader context. The basic fabrication methods for devices described in subsequent Chapters are also outlined. We conclude with the idea that integrated optics is an ideal platform for nonlinear optics. Thus, Chapter 3 offers an overview of nonlinear optics in the context of waveguide optics. Nonlinear refraction and wave mixing are explored, leading to the generation of Kerr frequency combs. In Chapter 4, we introduce microresonator frequency comb generation at visible wavelengths via a simultaneous second-order nonlinear process in silicon nitride waveguides. We further explore the second-order nonlinear electro-optic properties of silicon nitride in Chapter 5. We then introduce tunability to the silicon nitride frequency comb generation platform based on coupled microring resonators and integrated thermal tuning in Chapter 6. Finally, we explore two ways to extend the traditional silicon-on-insulator platform for broadband mid-infrared frequency comb generation. In Chapter 7, we demonstrate a low-loss air-clad silicon microresonator, and in Chapter 8 we explore a fully suspended silicon waveguide platform. We conclude with a summary in Chapter 9, and address several future research directions that can build upon the work presented in this dissertation.

CHAPTER 2

INTEGRATED PHOTONICS

2.1 Waveguides

2.1.1 High Index Contrast Waveguides

Silicon photonics is based on high-index contrast waveguides, as in Fig. 2.1(a), in which a high refractive index dielectric core material (e.g. silicon) is surrounded by a low refractive index dielectric cladding material (e.g. silicon dioxide, SiO_2). In a ray-optics picture, the structure in Fig 2.1(b). acts as a waveguide because as light travels from a high-index to a low-index medium at a sufficiently shallow incidence angle, *total internal reflection* occurs, such that light reflects at the interface and remains confined within the high-index medium. As long as the angle remains below the critical angle, $\theta_{cr} = \arcsin(n_2/n_1)$, the high-index medium acts to guide the light. This is the basic principle behind optical fibers as well as integrated photonic waveguides; however, fibers have an index contrast much less than 1, whereas silicon waveguides exhibit a high index contrast of nearly $3:1$.

Such a waveguide can also be understood from a mode picture, which remains a common theme throughout this text. One can solve the wave equation given the standard boundary conditions of the core/cladding refractive indices. A set of solutions arise having distinct eigenvalues, commonly referred to as "modes," each exhibiting their own effective refractive index, n_{eff}. The n_{eff} falls between the core and cladding indices, and can be thought of as an indicator

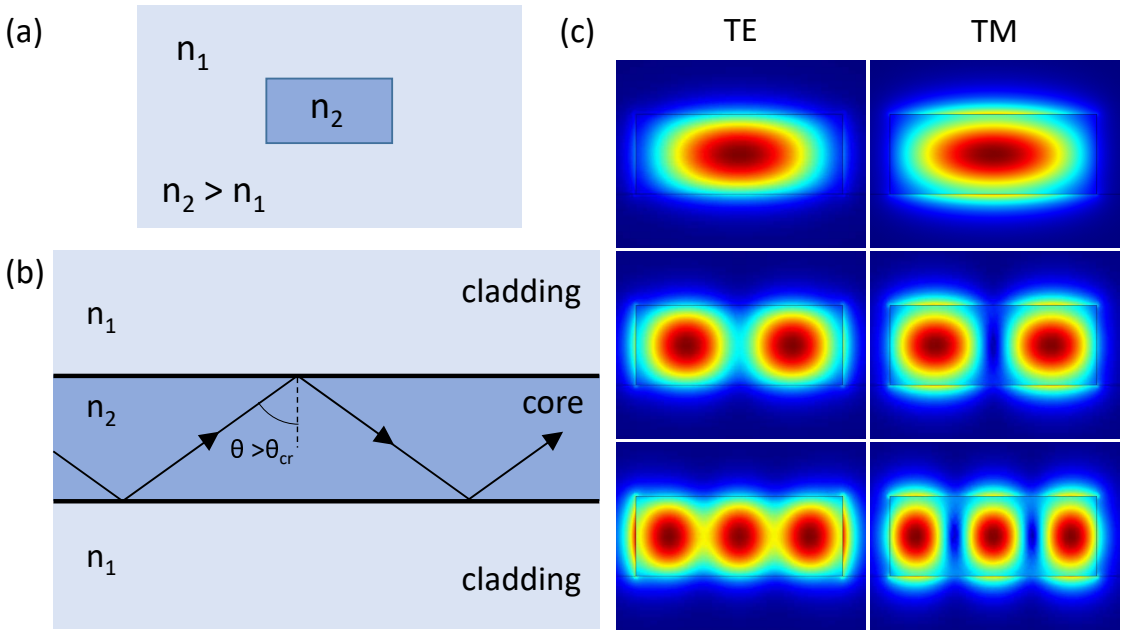

Figure 2.1: (a) Cross-section of a high index contrast waveguide, in which light is confined within a high-index core embedded within a low-index cladding material. (b) Ray-optics picture of a 2D slab waveguide. Light rays experience total internal reflection at the core-cladding boundary if their angle exceeds the critical angle, θ_{cr}. (c) Fundamental and first two higher-order modes for both TE and TM polarizations.

of the degree of light confinement. The fundamental and first few higher-order modes for transverse-electric (TE) and transverse-magnetic (TM) polarizations are shown in Fig. 2.1(c) from a finite-element method (FEM) simulation using COMSOL Multiphysics Software. The fundamental mode consists of a peak intensity in the center of the waveguide, a discontinuity at two interfaces (due to the discontinuous electric field boundary condition for a field normal to an interface), and an evanescent tail that exponentially decays beyond the waveguide core. Higher order modes are similar, but exhibit different numbers of peak intensity lobes within the core. The fundamental mode has the highest degree of confinement and thus exhibits the highest n_{eff}, which decreases for each

successive higher-order mode.

Several distinct properties arise from having a high index contrast. First, the higher the index contrast, the more tightly confined the light is inside the waveguide; this means the waveguide size can decrease somewhat below the wavelength of the light while still maintaining light confinement, which allows integrated waveguides to shrink down from the size of fibers (tens to hundreds of μm) down to the chip-scale (hundreds of nanometers). Tight confinement also creates a higher light intensity in the waveguide (since intensity is optical power per unit cross-sectional area), as well as decreases the strength of the evanescent tail, and allows for tighter waveguide bend radii without light leaking out. Second, high index contrast waveguides can exhibit a strong change in refractive index across different wavelengths, enabling dispersion engineering, which will be discussed in Chapter 3.8. Third, high index contrast means the n_{eff} of higher order modes are very well separated apart compared to fibers, enabling multi-mode waveguides to be used for many applications. Unfortunately, waveguide scattering loss due to sidewall roughness increases with high index contrast because the high-contrast roughness acts as a stronger perturbation to the waveguide mode than low-contrast roughness. Overall, high-index contrast is one of the most important fundamental properties of silicon photonics which enables the operation of almost all silicon photonic devices.

2.1.2 Waveguide Propagation

Light propagates through a high index contrast waveguide as a transverse wave. Modes exist with primarily TE as well as primarily TM fields, however,

particularly for high index contrast waveguides, a "TE" mode has small components of E_y and E_z fields as well as the primary E_x field. These modes propagate with phase velocity, v_p given by:

$$v_\mathrm{p} = \frac{c}{n_\mathrm{eff}}, \tag{2.1}$$

in which c is the speed of light in a vacuum, and group velocity, v_g given by:

$$v_\mathrm{g} = \frac{c}{n_\mathrm{g}}, \tag{2.2}$$

in which n_g is the group index:

$$n_\mathrm{g} = n + \omega\frac{\mathrm{d}n}{\mathrm{d}\omega} = n - \lambda\frac{\mathrm{d}n}{\mathrm{d}\lambda}. \tag{2.3}$$

Most materials are dispersive, such that the refractive index changes across wavelength, leading to changes in phase and group velocities across wavelength spectrum. The waveguide geometry also induces its own dispersion affecting the light propagation. This is of significant importance for nonlinear optical processes, and is further discussed in Chapter 3.7.

2.1.3 Modes and Mode Coupling

Mode coupling is a fundamental tool in integrated photonics, and it is instructive to further understand modes in some detail. A forward-propagating mode inside an isolated waveguide is orthogonal to all other waveguide modes, meaning it has zero mode overlap with other modes and cannot interact with other modes without some external mediation. If, however, a small perturbation is introduced, orthogonality can be broken and coupling can occur. For

a propagating waveguide mode, this perturbation could be any change in refractive index, such as a small notch in the side of the waveguide, or even another waveguide introduced some lateral distance away which overlaps with its evanescent tail. When orthogonality is broken and coupling occurs, energy is transferred between these modes. These coupled modes are no longer orthogonal; however, a different set of orthogonal mode solutions exist, commonly referred to as superposition modes, or *supermodes*, which will be discussed below.

If we consider waves propagating with propagation constants β_a and β_b in the absence of coupling, they satisfy the equations:

$$\begin{aligned} \frac{\mathrm{d}A_a}{\mathrm{d}z} &= -j\beta_a A_a \\ \frac{\mathrm{d}A_b}{\mathrm{d}z} &= -j\beta_b A_b, \end{aligned} \tag{2.4}$$

which simply describe each wave, A_i, propagating in the $+z$ direction accumulating phase with their respective propagation constants. If a mutual coupling mechanism is introduced between these modes, the equations become:

$$\begin{aligned} \frac{\mathrm{d}A_a}{\mathrm{d}z} &= -j\beta_a A_a + \kappa_{ab} A_b \\ \frac{\mathrm{d}A_b}{\mathrm{d}z} &= -j\beta_b A_b + \kappa_{ba} A_a, \end{aligned} \tag{2.5}$$

such that wave A_a is weakly affected by wave A_b and vice versa through mutual coupling strength κ_{ab} (κ_{ba}). A determinant solution to these equations yields the following expression [1]:

$$\beta_{\pm} = \frac{\beta_a + \beta_b}{2} \pm \sqrt{\left(\frac{\beta_a - \beta_b}{2}\right)^2 - \kappa^2} \tag{2.6}$$

in which $\beta_{\pm}$ are the orthogonal superposition modes (supermodes) of the original coupled modes β_a and β_b. These modes, plotted in Fig. 2.2(a), show a char-

acteristic anti-crossing shape. Each individual waveguide mode is shown as dotted lines, which cross each other. However, their mutual coupling creates an avoided crossing (anti-crossing) as the modes couple and hybridize with each other. One supermode is a phase-symmetric superposition [Fig. 2.2(b)] while the other is a phase-anti-symmetric superposition [Fig. 2.2(c)].The coupling strength determines the mode splitting at the center of the anti-crossing.

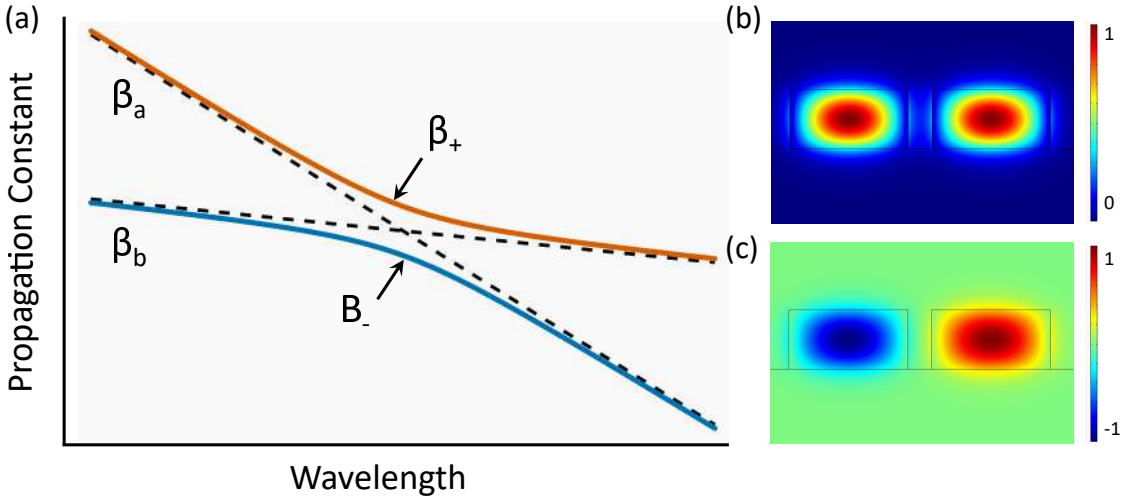

Figure 2.2: Mode Coupling. (a) Anti-crossing behavior of two coupled mode, β_a and β_b. At the center of the anti-crossing, the modes hybridize to form superposition modes (supermodes). These modes are phase symmetric (b) and phase anti-symmetric (c) waveguide modes. Far from the anti-crossing, the hybrid modes behave like individual isolated modes.

Degenerate mode coupling is a common case to consider. If $\beta_a = \beta_b = \beta$ (i.e. two parallel identical waveguides), and we examine the evolution of a wave beginning in waveguide 1, we see a sinusoidal transfer of energy between the two waveguides:

$$A_2 = A_1 \sin^2(\kappa L). \tag{2.7}$$

This energy transfer is periodic along the propagation direction (Fig. 2.3). If we

examine the orthogonal eigenmodes of this coupled waveguide system, we see that Eq. 2.6 reduces to the following:

$$\beta_{\pm} = \beta_{s,as} = \beta \pm \kappa \tag{2.8}$$

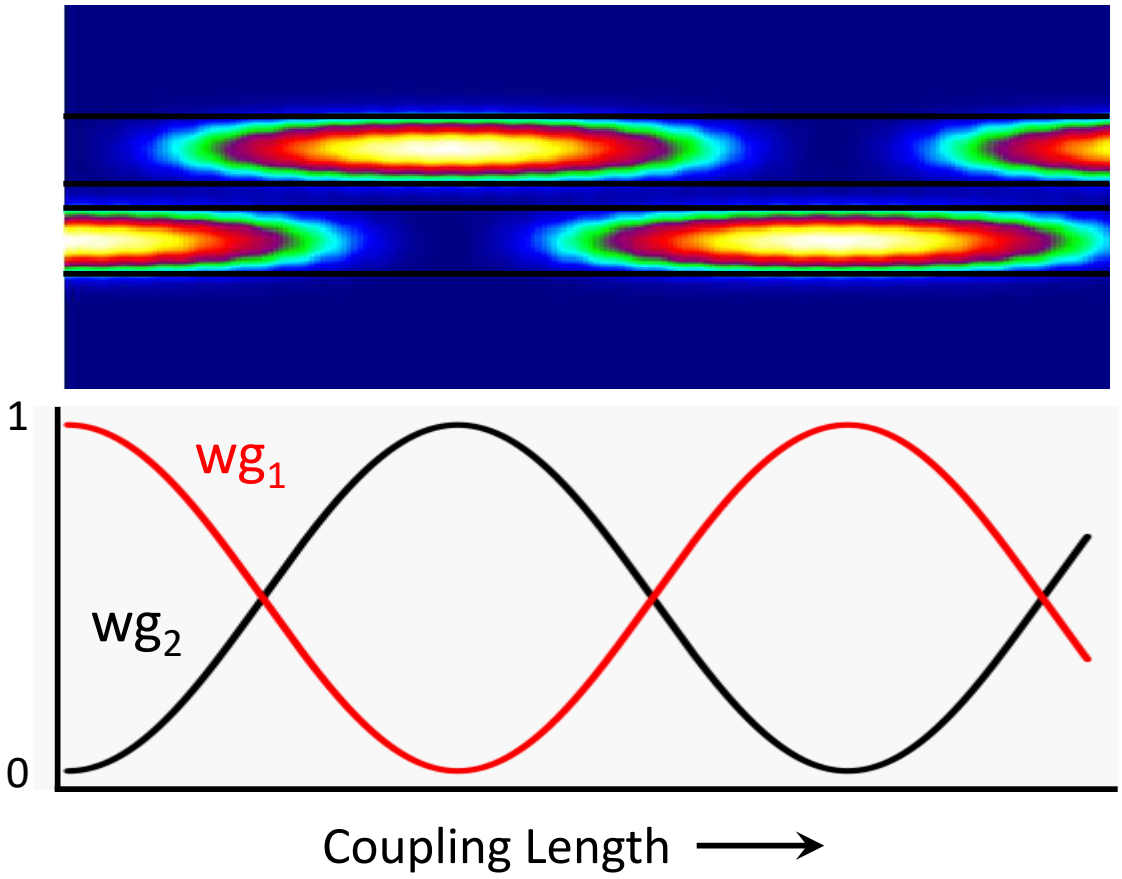

Figure 2.3: Two identical waveguides evanescently coupled to each other exhibit degenerate mode coupling, such that the eigenmodes are the symmetric and antisymmetric supermodes. Light launched into only one waveguide is not the system eigenmode, so light couples back and forth between the two waveguides in a sinusoidal manner

These two modes represent the phase-symmetric and phase-anti-symmetric superpositions of these two degenerate coupled waveguides [Fig. 2.2(b)-(c)]. The

propagation constants of these two supermodes have split, much like the splitting between bonding and anti-bonding energy levels of a hydrogen molecule that is formed by the mutual coupling of two identical hydrogen atoms. This type of coupling is the fundamental principle behind waveguide directional couplers, waveguide interferometers as well as microring resonator coupling. Intuitively, when we launch light into only waveguide 1 in 2.3, this is not the eigenmode of the coupled system, and so there is an exchange of light back and forth between the coupled waveguides. This is the principle behind waveguide directional couplers.

2.2 Resonators

2.2.1 Ring Resonator

The microring resonator is a versatile component of the "photonics toolbox" that is the focus of the devices and studies described in this work. A ring resonator consists of a waveguide wrapped around itself to form a circular traveling-wave ring resonator cavity. A *bus* waveguide is positioned close to the microring such that light evanescently couples into and out of the cavity (Fig. 2.4a). When continuous wave (CW) laser light from the bus waveguide evanescently couples into the ring, the light that makes the round-trip in the cavity interferes with the input bus-waveguide light. Destructive interference occurs when an integer number of wavelengths fit precisely inside the optical path length of the cavity, in which the cavity is said to be "on resonance." Mathematically, this occurs when the condition $2\pi n_{\text{eff}} L = m\lambda$ is met, in which L is the length of the cav-

ity, λ is the resonance wavelength, and m is an integer. Here, the interference causes a dip in bus-waveguide transmission and traps the light inside the ring for several round-trips. This transmission dip is shown in Fig. 2.4b, and forms a characteristic Lorentzian function in the frequency/wavelength domain:

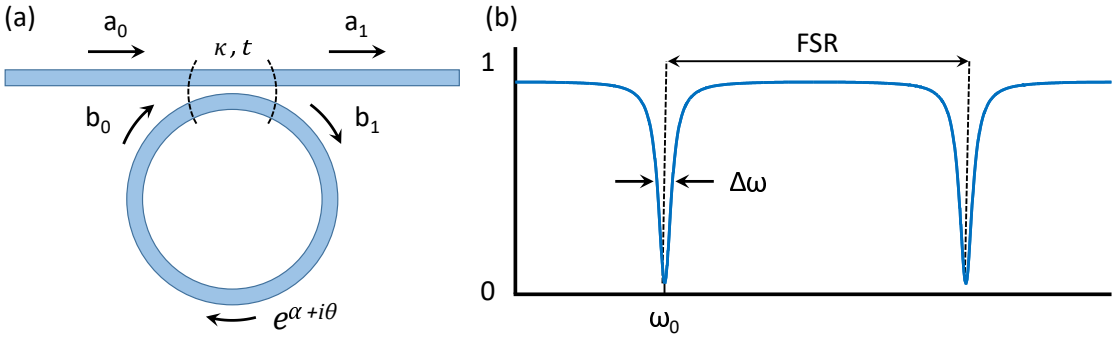

Figure 2.4: (a) General form of a microring resonator coupled to a bus waveguide. (b) Transmission spectrum of microring resonator, showing linewidth, resonance freqeuency, and free spectral range (FSR).

$$T = 1 - \frac{1}{(\omega - \omega_0)^2 + (\Delta\omega/2)^2}, \tag{2.9}$$

in which ω_0 is the resonance frequency and $\Delta\omega$ is the full-width at half maximum (FWHM) resonance linewidth. A series of resonances occur at neighboring wavelengths for consecutive m-number resonant modes. The spacing between consecutive resonances is called the free-spectral range (FSR), and is equal to:

$$\mathrm{FSR}_\omega = \frac{2\pi c}{n_g L}, \tag{2.10}$$

in which L is the cavity length. The width of the Lorentzian lineshape is a measure of the cavity decay rate, which is inverse to the cavity lifetime, τ. The

quality (Q) factor is an important figure-of-merit indicating how much energy is stored in the resonator, and is given by:

$$Q = \frac{\omega}{\Delta\omega} = \omega\tau. \tag{2.11}$$

The cavity Q is directly proportional to the cavity lifetime. The finesse is another important figure-of-merit, measuring the number of round trips light takes inside the cavity, and is given by the ratio of the FSR to the linewidth:

$$F = \frac{\mathrm{FSR}_\omega}{\Delta\omega}. \tag{2.12}$$

The finesse can also be represented simply in terms of the round-trip loss in the cavity:

$$F = \frac{2\pi}{\alpha L} \tag{2.13}$$

in which α is the waveguide propagation loss, and thus αL represents the cavity round-trip loss. The value of finesse, Q, and resonance extinction are determined by the balance between the *rate* of input/output coupling and the intrinsic cavity loss rate. The total cavity loss rate can be expressed as:

$$\gamma_{total} = \frac{1}{\tau_{\mathrm{tot}}} = \frac{1}{\tau_{\mathrm{i}}} + \frac{1}{\tau_{\mathrm{c}}}, \tag{2.14}$$

in which τ_{tot} is the total cavity lifetime, τ_{i} is the intrinsic cavity lifetime due to propagation losses, and τ_{c} is the cavity lifetime due to coupling. By dividing each term in this equation by the resonance angular frequency, ω, we can express this statement in terms of quality factor:

$$\frac{1}{Q_{\mathrm{l}}} = \frac{1}{Q_{\mathrm{i}}} + \frac{1}{Q_{\mathrm{c}}}, \tag{2.15}$$

in which Q_{l} is the total, or "loaded" Q, Q_{i} is intrinsinc Q, and Q_{c} is the coupling Q. Loaded Q is a directly measurable quantity, whereas intrinsic Q is a derived

quantity which is a measure of the propagation loss inside the cavity. Their relation is given by:

$$Q_i = \frac{2\pi n_g}{\alpha\lambda}, \tag{2.16}$$

in which α is the propagation loss per unit length [2].

There are three basic coupling regimes for a cavity to exhibit: under-coupled, critically-coupled, and over-coupled. A cavity is under-coupled if the coupling rate is slower than its intrinsic loss rate (when $Q_c > Q_i$). Here, loaded Q is dominated by the intrinsic losses, and minimal additional loss is introduced by the coupling mechanism. An under-coupled resonance thus has low extinction and sharp linewidth. A cavity is critically-coupled when the coupling rate matches the intrinsic loss rate of the cavity. Here, the intrinsic Q is twice that of the loaded Q. On resonance, complete destructive interference occurs, such that the extinction is maximum, and all light is lost inside the ring. A cavity is over-coupled when the coupling rate exceeds the intrinsic loss rate of the cavity. Here, the loaded Q is dominated by coupling. An over-coupled resonance has low extinction and has a much broader linewidth compared with an under-coupled resonance with the same propagation loss. Experimentally, the intrinsic Q can be calculated from a measured resonance by fitting a Lorentzian function and using the relation:

$$Q_i = \frac{2Q_l}{1 \pm \sqrt{T}}, \tag{2.17}$$

in which T is the transmission on resonance ($T = 0$ for critical coupling). The + sign is used in the denominator for under-coupling, and the − sign is used for over-coupling. Since the intrinsic Q is a measure of propagation loss, it is a critical figure-of-merit when working to achieve low-loss waveguide fabrication. The coupling Q can easily be modified in design by changing the gap

between the bus waveguide and ring, or alternatively introducing a longer coupling length.

Transfer Matrix Approach

The ring resonator can be understood using a transfer matrix approach. A directional coupler with amplitude coupling coefficient, κ, and amplitude transmission coefficient, t, can be represented by a 2×2 matrix:

$$M = \begin{pmatrix} t & i\kappa \\ i\kappa & t \end{pmatrix} \tag{2.18}$$

For satisfying conservation of energy, the total power coupling and transmission must total unity:

$$\kappa^2 + t^2 = 1, \tag{2.19}$$

in which κ^2 is the power coupling coefficient and t^2 is the power transmission coefficient. This transfer matrix holds under the assumptions of reciprocity and time-reversal symmetry. The inputs and outputs of the directional coupler, shown in Fig. 2.4(a), can be obtained by solving the matrix equation:

$$\begin{pmatrix} a_1 \\ b_1 \end{pmatrix} = M \begin{pmatrix} a_0 \\ b_0 \end{pmatrix} \tag{2.20}$$

The input b_0 can be expressed in terms of the output b_1 by introducing a phase and amplitude change from propagation around the ring, such that:

$$b_0 = b_1 e^{-\alpha L + i\theta} \tag{2.21}$$

in which θ is the phase accumulated during one round-trip. Solving Eq. 2.20 analytically for $|a_1|^2$ (transmission power) we obtain:

$$|a_1|^2 = \frac{a^2 + |t|^2 - 2a|t|\cos(\theta)}{1 + a^2|t|^2 - 2a|t|\cos(\theta)}, \tag{2.22}$$

in which a is the power remaining after one round trip, given by:

$$a = e^{-\alpha L} \tag{2.23}$$

The intracavity power ($|b_1|^2$) can also be obtained:

$$|b_1|^2 = \frac{a^2(1 - |t|^2)}{1 + a^2|t|^2 - 2a|t|\cos(\theta)}. \tag{2.24}$$

On resonance, the power transmission is:

$$|b_1|^2 = \frac{(a - |t|)^2}{(1 - a|t|)^2}. \tag{2.25}$$

Critical coupling occurs when $a = |t|$, in which transmission reaches zero on resonance.

2.2.2 Coupled Ring Resonators

Several interesting functionalities arise from coupling multiple microrings to each other. A significant amount of research has gone into coupled rings. A long chain of coupled rings, called a coupled ring optical waveguide (CROW), was first proposed by Yariv in [3]. Such a chain can be used as a higher-order filter to achieve a steep filter roll-off [4]; this is directly analogous to a higher-order analog electronic filter. Additionally, the resonant nature of the coupled

ring chain can cause light to travel at a low group velocity, commonly known as slow light [5]. The same formalism of coupled microrings can also be applied to coupled defect cavities in photonic crystals [3]. Shorter chains of coupled rings have also been studied for different applications, including demonstrations of "photonic molecule" which consists of two coupled rings.

A double-ring structure exhibits characteristics from coupled mode theory, similar to those discussed for two coupled waveguides in Chapter 2.1.3. However, the coupled modes of each microring are resonant modes having a characteristic resonance frequency in addition to spatial modes having a characteristic propagation constant. Therefore, we can analyze this structure in the frequency domain rather than the spatial domain, and observe energy-level mode splitting in the frequency spectrum as opposed to splitting of the k-vector, as discussed above in Chapter 2.1.3. A detailed study of a coupled microring device is discussed in Chapter 6.

A transfer matrix analysis offers significant insights into the functionalities of a double-ring structure. The parameters are defined in Fig. 2.5(a). For this analysis, it is useful to invert the matrices in Eq. 2.20 as follows:

$$\begin{pmatrix} a_0 \\ a_1 \end{pmatrix} = \boldsymbol{M\theta M} \begin{pmatrix} c_0 \\ c_1 \end{pmatrix}. \tag{2.26}$$

in which,

$$\boldsymbol{M} = \begin{pmatrix} \frac{it}{\kappa} & \frac{-i}{\kappa} \\ \frac{i}{\kappa} & \frac{-it}{\kappa} \end{pmatrix} \tag{2.27}$$

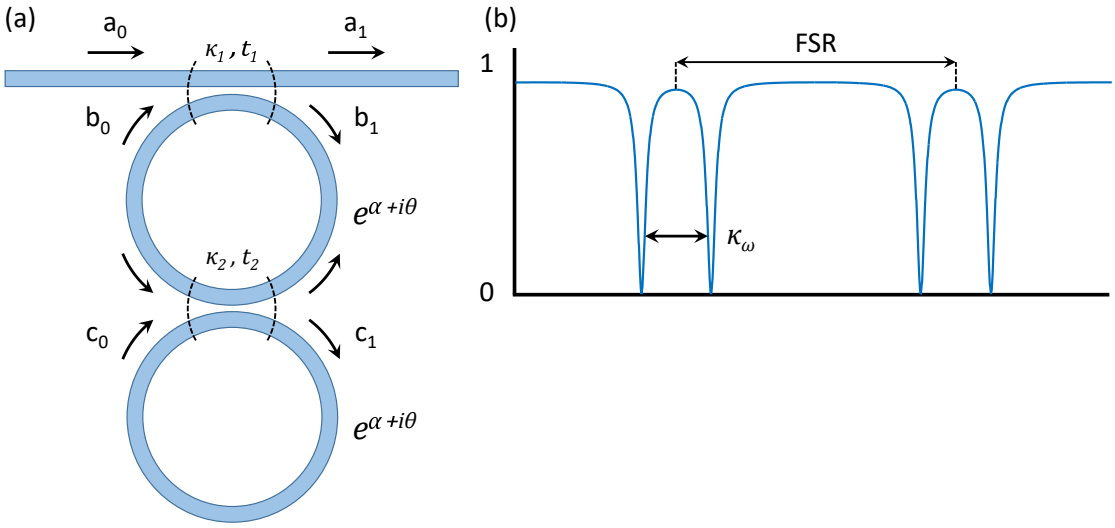

Figure 2.5: (a) General form of a double microring resonator coupled to a bus waveguide. (b) Transmission spectrum of microring resonator, in which the doublet resonance splitting, κ_ω is proportional to the coupling rate between the two microrings ($\propto \kappa_2$).

and,

$$\boldsymbol{\theta} = \begin{pmatrix} 0 & e^{\alpha+i\theta} \\ e^{-\alpha-i\theta} & 0 \end{pmatrix} \tag{2.28}$$

Solving Eq. 2.26, we can solve for transmission power, $|a_1|^2$, as well as intracavity power in ring 1, $|b_1|^2$, and ring 2, $|c_1|^2$. The transmission power is plotted vs. wavelength in Fig 2.5(b), showing a split resonance peak at each FSR corresponding to the supermodes of the coupled-resonator system. A detailed exploration of the functionalities enabled by this coupled ring system for nonlinear optics applications is presented in Chapter 6.

2.3 Materials

Integrated photonics has been developed using many material systems, each exhibiting unique properties useful for many applications. Optical properties including refractive index and absorption, light emission, electro-optic effect, and free-carrier generation are key factors for material choice. Fabrication considerations are also crucial, including process compatibility and material quality. Insulators and semiconductors below their bandgap are optically transparent to varying degrees, and can be leveraged for waveguiding.

Group III-V materials, such as gallium arsenide (GaAs) or indium phosphide (InP), are direct-bandgap semiconductors, meaning they are useful for making lasers and amplifiers. They also exhibit a strong electro-optic effect, in which an applied electrical voltage results in a change in material refractive index. They can therefore be used for high-speed optical switches and modulators. Additionally, operation above the bandgap can enable high speed photodetectors. These materials are epitaxially grown and expensive, and yet are vital to nearly all integrated photonics systems. Nonetheless, they are generally incompatible or have been difficult to integrate along with silicon-based CMOS-compatible materials.

Several additional prominent photonics materials warrant some discussion. Silica is used for integrated photonics as well as ultra-high quality factor microresonators [6–8], and exhibits a transparency from visible through the near-IR. Due to its low index, silica devices are necessarily larger than other materials. Germanium is commonly used for near-IR photodetectors due to its smaller bandgap and compatibility with silicon. Germanium is transparent

from 1700 nm all the way to 15 µm wavelength, making it attractive for mid-IR applications, which have been plagued thus far by material quality issues [9]. Diamond [10], aluminum nitride (AlN) [11], silicon carbide (SiC) [12], and lithium niobate ($LiNbO_3$) [13] are other interesting photonics materials with unique electro-optic, nonlinear, mechanical, and quantum properties that enable novel integrated devices and phenomena. In recent years, 2D materials such as graphene [14], molybdenum disulfide (MoS_2) [15], and boron nitride (BN) [16] have emerged as interesting photonic materials in addition to their well-studied electrical properties. This work focuses on CMOS-compatible material platforms, including silicon and silicon nitride.

2.3.1 Silicon

Silicon is an indirect-bandgap semiconductor (1.1 eV) featuring a high refractive index ($n = 3.47$ at 1550 nm), a high third-order nonlinear coefficient ($n_2 \sim 10^{-18}$) and a high thermo-optic coefficient (TOC = 1×10^{-4}). Its transparency window extends from 1 µm to nearly 8 µm wavelength. In the telecom range, it is widely used for high-speed optical modulators via the free-carrier plasma dispersion effect, in which free carriers controlled by an integrated diode cause a refractive index change. In this range, silicon suffers from detrimental nonlinear effects such as two-photon absorption and self-phase modulation, as well as significant temperature sensitivity. Silicon waveguides have reached propagation losses below 1 dB/cm, and microring quality factors above 10^6 using etchless fabrication techniques (detailed in Chapter 2.5.2) [17,18]. In the visible, silicon is widely used as a photodetector and image sensor. In the mid-IR, silicon is a promising material platform which is discussed in depth in Chapters

7 and 8. Owing to the CMOS industry as well as to its high abundance in the earth's crust, silicon is widely available in extremely high-purity, single crystal wafer form as well as in thin-film silicon on insulator (SOI). SOI is the standard silicon photonic platform, and consists of a thin film of single crystal silicon on top of a thin SiO_2 cladding, which sits on a bulk silicon substrate.

2.3.2 Silicon Nitride

Silicon nitride is a passive dielectric material featuring a relatively high refractive index (2.01 at 1550 nm), high third-order nonlinear coefficient ($n_2 = 2 \times 10^{-19} \mathrm{m}^2/\mathrm{W}$) [19], high mechanical stiffness, and moderate thermo-optic coefficient (TOC = 4×10^{-5}). Its broad transparency window extends from ~250 nm wavelength through the visible, near-IR, and into the mid-IR wavelengths ~6 µm. Silicon nitride has been able to achieve ultra-low losses below 1 dB/m, enabling microring quality factors of nearly 10^8. These high Q's have enabled significant advances in near-IR microresonator frequency combs, as discussed in Chapter 3.9. Additionally, its wide transparency makes it useful for visible applications. Silicon nitride is a deposited material, and can therefore be integrated with other materials, but exhibits a high degree of film stress, which must be addressed in fabrication (discussed in Chapter 2.5).

2.4 Wavelength Regimes

Development of integrated photonics generally began in the near-IR and has later spread outward into both shorter and longer wavelengths to access inter-

esting properties and applications in various wavelength regimes. Generally, the availability of laser sources is the primary fuel for photonics development and application areas.

2.4.1 Near Infrared

Telecom applications for optical interconnectivity fueled the development of extremely low-loss optical fibers and reliable, inexpensive lasers in the near-IR range near 1550 nm, which in turn has driven innovation in integrated photonics. Additionally, microresonator frequency combs were first developed in the near-IR [20]. Other applications include quantum optics [21], biomedical imaging (OCT) [22], and chemical sensing [23].

2.4.2 Mid Infrared

Quantum cascade lasers (QCLs) were invented two decades ago and have fueled developments in integrated mid-IR photonics [24]. The mid-IR is home to a set of optical absorption signatures from the rotational-vibrational energy levels of most common small molecules. These absorption features are unique to each molecule, and are used in many types of mid-IR spectroscopy techniques to optically identify compounds. Many materials begin absorbing strongly in the mid-IR, including SiO_2, so material platforms including crystalline fluorides [25, 26], sapphire [27–35], and chalcogenides [36–40] are commonly implemented.

2.4.3 Visible

The visible range has several unique applications in quantum optics and biology. Highly sensitive single-photon detectors are available at visible wavelengths, making this range ideal for quantum applications. Water has its maximum transparency in the visible range, which is vital to many biological imaging applications. Additionally, opto-genetics involves optical excitation of tagged neurons, which are excited using blue light. One outstanding challenge is that waveguide scattering increases significantly at shorter wavelengths (due to Rayleigh scattering), causing losses to become significant.

2.5 Fabrication

2.5.1 High-Q Silicon Nitride

The fabrication of high-Q silicon nitride devices has been a result of significant developments outlined in [41] and more recently [42]. The process begins with growing a 3-4 µm thermal oxide layer on a virgin silicon wafer to serve as the buried oxide (BOX) under-cladding for the waveguide. Next, a 350 nm layer of stoichiometric silicon nitride is deposited at 800 °C in a low-pressure chemical vapor deposition (LPCVD) furnace. The LPCVD nitride film has a low level of impurities due to its high temperature deposition, but has significant tensile stress, which limits the thickness one can deposit at once before the film cracks. In order to optimize the film quality, a 3 hour nitrogen anneal at 1200 °C is done to diffuse out the trapped hydrogen inside the nitride film. After annealing,

more LPCVD nitride is deposited to the final desired thickness, such as ~700 nm for the devices described in Chapters 4 and 6. The usual nitride thickness limitation was overcome in [42] by scribing trenches before deposition to release the stress and avoid propagation of cracks. Once the film is deposited, we prime the surface with hot piranha acid ($3:1$ H_2SO_4:H_2O_2) followed by Surpass 3000 adhesion promoter, and ma-N 2405 e-beam resist. We pattern waveguides in the ma-N using an electron beam lithography tool and develop using MIF-300 (or MIF-726) developer. We then etch the waveguides in an inductively-coupled plasma reactive ion etcher (ICP-RIE) using a fluorine-based CHF_3/O_2 etching recipe. We then strip the resist and anneal the nitride once more, allowing for hydrogen diffusion from the top half of the deposited film. The anneal is done mid-way as well as at the end in order to improve this out-gassing process; silicon nitride is commonly used as a good diffusion barrier, so outgassing of hydrogen through thinner films yields better results. After anneal, several hundred nanometers of high-temperature silicon dioxide (HTO) are deposited in an LPCVD furnace, followed by more than one micron of plasma-enhanced chemical vapor deposition (PECVD) silicon dioxide to complete the cladding layer. The base of the top-cladding is in direct contact with the optical mode, so a higher-quality HTO is used here. Following this step, metals may be added for active thermal tuning (see Chapter 2.5.3). Additionally, the etched-facet step is done. This process was previously developed and outlined in [43]. Using a thick photoresist (SPR 220-7.0), we pattern the outline of the chip and etch the full depth of the cladding oxide in an ICP etcher, creating a cleanly-defined edge-facet, enabling efficient coupling into the waveguide tapers. To finish the facet and enable fiber-coupling, we etch 100 µm into the silicon substrate using a Bosch etching process [43]. The radius of the optical fiber cladding is 62.5 µm,

so this allows us to dice the chip some distance away from the facet (avoiding roughening/chipping), while still allowing the fiber to freely access the facet.

2.5.2 High-Q Silicon

The etchless silicon waveguide process has been developed by several groups since 2010 [17, 44]. The fundamental limitation for low loss in traditional silicon waveguides is the scattering due to etching-induced sidewall roughness. Rectangular cross-section waveguides are normally defined by anisotropic reactive ion etching. The etching process is inherently rough and can leave behind polymer residue adding to sidewall roughness. In order to eliminate this roughness, the silicon waveguide can be defined via masked thermal oxidation. The thermal oxidation process is atomically smooth, and the rate of thermal oxidation can be controlled by introducing a diffusion barrier to slow down oxygen diffusion. The first demonstration created a very thin low-confinement waveguide by using silicon dioxide as a mask, but later demonstrations made use of silicon nitride, which is a more effective diffusion barrier [17, 18]. This enabled larger cross-section, high-confinement etchless silicon waveguides with quality factors $>10^6$ [18]. In this process, 200 nm of silicon nitride is deposited on an SOI wafer, and then the silicon nitride is patterned and etched down to the silicon layer defining the shape of the waveguides. This wafer is then thermally oxidized at 1200°C, defining a silicon waveguide with a curved sidewall. This can be cladded with more silicon dioxide, or can be further processed for an air-clad or suspended geometry, detailed in Chapter 8.

2.5.3 Integrated Thermal Tuning

Silicon nitride has a thermo-optic coefficient of $4{\times}10^{-5}$ RIU/K, which is somewhat less than that of silicon (1×10^{-4}). Due to a lack of free carriers, thermal tuning is the only efficient way to actively tune the index of silicon nitride, without the addition of other materials such as graphene. Thermal tuning is comparatively slow compared with free-carrier-based index tuning, but nonetheless can introduce versatility to the silicon nitride platform, which will be discussed in detail in Chapter 6.

Microheaters are a common component in integrated photonics, consisting of a simple section of resistive metal positioned above a cladded waveguide (Fig. 2.6), which delivers heat to the waveguide when current is passed through it. The cladding must be thick enough to minimize loss from the metal overlap with the evanescent tail of the waveguide, while remaining thin enough to efficiently induce a temperature change at the waveguide. For single mode silicon waveguides this distance is 1 µm, whereas for the high-Q silicon nitride waveguides described above, a larger distance of ~2 µm is necessary.

Ideally we would be able to induce enough index change to tune a microring resonance across one or more FSRs. For a typical microring radius (~100 µm), we may require several hundred mW of electrical power. Nichrome has been a metal commonly used by our group for integrated microheaters along with nickel, tungsten, and chrome. However, these materials exhibit heater failure at a low threshold power. At this point, current flow causes electrons to transfer momentum and transport material, a process called electromigration. This limits these heaters to several tens of milliwatts of electrical power before they break.

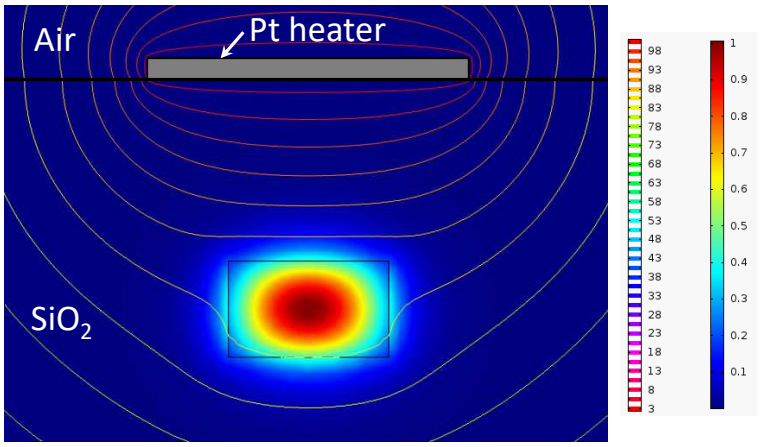

Figure 2.6: Integrated microheater cross-section. Platinum heater is fabricated above the cladded silicon nitride waveguide. Contour lines show temperature profile given a 100°C heater temperature.

In order to achieve higher heater powers, we developed a fabrication process for sputtered platinum microheaters. Platinum is a comparatively robust material, and sputtering as opposed to evaporation can yield denser, more pure thin films, enabling a higher failure power. We choose to do a lift-off process for these heaters. Once the cladding is deposited on top of the waveguide, we spin on 300 nm of lift-off resist (LOR 3A), and then photoresist (SPR 220-3.0). We pattern the heaters using contact photolithography. The LOR undercuts slightly to enable the lift-off process to occur. Evaporation is traditionally used for lift-off because of its directionality, whereas sputtering is slightly more conformal. Therefore, we develop slightly longer to achieve a larger undercut, ensuring that the lift-off etchant will be able to reach underneath the resist and lift-off the film. We sputter 10 nm of titanium as an adhesion layer, and 100 nm of platinum at a low pressure (3 mTorr) to achieve a minimal amount of film stress. We then lift-off in 1165 solvent. These heaters are very robust and can be easily operated upwards of 1 W or more of electrical power, enabling more than one FSR tuning for common microrings. The thermal response time of these heater are 20 µs.

2.6 Integrated Nonlinear Optics

Integrated photonics is an ideal platform for nonlinear optics, allowing the ability to perform nonlinear processes using low-power continuous wave (CW) lasers. As we will discuss in Chapter 3.3, third-order nonlinear optical phenomena are dependent on the intensity of light inside a nonlinear optical medium as well as the degree of nonlinearity of the medium itself. In free space, a diffraction-limited Gaussian beam can be focused inside a nonlinear medium. The most common way of increasing the light intensity to observe significant nonlinear effects is to use a pulsed laser, which can have a very high peak power lasting for picoseconds or even femtoseconds. The repetition rate of such a laser is only in the MHz range, such that the laser has a reasonable average power level while having peak powers in hundreds or even thousands of Watts. These lasers can be complex, sensitive, and expensive, potentially limiting the scope of applications for nonlinear optics technologies. At the chip-scale, high index waveguides can tightly confine light into a small cross-sectional area, increasing the optical intensity beyond that of a free-space beam. Additionally, a high-Q, high-finesse cavity introduces a cavity enhancement of the circulating power level inside the cavity. Integrated silicon and silicon nitride microresonator cavities commonly have a finesse upwards of 10^3-10^4. Therefore, CW lasers can be used at milliwatt power levels, and large, expensive pulsed lasers are no longer required to observe significant nonlinear effects. This is revolutionary, and can pave the way for broader applications of nonlinear optics.

CHAPTER 3

NONLINEAR OPTICS

3.1 Introduction

When light interacts with matter in a purely linear manner, the material refractive index and absorption characteristics determine the phase and amplitude changes experienced by the light. This linear interaction is commonly modeled using the Drude model of an oscillating electron in a parabolic potential [45]. This model is a fairly accurate representation of an electron in a dielectric or semiconductor medium well below its bandgap, for moderate intensities of light. However, the parabolic approximation of the electron potential in a real material is not perfect, and breaks down particularly at higher light intensities. The parabolic potential can deviate in both even- or odd-parity higher-order terms, as a result of the environment surrounding the electron in a crystal lattice or amorphous material. All materials exhibit even-parity higher-order nonlinearities. However, only a specific set of materials exhibit odd-parity nonlinearities, called non-centrosymmetric materials. These materials contain atoms of multiple elements with different atomic weight making up a crystalline lattice, such that the spatial symmetry of the electron potential is broken. This is true for materials such as Group III-V semiconductors (GaAs, InP, etc...), but absent from other crystalline materials such as silicon, due to the presence of only one element in the lattice. The presence of nonlinearities in the electron potential lead to nonlinear behavior of light propagating through such a material, including frequency mixing, generation of new wavelengths of light, as well as electro-optic interactions.

3.2 Nonlinear Susceptibility

The dielectric polarization of a material is defined via a proportionality called the electrical susceptibility, χ, which is a measure of the material response to an electric field. The polarization is given by:

$$P = \varepsilon_0 \chi E, \tag{3.1}$$

in which ε_0 is the permittivity of free space. The electrical susceptibility is related to the relative permittivity, ε_r, and refractive index, n, by:

$$\chi = \varepsilon_\mathrm{r} - 1 = n^2 - 1. \tag{3.2}$$

We examine the nonlinear optical properties of a material by performing a Taylor expansion of P at optical frequency, ω:

$$\begin{aligned} P(\omega) = \varepsilon_0 \chi^{(1)}(\omega_i) E_i + \varepsilon_0 \chi^{(2)}(\omega_i \pm \omega_j, \omega_i, \omega_j) E_i E_j + \\ \varepsilon_0 \chi^{(3)}(\omega_i \pm \omega_j \pm \omega_k, \omega_i, \omega_k) E_i E_j E_k + ...), \end{aligned} \tag{3.3}$$

in which $\chi^{(1)}$ is the linear susceptibility, $\chi^{(2)}$ is the second-order nonlinear susceptibility and $\chi^{(3)}$ is the third-order nonlinear susceptibility. The nonlinear susceptibilities are intrinsic material properties and vary slightly with wavelength (they generally increase near band edges). A non-zero second-order nonlinearity is present in only non-centrosymmetric materials, whereas all materials exhibit a third-order nonlinearity. One can see that for non-zero $\chi^{(2)}$ materials (e.g. GaAs), the susceptibility, and thus the refractive index, is linearly proportional to an applied electric field. This is called the linear electro-optic effect, or Pockels effect. For materials with $\chi^{(2)} = 0$, the refractive index is quadratically proportional to an applied electric field, known as the Kerr effect. These phenomena involve interaction of light with a DC or low-frequency electric field.

However, these nonlinearities also give rise to many interesting multi-photon interactions between multiple light waves.

3.3 Nonlinear Refraction

Unless special effort is taken, frequency conversion processes are generally inefficient in most systems. The most common nonlinearity comes from nonlinear refraction, which is an intensity-dependent refractive index. This originates from the third-order nonlinear coefficient in this form:

$$n(I) = n + n_2 I, \tag{3.4}$$

in which I is the optical intensity, which is proportional to $|E|^2$, and n_2 is the nonlinear refractive index coefficient, which is related to $\chi^{(3)}$ by:

$$n_2 = \frac{3}{8n_0}\chi^{(3)}, \tag{3.5}$$

This nonlinear refraction leads to two main phenomena: self-phase modulation (SPM) and cross-phase modulation (XPM). SPM is a nonlinear phase-shift that an optical field experiences when it propagates in a material due to its own intensity. The nonlinear phase shift is given by:

$$\phi_{\mathrm{NL}} = \gamma PL, \tag{3.6}$$

in which P is the optical power, L is propagation length, and γ is the nonlinear parameter:

$$\gamma = \frac{n_2 \omega}{cA_{\mathrm{eff}}}, \tag{3.7}$$

in which A_{eff} is the effective area of the nonlinear interaction. If another optical field is present, there is an additional phase-shift induced by the its presence, which is called XPM. In this case, the total phase-shift induced due to SPM and XPM is:

$$\phi_{\text{NL}} = \gamma L(P_1 + 2P_2). \tag{3.8}$$

It is important to note that the nonlinear phase-shift contribution from another field (XPM) is twice that from the field itself (SPM).

3.4 Three Wave Mixing

For materials with non-zero $\chi^{(2)}$, under the right conditions, two co-propagating optical fields can interact with each other and form a third optical field at a different frequency. This type of process is broadly referred to as three-wave mixing, and is constrained by both energy conservation and momentum conservation. Given two fields at frequencies ω_1 and ω_2, the generated field at ω_3 could be generated at $\omega_1 + \omega_2$ through sum-frequency generation (SFG) or at $\omega_1 - \omega_2$ through difference frequency generation (DFG). Additionally, if $\omega_1 = \omega_2$, a field at $2\omega_1$ can be generated through a second harmonic generation (SHG) process. Momentum conservation requires that $k_3 = k_1 + k_2$. This constraint determines which generation process is efficient and dominates. Here, the optical nonlinearity allows photon energy to be transferred to frequencies a large frequency difference away. However, due to material dispersion, special care must be taken for momentum conservation to occur, allowing efficient three-wave mixing.

3.5 Four Wave Mixing

For materials in which $\chi^{(2)} = 0$, three-wave mixing cannot properly satisfy energy conservation. Instead, $\chi^{(3)}$ processes require three optical fields to be present in order to generate a fourth field, in a process called four-wave mixing (FWM). There are several common forms of FWM, but here we will focus on FWM involving two pump photons, a signal photon, and a fourth generated photon commonly known as the idler photon. These optical fields satisfy energy conservation such that $\omega_{p1} + \omega_{p2} = \omega_s + \omega_i$, and momentum conservation such that $k_{p1} + k_{p2} = k_s + k_i$. In particular, we will focus on the case of degenerate FWM, in which the two pump photons are identical and come from the same optical field ($w_{p1} = w_{p2} = w_p$ and $k_{p1} = k_{p2} = k_p$). In this case, the signal and idler frequencies are symmetric with respect to the pump. In addition to generation of an idler photon, the signal and idler photons experience nonlinear, or parametric, gain as a result of energy transferred from the two pump photons. Another common FWM process is third-harmonic generation, in which three photons mix to produce a photon at triple their frequency: $\omega_4 = \omega_1 + \omega_2 + \omega_3$.

3.6 Parametric Gain

Parametric gain involves transfer of energy from an optical field at a different frequency strictly obeying conservation of energy without the involvement of material gain via stimulated emission. The efficiency of the FWM process depends on several factors. Considering the nonlinear parameter, γ (Eq. 3.7), for highest nonlinear effects we see that a high n_2 and a small A_{eff} are desirable. The combination of the pump power level with this nonlinear parameter as well as

the phase-matching condition give rise to parametric gain, g, defined as:

$$g = \sqrt{4\gamma^2 P_1 P_2 - (\kappa/2)^2}, \tag{3.9}$$

in which P_1, P_2 are pump powers, and κ is the total phase mismatch considering dispersion and nonlinear phase-shift. If the phase-mismatch is too large, the argument of Eq. 3.9 will be negative, making the gain an imaginary value (equivalent to loss).

3.7 Phase Matching

Phase-matching is necessary for ensuring efficient nonlinear processes involving light at multiple wavelengths. Most materials are dispersive, such that their refractive index varies across the wavelength spectrum. Light at different wavelengths will therefore travel with different phase and group velocities. Nonlinear wave mixing of multiple wavelengths of light thus involves photons potentially traveling at different velocities. However, for efficient nonlinear wavelength conversion, Eq. 3.9 imposes a constraint on these interactions, such that total phase mismatch, κ, is small; otherwise, the argument of Eq. 3.9 becomes negative, and the parametric gain becomes imaginary. Therefore, the total phase of all interacting photons must sufficiently satisfy momentum conservation, and any leftover phase mismatch tends to decrease the total gain and/or bandwidth of the nonlinear process. Phase-matching is thus a crucial part of design of nonlinear photonic devices.

Here we outline the phase-matching condition for degenerate four-wave mixing. Conservation of momentum states that the sum of the propagation

constants for all input photons must equal that of the output photons:

$$\beta_{p1} + \beta_{p2} = \beta_s + \beta_i, \tag{3.10}$$

in which $\beta_{p1,p2} = \beta_p$ are the degenerate pump photons, β_s is the signal photon and β_i is the idler photon. We perform a Taylor expansion on the signal and idler surrounding the pump frequency, yielding:

$$\begin{aligned} \beta_s(\omega + \delta) &= \frac{n\omega_p}{c} + \beta_1(\omega_p)\delta + \frac{1}{2}\beta_2(\omega_p)\delta^2 \\ \beta_i(\omega - \delta) &= \frac{n\omega_p}{c} - \beta_1(\omega_p)\delta + \frac{1}{2}\beta_2(\omega_p)\delta^2 \end{aligned} \tag{3.11}$$

in which δ is the angular frequency offset from the pump frequency, ω_p, $\beta_1 = \frac{d\beta}{d\omega} = 1/v_g$ is the first-order dispersion, and $\beta_2 = \frac{d^2\beta}{d\omega^2}$ is the second-order dispersion, also known as the group-velocity dispersion (GVD). The resulting phase mismatch, $\Delta\beta$, is:

$$\Delta\beta = \beta_2(\omega_p)\delta^2 + \phi_{NL} \tag{3.12}$$

We see that the first order dispersion terms cancel, along with all odd-order terms (β_3, β_5, etc). This leaves us with a phase mismatch primarily determined by the GVD, along with the even higher-order terms (β_4, β_6, etc) as well as the nonlinear phase-shift. Therefore, GVD is the primary design parameter for achieving FWM gain and frequency comb generation. To achieve a zero phase-mismatch, the phase shift induced by the GVD must serve to compensate the nonlinear phase-shift, and therefore requires a negative value. This is referred to as anomalous group-velocity dispersion, in which shorter wavelengths of light travel faster than longer wavelengths of light. Normal dispersion (GVD > 0) is the reverse. Generally, normal dispersion results in a lack of phase matching, yielding very narrowband nonlinear gain only closely adjacent to the pump

frequency. However, several studies have introduced applications of normal dispersion frequency comb generation [46, 47].

3.8 Dispersion Engineering

Light traveling through a waveguide is affected by material dispersion of the core and cladding media, but is also affected by dispersion induced by the waveguide geometry. This is because light at different wavelengths experiences a different effective waveguide mode index. This waveguide dispersion is the result of an interplay between waveguide width and height, refractive index contrast, polarization, as well as sidewall angle and bending radius. The total dispersion of a waveguide is a combination of both material and waveguide dispersion characteristics. Intuitively, a waveguide mode whose cross-section is much larger than the wavelength will be highly confined and experience primarily core material dispersion characteristics [Fig. 3.1(a)], whereas a waveguide mode for a very small waveguide will be delocalized and experience mostly cladding material dispersion [Fig. 3.1(b)]. Between these extremes, waveguide dispersion can dominate the overall dispersion characteristics [Fig. 3.1(c)]. Thus, the design of the waveguide cross-section can be used as a powerful tool to engineer the dispersion. High index contrast provides strong light confinement and enables a high degree of control for dispersion engineering. Dispersion control of high index contrast waveguides has led to significant developments in integrated nonlinear optics, including Kerr frequency comb generation.

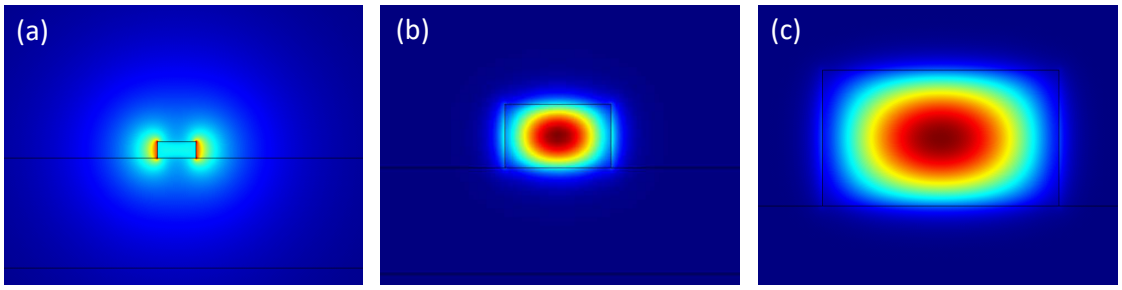

Figure 3.1: Wavguide dispersion engineering is primarily controlled by cross-sectional geometry, which affects mode confinement. This is particularly effective for high index contrast waveguides, which have dramatically different mode profiles for (a) small, (b) medium, and (c) larger cross-sections.

3.9 Kerr Frequency Comb Generation

A frequency comb is a set of discrete, equally-spaced optical frequency lines, forming the teeth of a comb-like shape in the frequency domain (Fig. 3.2). This frequency comb corresponds to a pulse train in the time domain, based on the Fourier transform relation between the two. All spectral lines are precisely spaced apart by the repetition rate of the pulses, f_{rep}. By repeatedly subtracting f_{rep} from a comb line frequency, one arrives at the frequency offset between the lowest order comb line and zero-frequency (DC), which we call the carrier-envelope offset, or f_{CEO}. This frequency translates to the phase-offset of the envelope of the pulse train. The absolute frequency of any single comb line can thus be described simply by these two values:

$$f_{\text{comb}} = m f_{\text{rep}} + f_{\text{CEO}}, \tag{3.13}$$

where m is an integer. If f_{rep} and f_{CEO} are experimentally measured and stabi-

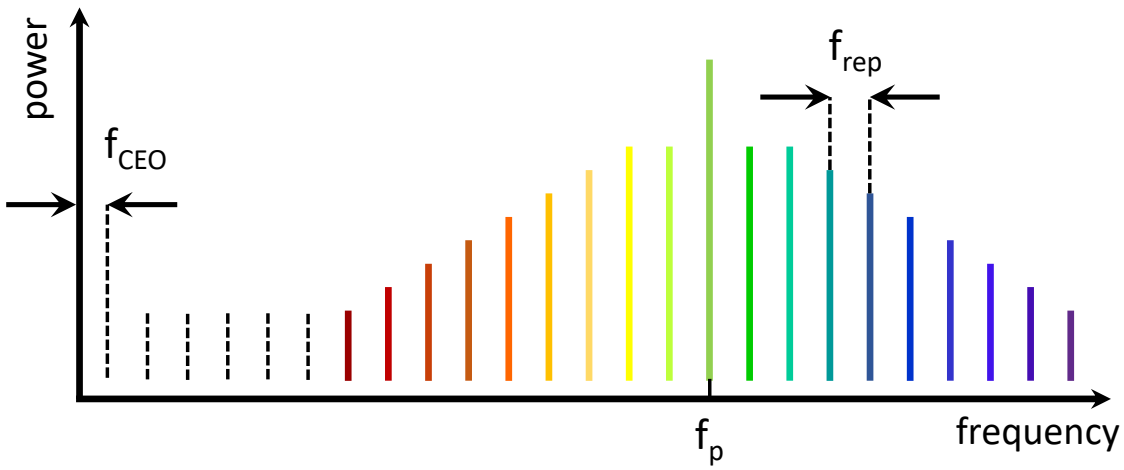

Figure 3.2: General spectrum of a frequency comb, with a discrete comblines separated by precise spacing f_{rep} and carrier envelope offset f_{CEO}

lized, the absolute frequency of each comb line can be known to a very high precision. Frequency combs can thus be seen as a frequency "ruler," and have important applications in frequency metrology, optical clocks, and astronomical calibrations [48–50]. Additional applications of frequency combs include optical spectroscopy, arbitrary waveform generation, and telecommunications [51–53]. The 2005 Nobel Prize in Physics was awarded to Hall and Hansch in part for the development of frequency combs and their spectroscopy applications [54].

Traditionally, Ti-sapphire or other mode-locked lasers are the most commonly-used frequency combs. However, during the last decade, a new type of frequency comb generation has been developed: microresonator-based Kerr frequency comb generation. This leverages the third-order (Kerr) nonlinearity of dielectric or semiconductor materials inside an optical microcavity through a process called optical parametric oscillation. An optical parametric oscillator (OPO) consists of a nonlinear medium inducing parametric gain inside of a cavity. The dynamics of OPO Kerr comb generation can be described mathe-

matically by a form of the nonlinear Schroedinger Equation called the Lugiato-Lefever Equation. Several rigorous studies are available in the literature [55–57]; here, I present an intuitive explanation of the process to act as a companion to such detailed investigations for gaining a deeper understanding. When a continuous wave pump beam enters the OPO cavity, the level of the FWM gain increases with cavity circulating power. At low powers, round-trip loss exceeds FWM gain, so only spontaneous FWM sidebands are transiently generated at the single-photon levels. This is similar to a laser cavity below threshold, in which round-trip loss exceeds material gain, such that only spontaneous emission exists in the cavity. To increase circulating power, the pump laser frequency is tuned into a resonance toward the cavity resonance frequency, which increases the circulating power. The laser is detuned from the blue (shorter wavelength) side of the resonance in order to maintain thermal stability, commonly referred to as the soft-thermal lock [58]. At the point where the round-trip gain exceeds the round-trip loss, the OPO threshold is reached, and a self-sustained oscillation is produced, generating FWM sidebands on either side of the pump frequency (Fig. 3.2). These sidebands are generated at an integer number of FSRs away from the pump, depending on the dispersion characteristics. As the pump circulating power increases, additional oscillation sidebands are generated through mutual interactions between lines, to the point where each cavity FSR contains a frequency comb line. At this point, the comb lines generally have random or uncorrelated phases with respect to each other, and in some cases one cavity FSR may contain more than one comb line separated by a very small frequency offset. When incident on a photodetector, these comb lines generate low frequency beat-notes and high phase-noise when monitored by a radio frequency (RF) spectrum analyzer. This lack of phase coherence be-

tween all the lines creates a high CW background level in the time domain and prevents pulses from forming. As the pump detunes farther into the resonance, the comb enters a chaotic-like state, in which nonlinear interactions between all the comb lines create a high phase noise level and large amplitude fluctuations throughout the comb. After further detuning, the nonlinear interactions form a phase-locked state, in which all low-frequency RF noise disappears, indicating a degree of phase-coherence between lines throughout the comb. This state is referred to as a multi-soliton state. A soliton is a precisely-defined mathematical solution of a nonlinear wave equation, which corresponds to a pulse which propagates while maintaining its shape due to a balance between nonlinear and dispersive effects. The solution to the Lugiato-Lefever Equation, which is the final state of the Kerr frequency comb, is a single soliton pulse that is circulating in the OPO cavity. Prior to this state, several multi-soliton states exist, in which multiple soliton pulses circulate in the cavity. These states transition by successively shedding solitons, until only a single soliton is left. It has been shown that these states actually exist on the red-detuned side of the resonance, which maintains thermal stability due to a nonlinear distortion of the resonance shape [58]. They exhibit the hyperbolic secant squared envelope in the frequency domain that is characteristic of a single soliton. The span of the comb is determined by the characteristics of the even-order dispersion parameters (β_2, β_4, etc). Depending on the dispersion properties, a dispersive wave can be generated, which is a peak in the comb envelope toward the edge of the comb [56]. At this point, the CW pump laser generates a pulsed output whose repetition rate matches the FSR of the cavity, and whose linewidth corresponds to the comb bandwidth.

These frequency combs have been developed in a wide variety of integrated photonic platforms, including silica microtoroids, silica wedge resonators, crys-

talline fluoride whispering-gallery mode resonators, as well as microring resonators made of silicon nitride, silicon, diamond, aluminum nitride, high index glass, and AlGaAs [10,11,20,52,53,59–72]. The radius of these microresonators is anywhere between several tens of microns to several millimeters, creating repetition rates from tens to hundreds of gigahertz. Typically, these cavities exhibit high quality factors between 10^6 and 10^9. The small size and high finesse of these cavities enable frequency comb generation with several milliwatts of CW pump power. These characteristics are in great contrast to traditional frequency combs which require table-top-sized pulsed mode-locked lasers as a pump rather than a CW laser.

Microresonator frequency combs were first developed in the near-IR telecom range (1550 nm), but have since spread to both the visible [73] as well as mid-IR wavelengths [59]. This spread is fueled by unique applications, such as biological imaging in the visible and optical spectroscopy in the mid-IR. Several challenges have slowed the progress of frequency combs at these wavelengths. In the visible range, most dielectric materials exhibit a strong normal dispersion, making it difficult to achieve anomalous dispersion and FWM gain. In the mid-IR, most common materials have strong absorption in the mid-IR, such as silicon dioxide, thus preventing high-Q resonators and comb generation. Additionally, a greater degree of control over the comb generation process through active tuning is desirable for many applications, including those at near-IR wavelengths. The work presented in the following chapters aims to directly address these outstanding problems in order to expand the scope and versatility of microresonator frequency comb generation and the field of integrated nonlinear optics.

CHAPTER 4

FREQUENCY COMB GENERATION AT VISIBLE WAVELENGTHS

4.1 Introduction

Microresonator-based optical frequency combs at visible wavelengths enable various applications including precise optical clocks, frequency metrology, and biomedical imaging [22,48,53]. However, visible comb generation has been limited by strong material dispersion and scattering losses at short wavelengths. Frequency comb lines generated near visible wavelengths would enable locking of combs to atomic transitions, which is critical for metrology. Several atomic transitions commonly used for stabilization of optical clocks, including rubidium and cesium, are located in the near-visible to visible range [74–76]. Additionally, comb lines in the visible range are of particular interest for biological applications. The red to near-infrared (near-IR) wavelength range is a target region for biological imaging, falling between the increased absorption of water at longer wavelengths and the increased Rayleigh scattering in tissue at shorter wavelengths. The availability of multiple comb line sources in this range could enhance the resolution in biological tissue imaging using optical coherence tomography (OCT) [22,77].[1]

One of the main challenges in achieving comb generation at visible wavelengths is the strong normal material dispersion that is characteristic of the dielectric materials used in microresonator devices (silica, silicon nitride, calcium fluoride, etc) as well as the high degree of scattering in this spectral range. For microresonator-based comb generation, low anomalous group-velocity dis-

[1] Portions of this chapter are reproduced with permission from [78]

persion (GVD) is necessary for phase-matching and efficient four-wave mixing (FWM) and parametric oscillation [79]. At near-IR wavelengths, the normal material dispersion is compensated by waveguide dispersion, which is dependent on the waveguide dimensions, to allow for the requisite dispersion profile for efficient comb generation [64, 79]. However, at shorter wavelengths approaching the band gap of the dielectric material, the material dispersion becomes too strong to be compensated by waveguide dispersion, which results in poor phase matching conditions. Additionally, Rayleigh scattering at the waveguide sidewalls increases inversely as λ^4, which inherently lowers the Q factor of resonators at shorter wavelengths. This decreases the cavity enhancement of the pump and further reduces the efficiency of nonlinear processes required for comb generation.

Previous demonstrations of broadband combs pumped in the near-infrared have not been able to extend into the visible range, and only narrowband comb generation has been achieved below 800 nm. Octave-spanning combs pumped at 1.55 μm have generated lines beyond 2 μm wavelength on the long-wavelength side but fail to extend beyond 900 nm at shorter wavelengths [80, 81]. Microring resonators have also been pumped closer to the visible range at 1064 nm, resulting in broad combs with lines extending below 1 μm [63] and as low as 830 nm [82]. There has been one demonstration to date of frequency comb lines below 800 nm, which employed a higher-order whispering gallery mode in a crystalline calcium fluoride resonator, but was able to generate only a 2 nm wide comb at 794 nm [83].

4.2 Second-Order Nonlinearity in Silicon Nitride

We circumvent the traditional challenges in achieving microcombs in the visible range and instead simultaneously employ the second- and third-order nonlinearity of silicon nitride (Si_3N_4) to generate frequency comb lines at visible wavelengths. Silicon-based materials have traditionally been limited to third-order ($\chi^{(3)}$) nonlinear interactions as they are inherently centrosymmetric in either crystalline (c-Si) or amorphous (a-Si or SiN_x) forms. Second-order nonlinear optical processes require breaking the symmetry of the material. The recent demonstrations of both Si_3N_4 and silicon as second-order nonlinear ($\chi^{(2)}$) materials [84–92] has expanded the range of possible applications for this CMOS-compatible platform. The symmetry-breaking in these otherwise-centrosymmetric materials has been attributed to 1) high levels of strain in the waveguide material [84], 2) surface effects from waveguide-cladding interfaces, which removes the bulk symmetry of the amorphous film [86–89], and 3) embedded silicon defects or nanoclusters [90, 91]. The $\chi^{(2)}$ coefficient has been estimated to be as high as 5.9 pm/V in Si_3N_4 [91], and 190 pm/V in silicon [92]. Second-order nonlinear processes such as second-harmonic or sum-frequency generation inherently involve wide, octave-spanning frequency conversion away from the pump frequency, as opposed to third-order processes such as FWM, which typically involve narrow conversion near the pump frequency. Here we use this wide-band attribute of $\chi^{(2)}$ nonlinearity to achieve wide frequency conversion from near-IR into visible wavelengths.

4.3 Device Design

We generate a parametric frequency comb in the near-IR using $\chi^{(3)}$ and frequency- translate it into the visible range (Fig. 4.1(a)) using $\chi^{(2)}$ in an integrated ring resonator cavity. A single-frequency, continuous-wave (CW) pump laser in the near-IR is coupled into a high-Q Si_3N_4 ring resonator [41,42], which acts to enhance the pump power and serves as the nonlinear medium. The pump laser first undergoes $\chi^{(2)}$ second-harmonic generation (SHG), producing one line in the visible range. As the cavity circulating power increases, the pump undergoes $\chi^{(3)}$ FWM optical parametric oscillation, which produces a frequency comb in the near-IR range (Fig. 4.1(b)). The comb lines then mix with the strong near-IR pump through a $\chi^{(2)}$ sum-frequency generation (SFG) process (Fig. 4.1(c)), which produces a set of comb lines in the visible range that are generated simultaneously with the near-IR comb. The generated comb lines therefore simultaneously address two widely different wavelength bands. Additionally, all processes are achieved in a single integrated device using a single CW laser source.

We engineer the waveguide dispersion to simultaneously phase-match near-IR frequency comb generation, second-harmonic generation, and sum-frequency generation. The high finesse of the Si_3N_4 cavity enhances the efficiency of nonlinear processes. The use of high-index contrast waveguides provides the ability to readily control the waveguide dispersion, and using Si_3N_4 eliminates the negative effects of free carriers and two photon absorption at the operating wavelengths [93]. Through dispersion engineering, we simultaneously satisfy the phase-matching conditions for each nonlinear process. For efficient SHG, the effective indices of the fundamental and second harmonic (SH)

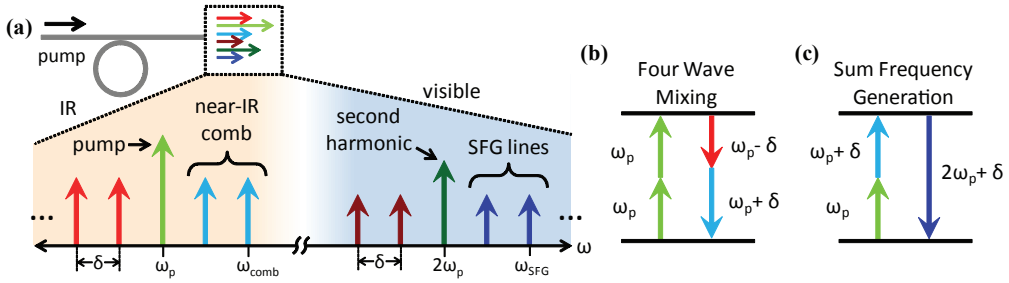

Figure 4.1: (a) A single near-IR pump is coupled into a microring cavity and undergoes second-harmonic generation, near-IR frequency comb generation, and sum-frequency generation to generate simultaneous near-IR and visible wavelength frequency comb lines. (b) Nonlinear photon interaction energy conservation for degenerate four-wave mixing optical parametric oscillation taking place in the near-IR. (c) Nonlinear photon interaction energy conservation for sum-frequency generation between one pump photon and one comb line photon generating a comb line in the visible. This process is identical for corresponding comb lines colored red in (a).

modes must match. This phase-matching is achieved by using a higher-order waveguide mode for the SH light, as in [86]. The third-order TE mode at twice the fundamental frequency is designed to have the same effective mode index as the fundamental TE mode of the pump. We use a finite-element mode solver to calculate effective indices of each mode by taking into consideration material dispersion, a 4° sidewall angle introduced during fabrication, and the waveguide bending radius of 104 µm. As shown in Fig. 4.2(a), this phase-matching condition is satisfied at a fundamental wavelength of 1540 nm for a waveguide with dimensions 700-nm tall by 1400-nm wide. This waveguide dimension is also chosen to optimize optical parametric oscillation. The phase-matching condition for optical parametric oscillation is largely dependent on group-velocity dispersion (GVD). The optimal condition for oscillation is a low level of anomalous GVD at the pump frequency [64]. This dispersion is then compensated by the $\chi^{(3)}$ nonlinear phase shift in order to achieve the proper phase-matching

for degenerate FWM. As shown in Fig. 4.2(b), the waveguide dimensions that satisfy SHG phase-matching also exhibit a sufficiently low level of anomalous GVD for efficient parametric oscillation.

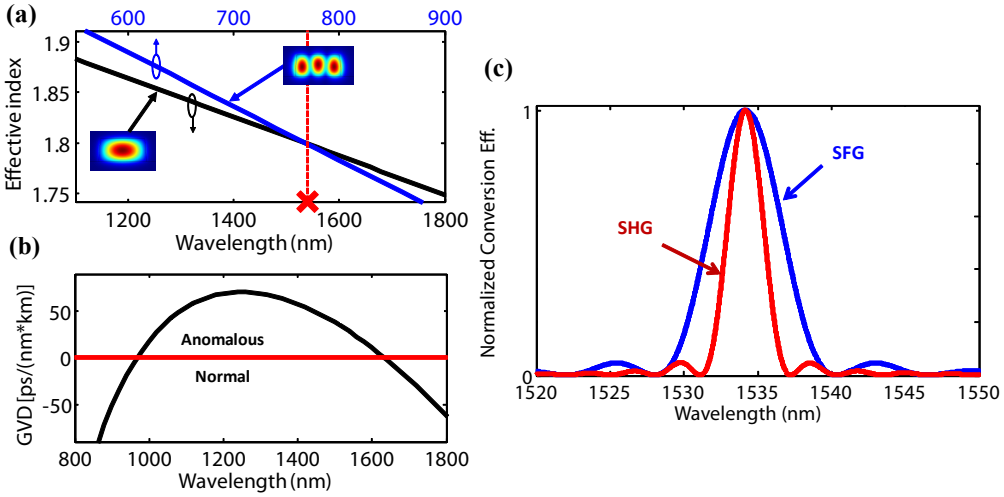

Figure 4.2: (a) The effective mode index dispersion of the fundamental TE mode in near IR spectral range and the third-order TE mode in the visible spectral range. One can see that around the pump wavelength of 1540 nm (red X), phase-matching occurs. (b) The group velocity dispersion (GVD) of the fundamental TE mode shown in (a). The low level of anomalous GVD at the pump wavelength of 1540 nm allows for efficient frequency comb generation. (c) Conversion efficiency vs. wavelength for $\chi^{(2)}$ SHG and SFG processes, estimated using Eq. (1). Phase-matching bandwidth for SFG is wider than for SHG, allowing for multiple comb lines to be converted into the visible range.

Once phase-matching is ensured for both FWM and SHG processes, the final SFG process is automatically phase-matched, resulting in simultaneous phase-matching for all desired processes. The phase-matching of the SFG process involves one photon from a comb line mixing with one photon from the strong pump. The phase-mismatch Δk is given by: $\Delta k = n_1\omega_1/c + n_2\omega_2/c - n_3\omega_3/c$, where n_i are the effective mode indices of the pump, comb line, and sum-frequency line, respectively. The corresponding photon angular frequencies,

ω_i, satisfy energy conservation ($\omega_1 + \omega_2 = \omega_3$). For a waveguide of equivalent length, in the limit of low single-pass conversion, the converted power for SFG in a cavity is given by:

$$P_3 = \frac{2\, d_{\text{eff}}^2\, \omega_3^2\, C_1 P_1 C_2\, P_2\, A_3}{n_1 n_2\, n_3\, \epsilon_0\, c^3 A_1 A_2\, C_3}\, f_{1,2,3}\, L_{\text{eff}}^2\, \text{sinc}^2\left(\frac{\Delta k\, L_{\text{eff}}}{2}\right), \tag{4.1}$$

where $d_{\text{eff}} = \chi^{(2)}/2$, $C_i P_i$ is the cavity circulating power, where C_i is the cavity enhancement factor, A_i is the effective mode area, and L_{eff} is the effective cavity length [94]. The effective cavity length L_{eff} is equal to the product of the group velocity and the cavity lifetime of the mode τ_i where $\tau_i = Q_i/\omega_i$. The overlap between the spatial modes of the interacting spectral lines is taken into account by the function $f_{1,2,3}$ [86]. Figure 4.2(c) shows normalized conversion efficiency versus wavelength for SFG and SHG, in which the latter follows the same conversion efficiency as SFG but with two photons allocated for the pump. The phase-matching requirement for SFG is less stringent than that of SHG, which provides the opportunity to convert a wider bandwidth of near-IR comb lines into the visible range. Intuitively, this property arises from keeping the pump stationary as the comb line varies in the SFG process, which reduces the phase-mismatch compared to SHG, in which both source photons contribute to the phase- mismatch. This bandwidth is determined primarily by the slope of the phase-mismatch Δk with respect to wavelength, which in turn is determined by the group index mismatch of the fundamental and higher-order modes. The choice of a different higher-order mode with a group index closer to that of the fundamental mode could further increase the conversion bandwidth. Overall, these three nonlinear processes are simultaneously phase-matched and are able to occur together in the same cavity structure.

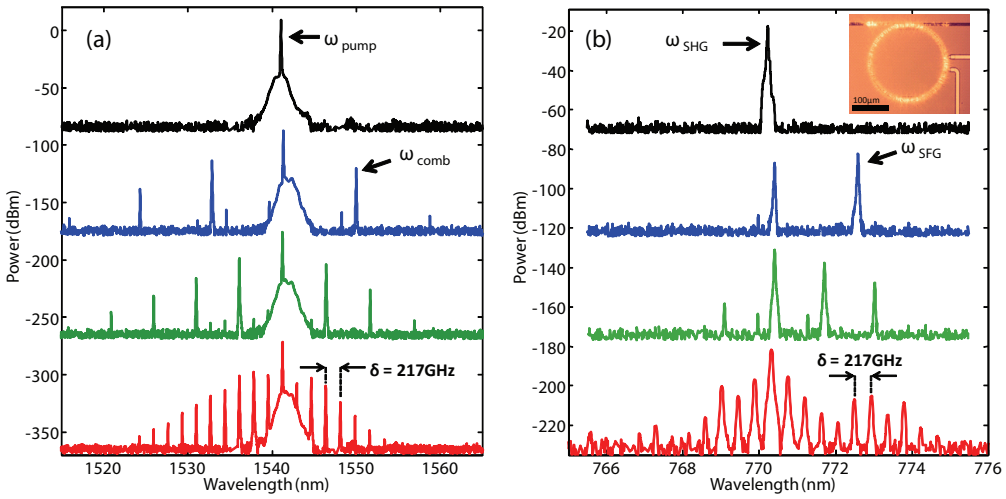

Figure 4.3: (a) Near-IR CW pump laser and frequency comb generation. Several different states of the frequency comb are shown. (b) Visible second-harmonic generation and frequency comb lines for corresponding spectra in (a). The vertical scales have been offset for clarity. Comb spacing is preserved by the SFG process for all states of the frequency comb shown. Inset micrograph shows the visible light generated by the device. These wavelengths fall just outside the normal range of the CCD camera, so the red color that is seen by the naked eye is distorted. A microheater was fabricated on this device for thermal tuning but was not used in this experiment.

4.4 Experimental Results

We measure up to 17 comb lines frequency-translated from near-IR into visible wavelengths extending from 765-775 nm. We use a Si_3N_4 ring resonator with radius 104 μm, waveguide dimensions 700 nm × 1400 nm and a coupling gap of 560 nm. The fabrication methods are the same as those outlined in previous work [41]. The resonator has a $Q = 1.5{\times}10^6$. All nonlinear processes occur inside the resonator cavity, and are enhanced by this high Q. The pump is produced by a single-frequency tunable diode laser amplified with an erbium-doped fiber amplifier (EDFA). The amplified spontaneous emission (ASE) noise from the

EDFA is filtered using a 1-nm tunable bandpass filter, and a polarization controller is used to couple to the fundamental quasi-TE mode of the waveguide using a single-mode lensed fiber. The pump is tuned into a cavity resonance near 1540 nm (Fig. 4.3(a), black curve), with approximately 700mW in the bus waveguide. At low circulating power in the cavity, the second-harmonic is generated at the expected wavelength of 770.3 nm, as shown in the black curve of Fig. 4.3(b). The maximum second harmonic conversion efficiency we measure is -29 dB, in which ~1 mW of the second harmonic has been generated. As the pump is tuned into the resonance, the circulating power in the cavity builds up, which leads to the onset of near-IR frequency comb generation as well as frequency conversion of the comb lines into the visible range. A micrograph inset shows the generated visible light. Several states [62, 95] of the generated comb are shown, with comb lines generated every 5, 3, and 1 free-spectral ranges (FSR's). In the filled-in comb state (red), we observe a visible comb bandwidth of nearly 10 nm, covering 17 FSR's. There is equal frequency spacing of 217 GHz among the near-IR comb lines and the visible comb lines. The SFG conversion efficiency is approximately -20 dB. We believe this conversion efficiency is higher than the SHG conversion of the pump due to a lack of precise pump phase-matching for this resonator. This is evident in the blue curve in Fig. 4.3(b) where we see that the converted comb line five FSR's away has a higher power than the second-harmonic of the pump. We also observe significant variations across different comb lines, which we attribute to higher-order group index mismatch, resulting in a detuning of the generated light from the cavity resonances.

We perform a seeded SFG experiment in order to characterize and confirm this conversion process. Nonlinear frequency conversion processes can be characterized by the conversion efficiency with varying pump powers. For SFG, the

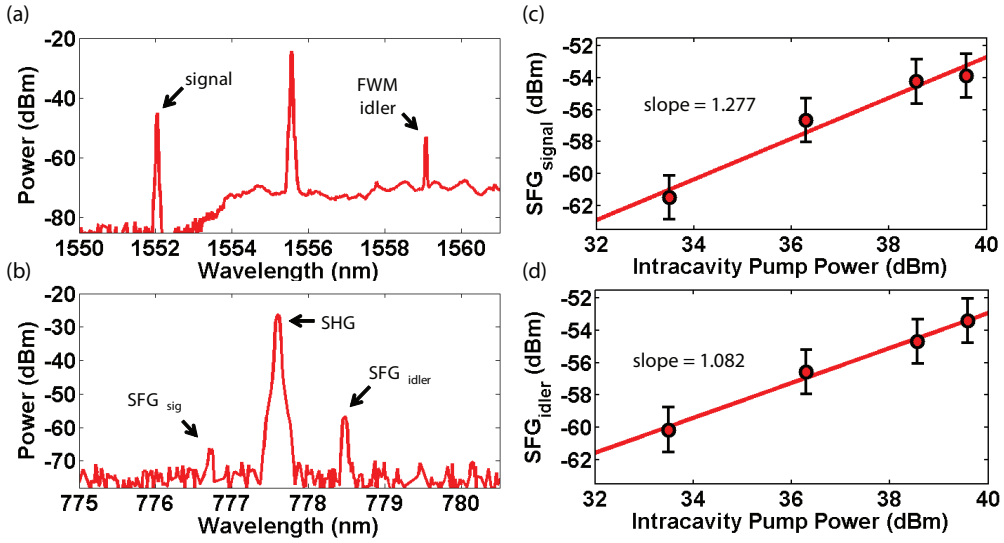

Figure 4.4: Seeded SFG experiment. (a) Near-IR pump and signal lasers are coupled into the ring resonator. An additional line is seen symmetric about the pump, resulting from FWM. (b) The visible spectrum shows SHG of the pump wavelength and SFG of pump wavelength mixing with both the signal and FWM idler lines. (c) Conversion efficiency vs. pump power for SFG_{signal}, showing conversion proportional to the pump power. (d) Conversion efficiency vs. pump power for SFG_{idler}, showing conversion proportional to pump power.

nonlinear process involves one pump photon, so the converted power is proportional to the pump power. For a $\chi^{(3)}$ process such as degenerate FWM, the nonlinear process involves two pump photons, so the converted power is proportional to the square of the pump power. Therefore, in a plot of conversion versus pump power, the slope reflects the nature of the nonlinear process. In this experiment, we use a fiber wavelength-division multiplexing (WDM) coupler in order to combine the near-IR pump laser with another near-IR tunable diode laser to send into the resonator cavity. This second tunable laser allows us to have experimental control of the signal being converted into the visible range rather than for the case above, in which the generated comb lines are being converted. For this experiment, we use a ring resonator cavity with the same

cross-sectional dimensions as above but with lower Q, yielding a higher parametric oscillation threshold. This ensures that there are no near-IR comb lines that can be converted into the visible range. We begin by tuning the pump laser far enough into resonance to generate a second harmonic line while remaining below the oscillation threshold. This ensures that we are operating at the proper phase-matching position for the SFG process, consistent with the above results. Next, the signal laser is tuned into a neighboring resonance. We observe seeded FWM surrounding the pump (Fig. 4.4(a)), which is not desired but is unavoidable in this situation as this process is well phase-matched. Additionally, we observe the desired conversion into the visible range for both lines surrounding the pump (Fig. 4.4(b)). We measure the conversion efficiency versus pump power, as shown in Figs. 4.4(c) and 4.4(d). Our conversion here is low because we are using lower power values to ensure we remain below the parametric oscillation threshold. Some small error in the slope for the signal conversion is due to instabilities in the measurement setup. As shown, we observe a slope of approximately 1, confirming that this is indeed a $\chi^{(2)}$ SFG process.

4.5 Discussion

We analyze the phase-matching conditions for several nonlinear interactions and confirm that the nonlinear process translating the comb into visible wavelengths is the SFG process. The presence of lines at all FSR resonances rules out SHG as the overall dominant process. If the entire near-IR comb were to undergo SHG, the frequency spacing of the visible comb would be doubled, resulting in a comb line at every-other FSR resonance. We also consider other $\chi^{(3)}$ processes as an alternative comb generation mechanism. FWM optical paramet-

ric oscillation of the second-harmonic frequency would generate a visible comb with lines at every FSR. However, according to [10], the parametric oscillation threshold is given by,

$$P_{th} \approx 1.54 \left(\frac{\pi}{2}\right) \frac{Q_C}{2\,Q_L} \frac{n_{\text{eff}}^2 V}{n_2\,\lambda_0\,Q_L^2}, \tag{4.2}$$

where n_{eff} is the linear mode index, V is the resonator mode volume, $n_2 = 2{\times}10^{-19}$ m^2/W is the nonlinear refractive index, λ_0 is the pump wavelength, Q_C and Q_L are coupling and loaded quality factors of the resonator mode, respectively, and,

$$\frac{1}{Q_L} = \frac{1}{Q_i} + \frac{1}{Q_C}, \tag{4.3}$$

where Q_i is the intrinsic quality factor [10]. At visible frequencies, P_{th} increases due to increase of scattering losses from Rayleigh scattering (decreasing Q_i) and due to the frequency dependence of the waveguide-ring coupling condition (decreasing Q_C). We estimate that Q_i at visible wavelengths is less than 10^5 and the ratio Q_C/Q_L is at least 10, yielding an under-coupled resonance condition. Thus, assuming a mode volume of 400 μm^3, $P_{th} \geq 10$ W, which is at least four orders of magnitude above the ~1 mW of power in our second-harmonic line. Finally, we also rule out non-degenerate FWM for generating the visible comb lines. Non-degenerate FWM would involve the near-IR pump mixing with the second-harmonic and the near-IR comb lines to generate the visible comb lines. The phase-matching requirements for this process stipulate that the group velocities (v_g) of the near-IR light and the visible light must match. As shown in Fig. 4.2(a), the slope of the effective index curve for each mode is different, and this slope determines the v_g of the circulating light. While the nonlinear phase shift due to cross-phase modulation can be used to compensate for this v_g mismatch, this phase shift would require ~2 W of pump power to minimize the phase mismatch for lines even only one FSR away. Here, we only supply 700 mW in the bus waveguide and generate ten FSR's away from the pump, so

this non-degenerate FWM process is not suitably phase-matched. As outlined above, $\chi^{(2)}$ SFG is phase-matched and takes advantage of direct interaction with the strong pump, and thus it is left as the most plausible process for generating these comb lines.

We envision this result as a potential platform for an on-chip optical atomic clock and the creation of a coherent link between visible and near-IR wavelengths. We predict that phase correlations will be preserved in the SFG process in the presence of comb mode-locking, so the visible comb lines would be correlated with the near-IR comb as well. Additionally, the ability to produce SHG on-chip could also be applied to *f*-2*f* self-referencing by frequency-doubling the long wavelength edge of an octave-spanning comb. Off-chip $\chi^{(2)}$ crystals used for *f*-2*f* self-referencing of octave spanning combs are not always available for the desired wavelength ranges and are not integrated, but by tailoring phase-matching conditions, this self-referencing could potentially be integrated on-chip. Additionally, by integrating the on-chip microresonator devices with atomic vapor systems [96, 97], this process can enable a compact platform for microresonator-based frequency comb stabilization, leading to applications in biomedical imaging, frequency metrology, and on-chip optical clocks.

CHAPTER 5

ELECTRO-OPTIC EFFECT IN SILICON NITRIDE

5.1 Introduction

Studies have demonstrated silicon nitride to have $\chi^{(2)}$ properties, demonstrated via second harmonic generation (SHG) [85, 87, 89, 91]. The linear electro-optic (EO), or Pockels, effect, is also related to the $\chi^{(2)}$ nonlinearity, and is of significant interest for lossless high speed phase modulation beyond 100 GHz, currently only available in platforms such as aluminum nitride and lithium niobate [13, 98].[1]

The origin of $\chi^{(2)}$ properties in silicon nitride have remained somewhat unclear to date. Several studies have investigated interface effects [87, 89] and embedded silicon nanocrystals [91] as the possible origins of the $\chi^{(2)}$ of silicon nitride. Studies have also spanned different deposition methods, including sputtering [91], PECVD [89], and LPCVD, in which the highest $\chi^{(2)}$ coefficient of 5.9 pm/V was reported for sputtered silicon nitride. Second harmonic waves generated at interfaces have been used to monitor surface properties [100]. The interface locally breaks the bulk symmetry of the material, allowing $\chi^{(2)}$ effects to occur.

[1] Portions of this chapter are reproduced with permission from [99]

5.2 Device Design

We present the first demonstration of the Pockels effect in silicon nitride by enhancing the $\chi^{(2)}$ effect due to interfaces in the waveguide using a horizontal multi-slot cross-section [Fig. 5.1(a)]. For the transverse-electric (TE) polarization, the electric field is continuous and parallel across the interfaces [Fig. 5.1(b)], and for transverse-magnetic (TM) polarization, the electric field is perpendicular to the interfaces and forms a series of slot modes [Fig. 5.1(c)]. The slot effect creates a large discontinuity at each interface, and concentrates light in the low index slot. A similar structure was investigated in [6], in which SHG was observed. In order to probe the $\chi^{(2)}$ nonlinearity, we measure the Pockels effect, which is a linear change in refractive index due to an applied electric field.

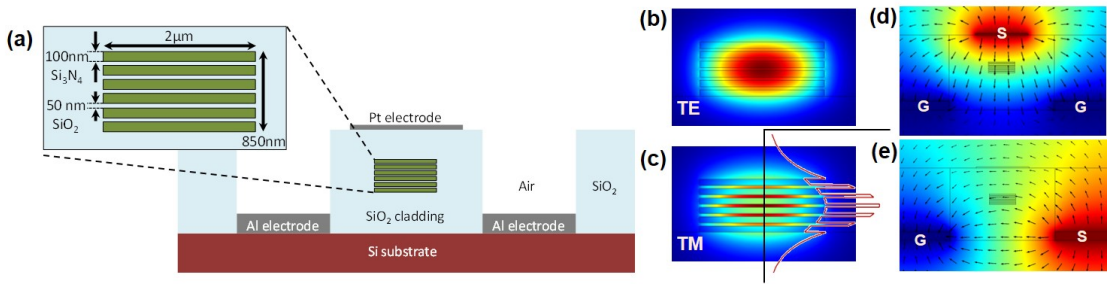

Figure 5.1: (a) Cross section of device, showing horizontal multi-slot waveguide stack and electrode configuration, with fundamental TE (b) and TM (c) modes. Field profile for TM mode shows field enhancement at interfaces due to the slot effect. Electrodes surrounding the waveguide to generate (b) vertical and (c) horizontal electric fields across the waveguide. Voltage configuration (GSG and GS) is shown in the color map.

By fabricating an alternating multi-slot waveguide cross-section, we increase the mode interaction with the interfaces in order to enhance the EO coefficient.

We fabricate a high Q microring resonator with an 850 nm $\times$ 2 µm cross-section [Fig 5.1(a)]. In an LPCVD furnace, we deposit alternating layers of low loss silicon nitride and high temperature SiO_2 oxide (HTO) with thickness 100nm and 50nm, respectively, totaling 6 layers each. We then follow the same fabrication procedures as outlined in [42]. After cladding, we etch trenches on either side of the waveguide down through the buried oxide (BOX) and sputter platinum electrodes on top of the waveguide and aluminum electrodes into the trenches [Fig. 5.1(a)]. With this electrode configuration, we can create a horizontal [Fig.5.1(d)] or vertical [Fig. 5.1(e)] electric field in order to probe multiple components of the EO tensor, r_{ij}.

5.3 Experimental Results

We measure the maximum EO coefficient of silicon nitride to be 8.31 ± 5.6 fm/V in the r_{31} and r_{32} directions, and demonstrate EO modulation with an RC-limited bandwidth of 500 MHz. A modulation peak at 1 GHz is shown in [Fig. 5.2(a)]. We measure the bandwidth of our EO modulation to be approximately 500 MHz, which is RC-limited [Fig. 5.2(b)]. The modulation response exhibits a linear relationship vs. driving power. The slope of one confirms that the modulation is due to the linear EO effect. For the EO effect, refractive index change is proportional to the applied voltage. Modulation due to thermal effects, which are proportional to the square of voltage, would have a slope of two. The response was taken at both 3 MHz and a 1 GHz [Fig. 5.2(c)] to further rule out thermal effects, which decrease beyond 100 kHz.

We are able to measure four components of the EO tensor of the multi-slot

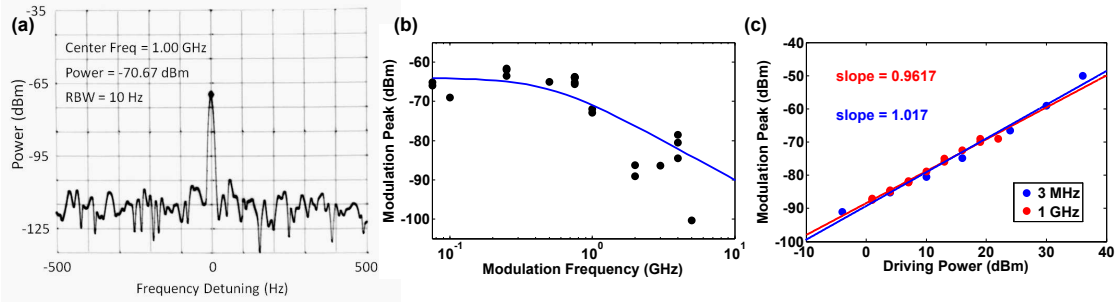

Figure 5.2: (a) Electro-optic modulation peak at 1 GHz. (b) Measured bandwidth of EO modulation is RC-limited with an approximate 3-dB bandwidth of 500 MHz. (c). Linear EO modulation of silicon nitride, in which the modulation peak is linearly proportional to the modulation driving power. This response was measured at both 3 MHz and 1 GHz modulation frequency.

silicon nitride waveguide. The change in refractive index due to an applied electric field is given by:

$$\Delta\left(\frac{1}{n^2}\right) = \sum_j r_{ij} E_j \tag{5.1}$$

in which E_x and E_y are horizontal components of applied electric field and E_z is the vertical component. We assume silicon nitride and SiO_2 to be isotropic materials, so that the bottom half of the EO tensor is zero. We measure r_{ij} to be:

$$r_{ij} = \begin{pmatrix} r^{*}_{TE,H} & r^{*}_{TE,H} & r_{TE,V} \\ r^{*}_{TE,H} & r^{*}_{TE,H} & r_{TE,H} \\ r^{**}_{TM,H} & r^{**}_{TM,H} & r_{TM,V} \\ 0 & 0 & 0 \\ 0 & 0 & 0 \\ 0 & 0 & 0 \end{pmatrix} = \begin{pmatrix} 3.04^{*} & 3.04^{*} & 0.16 \\ 3.04^{*} & 3.04^{*} & 0.16 \\ 8.31^{**} & 8.31^{**} & 1.04 \\ 0 & 0 & 0 \\ 0 & 0 & 0 \\ 0 & 0 & 0 \end{pmatrix} \text{fm/V} \tag{5.2}$$

The tensor components are labeled for the optical field polarization and the applied electric field direction orientation. For a circular electrode geometry, the

horizontal applied field traverses both in-plane directions, and thus we are only able to identify the average effect across these TE and TM tensor components (marked separately with * and **, respectively). The strongest EO coefficient that we measure is for the TM polarization with an in-plane applied electric field, which indicates the expected enhancement due to interface interactions. This improvement opens an opportunity to further investigate interfaces as well as in-plane stress engineering as possible routes to further increasing the EO effect of Si_3N_4. With an improved second-order nonlinear response, Si_3N_4 can become an ideal deposited photonics platform to be used in many high speed and low-loss applications.

CHAPTER 6

TUNABLE FREQUENCY COMB GENERATION BASED ON DUAL MICRORING RESONATORS

6.1 Introduction

In order to achieve efficient and versatile microresonator-based comb generation, active tuning of the cavity coupling condition as well as the cavity dispersion is necessary. Currently, the pump power and cavity detuning are variable parameters used to control the nonlinear interaction, whereas other parameters such as the dispersion, Q factor, and cavity coupling condition are static and are fixed during fabrication. The coupling ratio controls the intensity of the pump and generated comb modes propagating in the resonator and the intensity coupled out of the cavity. Furthermore, it also determines the efficiency of the overall comb generation process [101]. The dispersion has a key role in phase-matching the four-wave mixing (FWM) process, and thus determines the bandwidth of the generated comb. Coupling and dispersion are both designed based on waveguide geometry, so they are generally both immovable. Inherent fabrication variation of dimensions and loss rate also leads to a significant uncertainty of resonance extinction for any designed structure. Post-fabrication extinction control would enable full optimization of device efficiency and increase total device yield. Such a tunable device would be versatile enough to generate a comb of arbitrary bandwidth and optimized efficiency.[1]

Tuning the coupling between the bus waveguide and resonator is challenging since in standard passive monolithically-integrated structures, the coupling

[1]Portions of this chapter are reproduced with permission from [102]

gap is fixed by design and cannot be changed after fabrication. Demonstrations of tunable comb generation have included resonance frequency tunability, which enables control over the operating wavelength. Such tuning has been achieved during comb generation via both thermal and electro-optic means [11, 80, 103]. Coupling gap tunability enables greater control over the comb generation process, allowing for optimization of comb efficiency [101]. Coupling tunability has been demonstrated in integrated silicon devices using a Mach-Zehnder interferometer (MZI) coupler [104–106]. However, the coupling produced by this MZI structure inherently has a sinusoidal wavelength dependence, which can be detrimental to broadband comb generation. Coupling gap tunability can occur in suspended microtoroid and wedge resonator structures, since the devices are operated using suspended tapered fibers [20]; however, this approach requires highly stable fiber positioning with accuracy on the scale of tens of nanometers in order to achieve controllable tuning.

6.2 Device Design

Here, we show a dual-cavity coupled microresonator structure in which tuning one microring resonance frequency induces a change in the overall cavity coupling condition, as evident in the transmission extinction ratio. Our structure consists of two identical microring resonators evanescently coupled to each other, with one ring coupled to a bus waveguide [Fig. 6.1(a)]. Due to the evanescent coupling, the two resonant cavity modes hybridize to form a coupled eigenmode system, in which two superposition eigenmodes ("supermodes") are formed: a symmetric (s) and an anti-symmetric (as) mode. These two new eigenmodes exhibit modified resonant frequencies, according to:

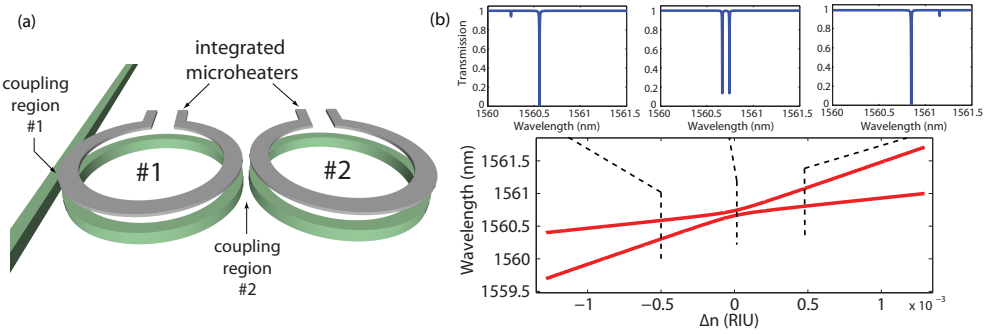

Figure 6.1: (a) Schematic of dual-cavity coupled microring resonator with integrated microheaters. (b) Simulated mode anti-crossing curve as a function of effective mode index detuning between the two microrings. Ring #2 is tuned while ring #1 is kept constant. The modes exhibit an avoided crossing at zero detuning due to the inter-ring coupling. Insets above are simulated transmission spectra showing varying extinction across the anti-crossing.

$$\omega_{\text{s, as}} = \omega_{\text{avg}} \pm \sqrt{\frac{\Delta\omega^2}{4} + \kappa_\omega^2} \tag{6.1}$$

in which ω_{avg} is the average of the individual cavity resonance frequencies, $\Delta\omega$ is the difference between the individual cavity resonances (cavity detuning), and κ_ω is the inter-ring temporal coupling rate. If the cavities are degenerate ($\Delta\omega = 0$), the supermode resonances are split apart from the isolated cavity resonance frequency by $\pm\kappa_\omega$. When the inter-ring coupling rate exceeds the individual cavity decay rate, distinct doublet resonances form at each cavity free spectral range (FSR). As the detuning between the two cavities is varied, a characteristic anti-crossing shape is formed, as in Fig. 6.1(b). At zero detuning, light resonantly couples between the two rings, resulting in an equal distribution of light in both cavities [Fig. 6.1(b), middle inset], and thus equal extinction in both doublet resonances. However, as the cavity detuning increases, the distribution of light becomes unequal as the resonant coupling between cavities becomes

less efficient. Far from zero detuning, the modes are less hybridized, and most of the light in each of the doublet resonances is concentrated in only one ring or the other [Fig. 6.1(b), left/right insets]. The change in detuning also causes the effective cavity length to change, which alters the balance between the round-trip loss and the bus-waveguide coupling. This modifies the loaded-Q. The intrinsic-Q remains unchanged, as long as both cavities have the same loss rate. Figure 6.1(b) shows the simulated doublet resonance shape for three detuning positions along the anti-crossing curve, showing the strong asymmetry in extinction away from zero-detuning. During preparation of this manuscipt, the authors became aware of related work by Xue, et al., which also implements the dual-ring geometry for frequency comb applications [47].

We engineer the ring coupling conditions in order to enable highly efficient, wide extinction tunability. Using a transfer matrix approach, we simulate this structure for high-Q silicon nitride (Si_3N_4) cavities. Along the mode anti-crossing [Fig. 6.1(b)], the varying mode interaction causes the resonance extinction to change significantly; this provides our desired tunability. The device consists of two coupling regions that control the mode interactions: the ring-to-bus coupling region and the inter-ring coupling region. The ring-to-bus coupling controls the range of accessible extinctions, and the inter-ring coupling controls the efficiency of the tuning. We plot the resonance extinction along the anti-crossing for various ring-to-bus coupling conditions, shown in Figs. 6.2(a)–6.2(c). For all three cases, the extinction approaches a constant value at large detunings when the rings are essentially decoupled, and goes through a steep transition near zero detuning. The shorter- and longer-wavelength resonances exhibit opposite trends about zero detuning. The maximum overall coupling-condition for the dual cavity occurs at large detunings, when light is localized

entirely in the first cavity, with minimum perturbation from the second cavity. As the second cavity couples more strongly with the first (at smaller detunings), light becomes distributed throughout both rings, effectively decreasing the coupling to the bus waveguide. With heaters to independently tune the cavity resonance frequencies, we can therefore tune the extinction simply by applying

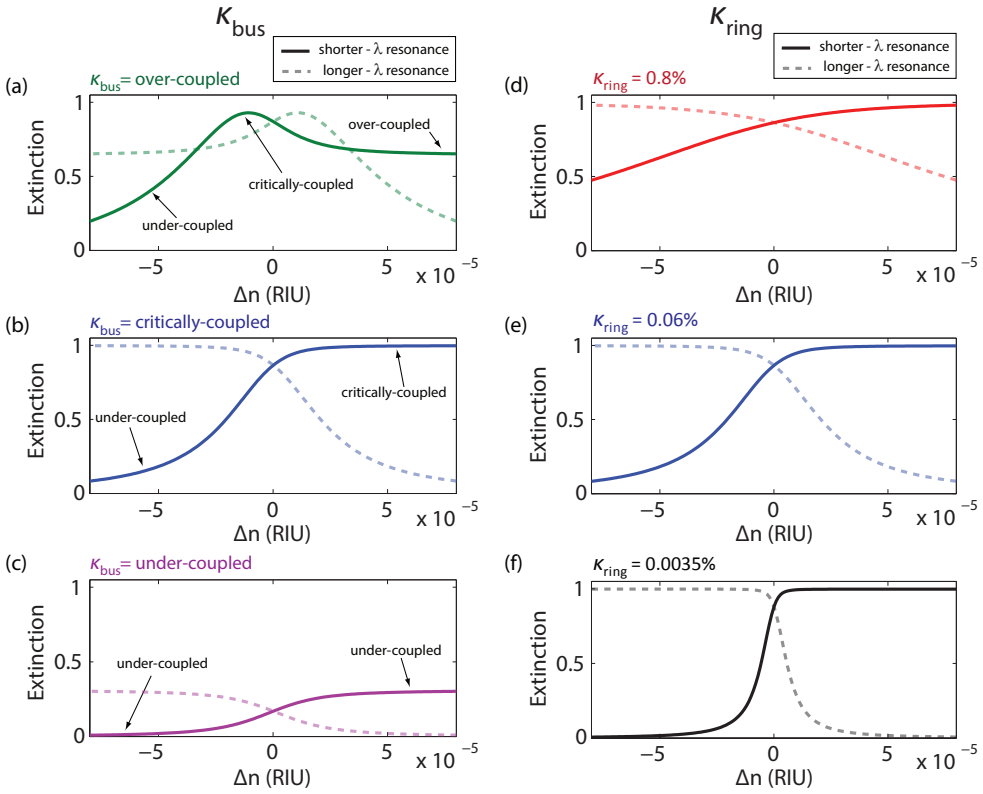

Figure 6.2: (a) Simulated extinction vs. ring detuning shown for under-coupled ring-to-bus coupling condition. Ring-bus coupling determines the maximum possible coupling condition of the full structure. The extinction approaches a constant value at large detunings, and goes through a steep transition near zero detuning. (b) Extinction curve for critically-coupled ring-bus coupling condition. (c) Extinction curve for over-coupled ring-bus coupling condition. (d-f) Extinction vs. ring detuning shown for three different inter-ring coupling values. The lowest inter-ring coupling exhibits the steepest slope, indicating a higher extinction tuning efficiency. The resonance linewidth determines the maximum achievable efficiency.

electrical power to the device. In Figs. 6.2(d)–6.2(f), we show that the tuning efficiency, i.e. the slope of the extinction response with Δn, can be tailored by engineering the inter-ring coupling rate. By decreasing the coupling rate, the anti-crossing response becomes sharper, which improves the tuning efficiency. The upper bound on efficiency occurs when the inter-ring coupling is on the order of the cavity decay rate. Therefore, a higher Q enables higher-efficiency tuning. For example, a cavity with a Q-factor of 2×10^6 can tune the extinction from a 1 dB under-coupled resonance to 11 dB with a refractive index shift of 1.4×10^{-5}. For a Si_3N_4 structure (exhibiting a thermo-optic coefficient of 4×10^{-5} RIU/K) with heaters as described below, this tuning would require a low power budget of approximately 1 mW of heater power.

Our fabricated devices consist of coupled high-Q Si_3N_4 microresonators with tunable extinction ratio via integrated microheaters. We fabricate a dual coupled microresonator in Si_3N_4 with cross-sectional dimensions 950 × 1400 nm. The structures are fabricated using a process similar to the one described in [42]. Our fabricated devices have an intrinsic Q-factor of approximately 2×10^6, and radii of 115 µm as well as 75 µm, yielding devices with FSR's of 200 GHz and 500 GHz, respectively. This cross-section yields anomalous group-velocity dispersion (GVD) (β_2 = -180 ps^2/km) at our pump wavelength of 1560 nm critical to ensure phase matching for parametric comb generation [79]. We do not observe a decrease in intrinsic-Q compared to equivalent single-ring devices; this can enable equivalent comb performance in the dual-ring device. Above the waveguide cladding, we fabricate integrated microheaters by sputtering platinum and using a lift-off approach, yielding a cross-section of 100 nm tall by 6 µm wide. We position the heaters 1.9 µm above the waveguide to ensure negligible optical loss while maintaining close proximity for efficient heat delivery.

These heaters yield an efficiency of 1.35×10^{-5} RIU/mW. We can control the heater power to within 7 μW, resulting in a resonance wavelength accuracy of 7 MHz, which is well below the cavity linewidth. A micrograph of the 200 GHz FSR device is shown in Fig. 6.3(a).

6.3 Device Characterization

6.3.1 Tunable Extinction

The fabricated devices demonstrate good agreement with the simulated extinction tuning. Using the integrated microheaters, we first tune ring #2 while keeping ring #1 constant. In order to achieve blue detuning ($\Delta n < 0$), we bias heater #1 above room temperature. The blue data points in Fig. 6.3(b) are measured resonance positions as the heater on ring #2 is tuned. The red line in Fig. 6.3(b) is a curve fit based on Eq. (6.1), with an additional parameter included to account for thermal cross-talk between the two rings. There is good agreement between theory and experiment. In Figs. 6.3(c) and 6.3(d), we plot the measured extinction as a function of detuning for a critically-coupled device and an over-coupled device, respectively. We see an experimental trend that matches the theoretical curves very closely in Fig. 6.2(b) and Fig. 6.2(a), respectively. Figure 6.3(e) shows our ability to compensate for the overall wavelength shift as the extinction is thermally tuned. By tuning both heaters independently for each ring, we are able to compensate for this wavelength shift, and demonstrate 13.3 dB of tuning of the resonance extinction, from 0.7 dB to 14 dB. Since we can keep the resonance in place as the extinction is tuned, this device is useful for

real-world applications involving single-frequency lasers.

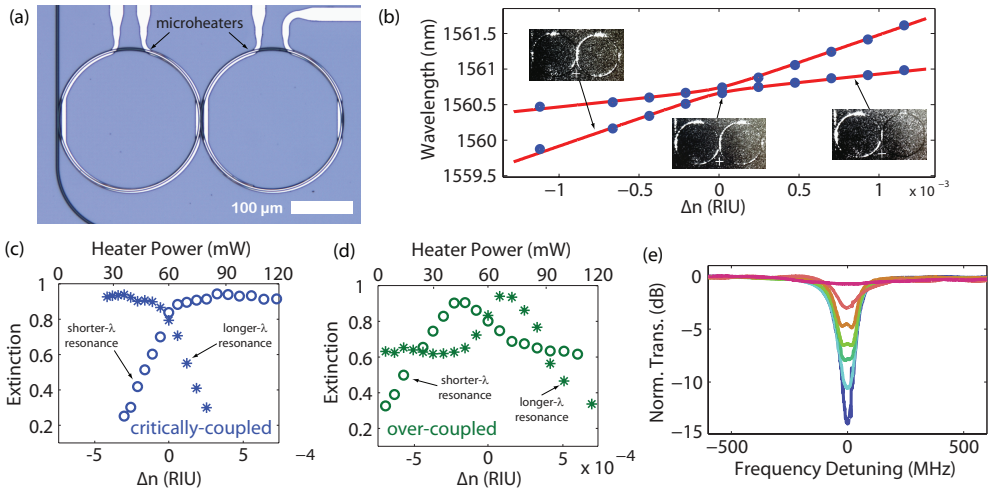

Figure 6.3: (a) Micrograph of fabricated dual-cavity device with integrated platinum microheaters. (b) Measured (blue points) mode anti-crossing curves with theoretical curve fit (red line). Ring #2 is tuned while ring #1 is kept constant. The inset infrared micrographs show spatial light distribution among the two rings for 3 different positions along anti-crossing. Only the lower-wavelength resonance is shown here. A small thermal cross-talk is present between the two rings resulting in an observed tilt in the anti-crossing shape. (c) Experimental measurement of extinction vs. detuning for a critically-coupled device and (d) for an over-coupled device. Ring #2 is detuned while ring #1 is kept constant. Extinction response matches theoretical trend in Fig. 6.2(a)-(b). (e) Experimental measurement of extinction tuning at a fixed wavelength by using heater #1 for compensation. As heater #2 is increased, heater #1 is decreased in order to keep the resonance wavelength fixed.

6.3.2 Tunable Modal Dispersion

We show that the dispersion introduced by the coupled cavity geometry is highly tunable, and present a new method for dispersion engineering using modal dispersion. In general, the dispersion of the inter-ring coupling region

is more than one order-of-magnitude smaller than the magnitude of the waveguide dispersion, and thus has a very small effect on the total dispersion. Here, however, we harness the anti-crossing effect to create a much higher dispersion, which is also tunable. Dispersion due to higher-order mode-crossings has been investigated recently in Liu, et al [46]. Here, we realize this dispersion tunability using a Vernier structure, by ensuring that one ring has a different round-trip optical path length than the other [107–110]. Having different FSR's, these cavity resonances operate at different ring detuning values across the spectrum, and thus the resonance splitting becomes wavelength dependent. The supermode resonance position can be represented in terms of the difference in FSR between the two cavities, Δ_{FSR}, and the cavity mode number, m. We rewrite Eq. (6.1) in this form:

$$\omega_{\text{s, as}} = \omega_1 + \frac{\Delta_{FSR}(m - m_0)}{2} \pm \sqrt{\frac{\Delta_{FSR}^2(m - m_0)^2}{4} + \kappa_\omega^2}, \tag{6.2}$$

where ω_1 is the resonance frequency of the first cavity,κ_ω is the inter-ring temporal coupling rate, and $m_0 = n\omega_1 R/c$ is the mode number where the two cavity resonance frequencies overlap, in which n is the effective mode index, R is the radius of the first ring, and c is the speed of light. The Vernier effect [107–110] causes the resonance frequencies to overlap again multiple FSR's away, making this function periodic. Here, we analyze the effect over one period, which can be repeated for adjacent periods. The spectral dependence of supermodes frequency splitting can be expressed as the derivative of the frequency splitting with respect to cavity mode number, m:

$$\frac{d\omega_{\text{splitting}}}{dm} = \frac{\frac{1}{2}\Delta_{FSR}^2(m-m_0)}{\sqrt{\Delta_{FSR}^2(m-m_0)^2/4+\kappa_\omega^2}}. \tag{6.3}$$

This expression is a continuous function in m, but the cavity modes only exist for integer values of m, so the function is sampled at each integer cavity mode. For now, we have neglected the dispersion due to the waveguide geometry and material, which cause a spectral dependence of the FSR. The GVD, β_2, can be expressed in terms of the second derivative of ω with respect to m, i.e. the difference between two adjacent FSR's surrounding mode m [111]:

$$\beta_2 = -\frac{n}{2\pi c\, FSR_\omega^2}\frac{d^2\omega}{dm^2}, \tag{6.4}$$

where FSR_ω is the free spectral range in units of angular frequency, ω. Using (6.2) and (6.4), we derive an expression for the modal GVD of the two supermodes:

$$\beta_{2,\text{s, as}} = \mp\frac{n}{2\pi c\, FSR_\omega^2}\frac{\frac{1}{4}\Delta_{FSR}^2\kappa_\omega^2}{\left[\Delta_{FSR}^2(m-m_0)^2/4+\kappa_\omega^2\right]^{3/2}}, \tag{6.5}$$

where FSR_ω here represents the average FSR of the two rings. The peak modal dispersion value is expressed as:

$$\beta_{2,\text{ max}} = \mp\frac{n}{8\pi c\kappa_\omega}\left(\frac{\Delta_{FSR}}{FSR_\omega}\right)^2, \tag{6.6}$$

and the full width at half maximum (FWHM) bandwidth of the modal dispersion, expressed in units of cavity mode number, m, is:

$$FWHM_m = \frac{4\kappa_\omega}{\Delta_{FSR}} \sqrt{2^{2/3} - 1}. \tag{6.7}$$

There is a trade-off between strength of the modal dispersion [Eq. (6.6)], and the bandwidth [Eq. (6.7)], which are both a function of Δ_{FSR} and κ_ω. It is straightforward to incorporate the waveguide and material dispersion with this modal dispersion in the above equations by accounting for derivative terms of the FSR, omitted here for simplicity. The properties of the modal dispersion can be tailored via the inter-ring coupling and the FSR mismatch, both of which are primarily fixed after fabrication. Additionally, integrated thermal control of the cavity resonance frequencies also allows us to tune the cavity frequency offset, enabling dynamic tunability of the strength of the modal dispersion. Using a fabricated device consisting of rings with slightly different FSR's, we measure the transmission spectrum across 100 nm of wavelength (1520-1620 nm) for multiple values of ring detuning and measure the resonance splitting. The spectral dependence of the resonance splitting across the spectrum, given by Eq. (6.3), is plotted in Fig. 6.4(a) for multiple ring detuning values. Heater #1 is kept at constant power while heater #2 is tuned. The red line is a theoretical fit based on Eq. (6.3) using experimental parameters estimated independently. The experimental data follows the theory well. Two sample spectra corresponding to data points in Fig. 6.4(a) are shown in Figs. 6.4(b) and 6.4(c). For this theoretical fit, we also plot the corresponding modal GVD, based on Eq. (6.5), in Fig. 6.4(d). We see a maximum modal dispersion of ±4.5 ps^2/km. As per Eq. (6.5), the symmetric and anti-symmetric modes acquire opposite dispersion values. The magnitude of this value is small compared to our total waveguide dispersion (β_2 = -180 ps^2/km), which is simply due to a small FSR mismatch for this particular device. For larger FSR mismatch, this modal dispersion value can

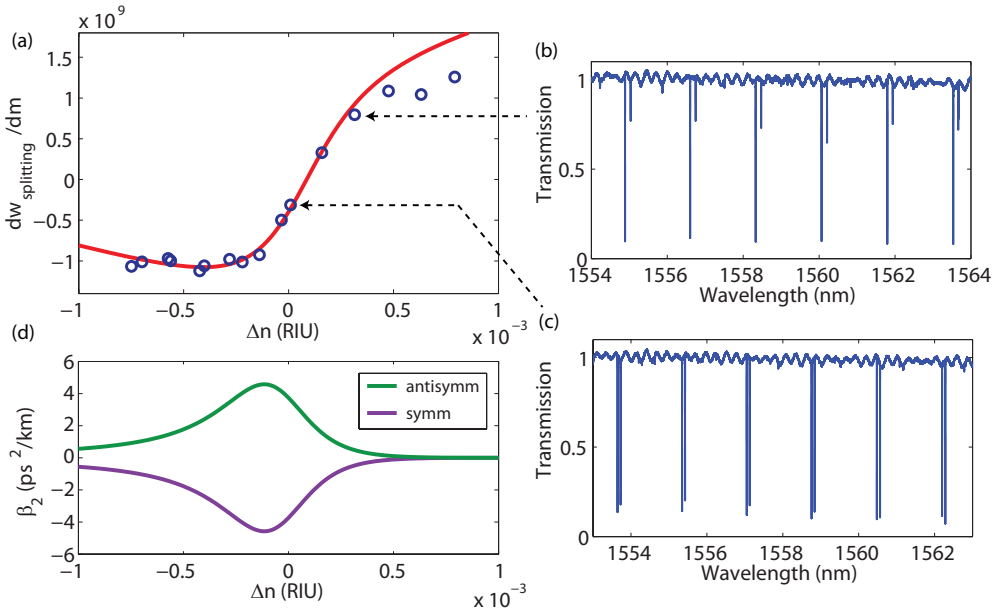

Figure 6.4: (a) Spectral dependence of supermode resonance splitting for multiple ring detuning values. The red line is a theoretical fit based on Eq. (6.3) with experimental parameters estimated independently. Data was obtained by heating ring #1 with a constant 100 mW and sweeping heater #2. Each point represents the slope of the splitting value across 100 nm resonance spectra that were collected. A portion of two of these spectra are shown in (b) and (c). (d) Theoretical modal GVD curves for symmetric and antisymmetric supermodes based on curve fit in (a) using Eq. (6.5).

easily reach upwards of ±1000 ps^2/km or more. Since this large dispersion is also highly tunable, this modal dispersion can be implemented as a powerful tool for dispersion engineering. This modal dispersion provides a critical knob for engineering the GVD of the system for phase-matching nonlinear optical processes.

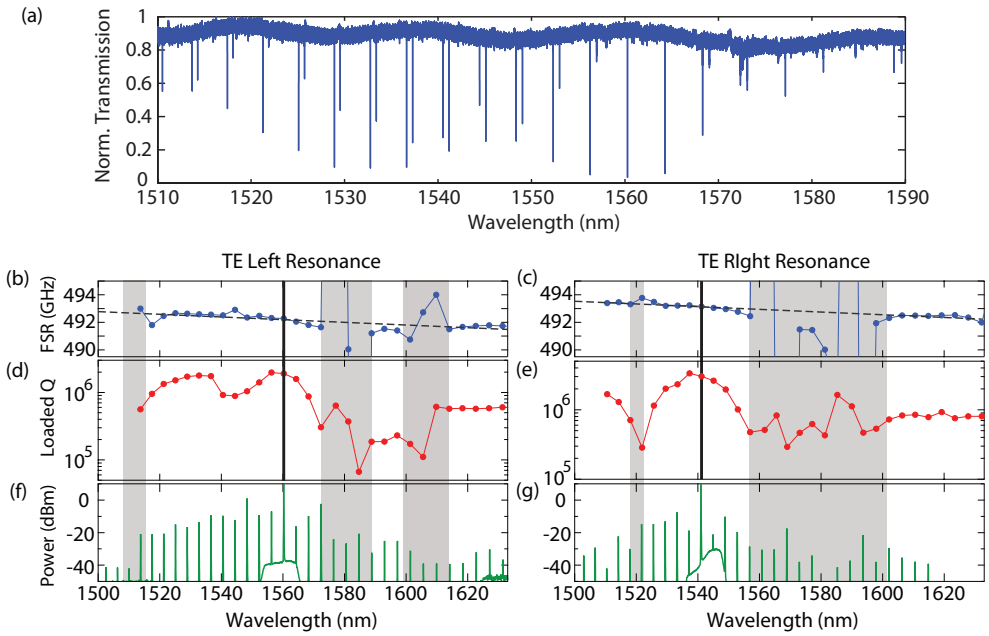

Figure 6.5: (a) Transmission measurement of 500 GHz FSR dual-coupled microring resonator. Measured FSR is shown for (b) lower wavelength resonance and (c) higher wavelength resonance. The corresponding loaded Q is shown for (d) lower and (e) higher wavelength resonance. The generated comb is pumped at (f) 1560 nm on a left resonance and (g) 1540 nm on a right resonance, indicated by solid black vertical lines. The shaded region indicates locations of mode-crossings that cause degradation of the comb line power. Nonetheless, stable, low-noise comb generation is possible by ensuring that the spectral position of these mod crossings is far detuned from the pump.

6.4 Mode-Crossing Characterization

The wide tunability of our device allows us to overcome mode-crossings resulting from strong coupling between different transverse spatial modes – a major challenge for comb generation. Microresonator combs have been generated in multimode structures that can suffer from higher-order mode-crossings throughout the spectrum, originating from the coupling region as well as waveguide bends and the presence of slightly-angled sidewalls [112–114]. Even in

single-mode structures, where no higher-order modes exist, strong polarization mode-crossings can occur. Such mode-crossings can strongly affect the comb generation process due to the localized changes in dispersion, which can prevent soliton formation [115] and distort the amplitude of the generated spectrum [116]. Several studies have taken steps to reduce the presence of higher-order mode coupling [117, 118]. When mode-crossings occur, one expects the FSR to deviate strongly from the expected value, accompanied by a reduction in the Q caused by the significantly enhanced losses of the higher-order modes. In order to characterize the mode-crossings in the dual-cavity structure, we measure the FSR and loaded Q of both supermodes of a 500 GHz FSR dual-cavity device. The transmission measurement of the dual-coupled microring is shown in Fig. 6.5(a) and the measured FSR and the loaded Q factor are shown in Figs. 6.5(b)–6.5(e). The resonance wavelengths are precisely determined using a laser-based precision measurement of the wavelength-dependent FSR, which allows for measurement of the FSR with a relative precision of 10^{-4} [119]. The measurement indicates that the presence of mode-crossings severely disrupts the resonance frequency position. For the left resonances, we observe large higher-order mode-crossings at 1570 nm, 1585 nm, and 1610 nm, which result in significant deviations in the FSR and additional small mode-crossings at 1520 nm and 1545 nm. For the right resonances, we observe large higher-order mode-crossings at 1560 nm and 1585 nm and a small mode-crossing at 1525 nm. These regions are indicated by gray sections in Figs. 6.5(b)–6.5(g). The corresponding loaded Q characterization shows that the large mode-crossings are accompanied by a significant reduction in the Q caused by the significantly enhanced losses of the higher-order modes. As a result, pumping at these wavelengths hinders the generation of a stable comb due to insufficient power enhancement

in the cavity. However, as shown in Fig. 6.5(f) and 6.5(g), by ensuring that the spectral position of these mode crossings is far detuned from the pump at 1560 nm and 1540 nm for the left resonances and right resonances, respectively, we are able to generate a stable, low- comb with 1.5 W of pump power. The generated spectra show some asymmetry, largely due to the presence of the large mode-crossings. In addition to altering the spectral position of the resonance, these mode-crossings reduce the cavity enhancement and subsequently restrict the comb bandwidth.

We demonstrate that this device can be used to avoid mode-crossings by dynamically tuning the position of a mode-crossing. The ability to dynamically control the position of mode-crossings is vital particularly for many applications that cannot rely on the tuning of the pump source. Beginning with an as-fabricated 200 GHz FSR dual-cavity device with 100 mW of heating on ring #1 [Fig. 6.6, blue curve], we observe a mode-crossing at 1548 nm, indicated by a local decrease in extinction for a single FSR resonance. When we sweep the resonance of ring #2 by 0.4 nm (heater power from 0 to 40 mW), we observe that the mode-crossing shifts across the spectrum by over 3 nm (2 FSR's), which is almost an order of magnitude larger than the ring resonance shift. Therefore, we can tune the mode-crossing with high-efficiency. This high tuning efficiency is due to the anti-crossing behavior of the dual cavity structure. This novel degree of freedom can be used for comb generation optimization.

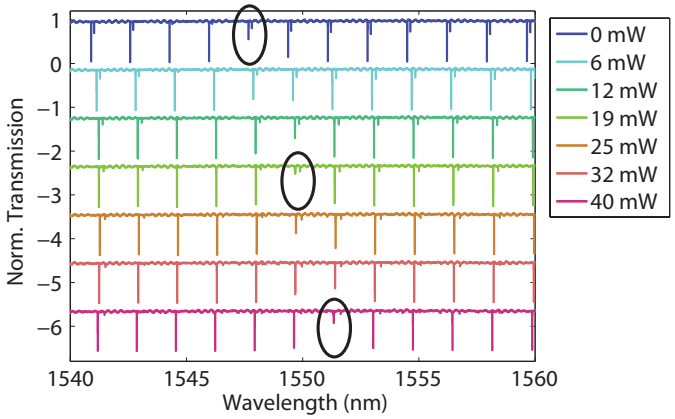

Figure 6.6: Demonstration of mode-crossing tunability using a 200 GHz FSR dual-cavity device. Ring #1 is heated with 100 mW and ring #2 is swept with heater power indicated in the legend. A mode-crossing (circled) is tuned across two FSR's while the overall position of the desired resonances shifts only 0.4 nm.

6.5 Experimental Results

We harness the ability to tune the resonance extinction to optimize frequency comb generation efficiency and show a 110-fold improvement in the comb efficiency. We generate frequency combs in this structure at different ring detuning values and monitor the resonance extinction [Fig. 6.7(a)–6.7(c)] as well as the spatial distribution of light [Fig. 6.7(d)–6.7(f)]. Here we use a 200 GHz FSR dual-cavity device and pump using a single-frequency tunable diode laser amplified by an erbium doped amplifier. We couple into the chip using a lensed fiber, and measure approximately 5 dB coupling loss, yielding a pump power of approximately 600mW in the bus waveguide. We monitor the output of the comb on an optical spectrum analyzer (OSA). We observe different distributions of light across both rings according to their resonance detuning. In Figs. 6.7(e) and 6.7(f), the pump is tuned into a resonance that lies on opposing sides of the coupling anti-crossing position, where the light is primarily localized in ring #1

or in ring #2, respectively. We are able to tune the comb generation efficiency from degraded efficiency up to optimal performance [Fig. 6.7(g)–6.7(i)]. We define our generation efficiency as the ratio of the total power in the comb lines divided by the pump power dropped into the ring. We measure this by taking the input laser power, subtracting the facet coupling loss, and subtracting the power measured in the OSA, which is the left-over pump that was not dropped into the cavity. We see a 40-fold improvement in efficiency from the comb in Fig. 6.7(g) (blue) to the comb in Fig. 6.7(h) (red), with efficiency increasing from 0.018% to 0.7% efficiency, respectively. Further, we are able to achieve a 110-fold improvement from the comb in Fig. 6.7(g) (blue) to the comb in Fig. 6.7(i) (violet), with efficiency increasing from 0.018% to 2% efficiency, respectively. We note that, as shown in Bao, et al., an increase in coupling condition (indicated by the increase in extinction from Fig. 6.7(a) to (c)) yields an improvement in overall comb efficiency [101]. For all three combs, all other experimental conditions, particularly pump power, were kept unchanged. This device can replace conventional single-ring comb devices, not because it can achieve a higher efficiency than a single-ring device, but because of its post-fabrication tunability. This eliminates the problem of fundamental fabrication variations, allowing for optimized device yield and high efficiency performance across all devices.

We demonstrate open eye diagrams using the comb lines as a wavelength-division multiplexing (WDM) channel. For WDM applications [120–122], power consumption is a critical factor, and the comb bandwidth should be confined to the operational wavelength range of the WDM system with high conversion to the comb lines. Furthermore, for the generated comb to be used as a multiple wavelength WDM source, low RF amplitude noise is required. We investigate the comb generation dynamics and the properties, in particular, to determine

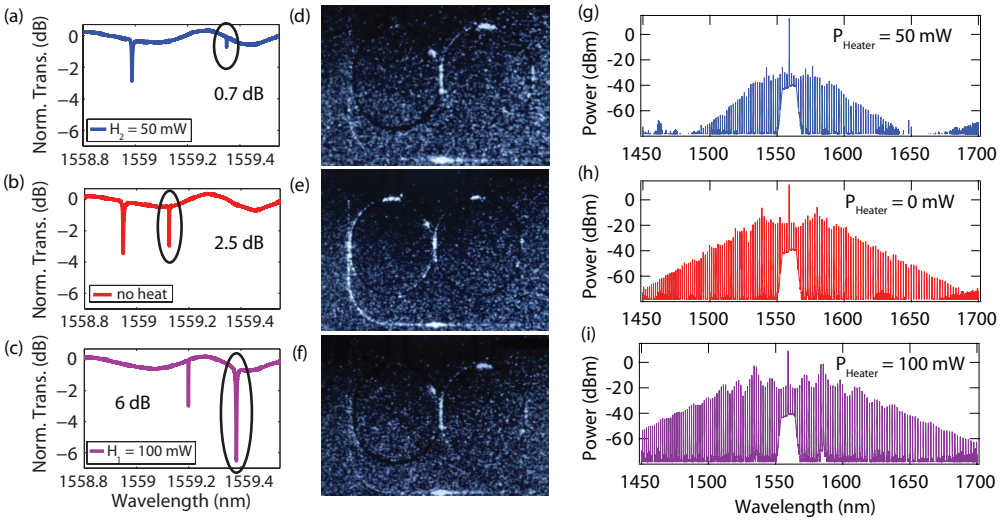

Figure 6.7: (a)-(c) Spectrum showing extinction tuning using left heater (H_1) and right heater (H_2). (d)-(f) IR camera photos showing spatial distribution of light during comb generation. (g)-(i) Comb generation with extinction tuning, with (i) as the maximum efficiency comb achieved of 2%.

the stability of a comb line. We pump the resonator at 1560 nm for comb generation. To monitor the comb generation dynamics, we measure the optical and RF spectra, as well as the eye diagram through modulation of a single comb line. For the eye diagram, we use a 1 nm tunable filter to pick-off a single comb line which is modulated with a $2^{31} - 1$ non-return-to-zero pseudo-random bit sequence (NRZ PRBS) at 10 Gb/s and sent to a high-speed sampling oscilloscope for characterization. Figure 6.8 (a)–6.8(c) shows the measured optical spectra, RF spectra, and the eye diagram, respectively, as the pump wavelength is tuned into resonance (top to bottom). While the optical spectra show no significant changes, the RF spectra show that the comb undergoes a transition to a low RF amplitude noise state, similar to behavior observed previously [123]. Furthermore, the eye diagram illustrates the behavior of the comb at a single resonance. In the high-noise state (top, middle), the eye shows poor signal-to-noise and significant distortion, which can be attributed to the fast intensity fluctuations

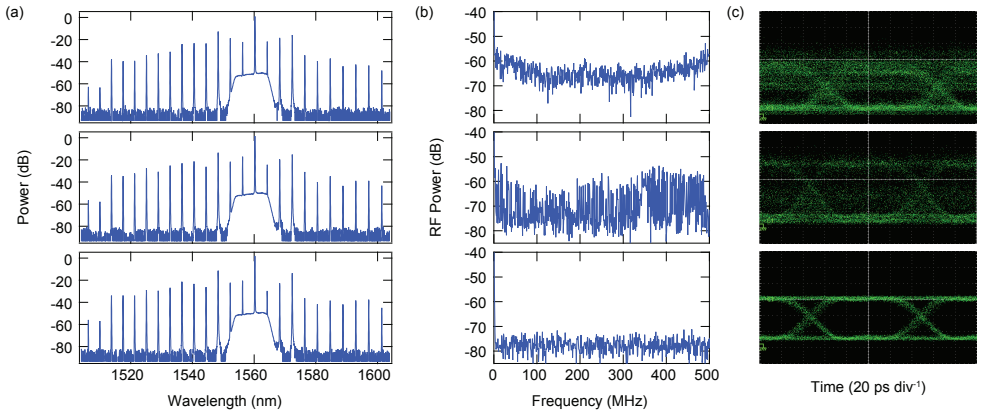

Figure 6.8: Comb generation dynamics for 500 GHz FSR microresonator as pump wavelength is tuned into resonance (top to bottom). Plot shows (a) optical spectra (b) RF spectra, and (c) eye diagram of single comb line that is filtered and modulated with a 10 Gb/s PRBS.

of multiple comb lines within the single resonance through various FWM processes. As the pump is tuned further, the signal-to-noise further degrades to the point where the eye is completely closed, which corresponds to comb instability from chaotic-like behavior [57]. Once the comb transitions to the low phase noise state, the eye diagram shows good signal-to-noise. Our results indicate that, even with mode-crossings in close proximity in wavelength, it is possible to generate a stable, low-noise comb suitable as a multiple wavelength source for WDM applications.

Our design can be used for active optimization of comb efficiency, stabilization, and can be potentially useful for active control of mode-locking behavior. Our observation of the strong dispersion tunability of this device holds promise for creating tunable bandwidth combs as well as fundamentally extending beyond conventional dispersion engineering to enable novel comb generation regimes, such as at visible wavelengths. Further, active feedback on microresonator combs using integrated thermal tuning can provide the versatility

and robustness needed to allow chip-based frequency combs to operate in real-world sensing, optical clock, and frequency metrology applications.

CHAPTER 7

LOW-LOSS SILICON PLATFORM FOR BROADBAND MID-INFRARED PHOTONICS

7.1 Introduction

In order to further extend the wavelength range of microresonator frequency combs to longer wavelengths, we now use silicon as our waveguide material. Silicon photonics has revolutionized optics in the near IR spectral range but has had limited impact on optics in the mid-IR range, primarily because of the platform's intrinsic material absorption. Within the mid-IR wavelength range, many common molecules relevant to real-world sensing applications have strong absorption signatures, forming the so-called "molecular fingerprint" spectral region [124]. Numerous forms of optical spectroscopy have been developed for biological, chemical, environmental, and industrial applications, with an increasing need for compact and inexpensive sensors enabled by integrated photonics [124]. The advancement of quantum cascade lasers has paved the way for growth of compact, chip-scale mid-IR photonic applications [24, 125, 126]. Concurrently, silicon photonics has transformed near-IR telecommunications technologies while leveraging the immense silicon fabrication infrastructure of the electronics industry [127, 128]. Despite their development in tandem, silicon photonics has long been considered unsuitable for mid-IR applications due to its lack of broad transparency beyond the near-IR range. The transparency window of the silicon waveguide core extends to 6-8 μm wavelength [129, 130], whereas the silicon dioxide (SiO_2) cladding material begins absorbing strongly around 3.5 μm [131]. Therefore, few demon-

strations of silicon-on-insulator (SOI) waveguides have operated past 2.5 μm [132–138]. While mid-IR platforms based on crystalline fluorides [25, 26], germanium [9, 139–144], chalcogenide materials [36–40] have been demonstrated with low loss, integrated photonics structures on a silicon chip in this spectral range have yet to be demonstrated.

Recently, efforts have been made to develop mid-IR photonics on a silicon platform based suspended structures and sapphire substrates; however, to date these have not been able to yield low loss optical structures. The challenge of incorporating alternative cladding materials for silicon-based mid-IR photonics lies in achieving broadband transparency while ensuring low propagation loss with minimal fabrication complexity. Removing the oxide cladding to form either a pedestal or fully suspended SOI waveguide can greatly reduce or eliminate the absorption loss, extending the platform's transparency window [145–152]. However, this approach can introduce fabrication complexity as well as challenges for the device's thermal stability and low scattering losses. To increase robustness, the under-cladding can instead be replaced by a more transparent material, such as sapphire (transparent out to 4.5 μm). Silicon-on-sapphire is commercially available and has been extensively studied [27–35]; however, it is a hard material that is difficult to etch, leading to scattering losses. Additionally, Chen et al. have recently demonstrated a platform based on silicon on calcium fluoride (CaF_2), which extends the transparency window even further [153]. However, this platform introduces significant complexity, requiring completely custom fabrication processing techniques.

7.2 Low Loss Platform

Here, we demonstrate the ability to leverage silicon photonics to achieve broadband low propagation losses below 1 dB/cm in the mid-IR (comparable with the losses achievable in the near-IR spectral range) by tailoring the waveguide cross-sectional geometry. The primary source of loss for mid-IR silicon waveguides comes from absorption of the mode that overlaps partially with the oxide cladding, which surrounds the waveguide core on all sides. The degree of mode overlap with the cladding, particularly for high-index contrast waveguides, can be tailored by varying cross-sectional geometry as well as index contrast, wavelength, and polarization. Here, in order to minimize these losses, we engineer the mode to minimize propagation loss. Fig. 1 shows the simulated absorption losses for different waveguide geometries, including a traditional silicon photonic waveguide for this wavelength with cross-sectional dimensions 500 nm $\times$ 1400 nm (as in [59]), using finite element method (FEM) simulations of optical modes in COMSOL Multiphysics software. We account for the cladding oxide absorption, adapted from literature [131], which we plot in Fig. 7.1 (blue curve). The losses are extracted from the imaginary component of the simulated mode effective refractive index, k, from which we calculate propagation power loss, $\alpha = 4\pi k/\lambda$. One can see that the loss increases significantly at mid-IR wavelengths as the mode grows larger into the cladding, exceeding 10 dB/cm, which is prohibitive for most waveguiding applications. If we remove the top cladding, we see a modest improvement in loss, limited still by the large remaining overlap with the under-cladding, as seen in the inset mode picture. By using an unconventional air-clad waveguide geometry with 2300 nm $\times$ 4000 nm cross-section, we are able to significantly decrease the loss at higher wavelengths by

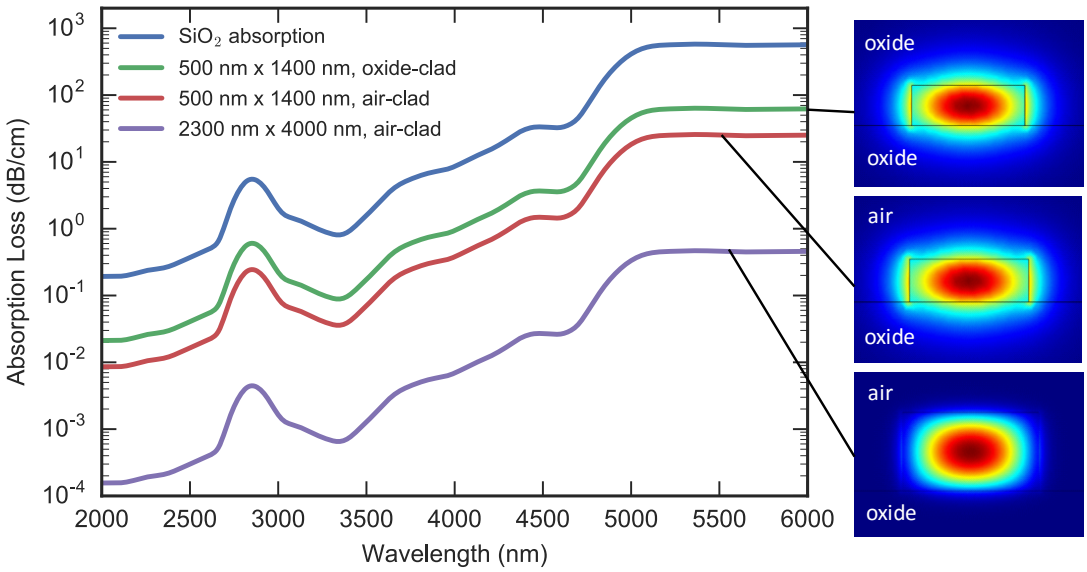

Figure 7.1: Simulated absorption losses for different waveguide cross-sectional geometries, including a traditional silicon photonic waveguide for this wavelength with cross-sectional dimensions 500 nm × 1400 nm (as in [59]) as well as our air-clad waveguide with cross-sectional dimensions 2300 nm × 4000 nm. The cladding oxide absorption, adapted from literature [131], is plotted in the blue curve. One can see that the air-clad geometry shows a two order-of-magnitude loss improvement compared to the oxide-clad geometry

more than two order-of-magnitude loss improvement over the oxide-clad waveguide. As evident in the inset mode pictures, the optical mode for this geometry overlaps minimally with the oxide under-cladding compared to the traditional cross-section. For this geometry, the propagation loss remains below 1 dB/cm up to a wavelength of 6 µm (corresponding to a Q factor > 10^5) and below 0.1 dB/cm up to nearly 5 µm (Q > 10^6). This broadband silicon photonics transparency window requires no additional fabrication complexity.

We fabricate an integrated air-clad silicon microring resonator and waveguide, using conventional silicon fabrication processing followed by a chem-

ical treatment of the surfaces to ensure low propagation losses. For our substrate, we use a commercially available SOI wafer from Ultrasil Corporation with a 2.3 µm top silicon film thickness, and 3 µm buried oxide thickness. The top silicon film is high resistivity Float-Zone silicon, with a resistivity >4,000 Ωcm, corresponding to an intrinsic doping concentration of $< 1\times10^{13}$ cm^{-3}. This high resistivity is advantageous for mid-IR wavelengths to minimize losses due to multi-photon absorption. The process involves fabricating unclad photonic structures, integrated with oxide-clad inverse tapers. The oxide-clad inverse tapers guarantee the taper mode to be delocalized for mode-matching to our input laser beam while remaining above the cutoff condition for the propagating waveguide mode. The taper, which is 200 nm wide at the tip, yields a mode that is designed to overlap with our free-space mid-IR laser beam with a beam width 5 µm. Note that with an under-cladding thickness of 3 µm, we can ensure that there is no leakage into the substrate at the input facet by removing the substrate (30-40 µm) near the edge using xenon difluoride (XeF_2), while using photoresist as an etch mask. We pattern the waveguides via electron-beam lithography using ma-N 2410 electron-beam resist, and fully etch the silicon using an inductively-coupled plasma (ICP) dry etching process with a C_4F_8/SF_6 gas mixture. We then deposit 3 µm of plasma-enhanced chemical vapor deposition (PECVD) silicon dioxide for cladding. In order to remove the cladding above the waveguides and resonators, we pattern a large area (of a few mm) above the waveguides and resonators, dry etch the PECVD oxide, leaving 200 nm, and finally remove the remaining cladding oxide in dilute hydrofluoric acid (6:1 H_2O:HF) wet etch. In order to clean and smooth the surface, we perform a chemical oxidation surface treatment with piranha acid (3:1 H_2SO_4:H_2O_2) and dilute HF, as outlined in [154]. In order to ensure low coupling losses, we then

pattern and etch trenches to define the edge facets of the chip [43], and finally dice the wafer into individual chips. Microscope and SEM images of the fabricated waveguide and microring resonator are shown in Fig. 7.2.

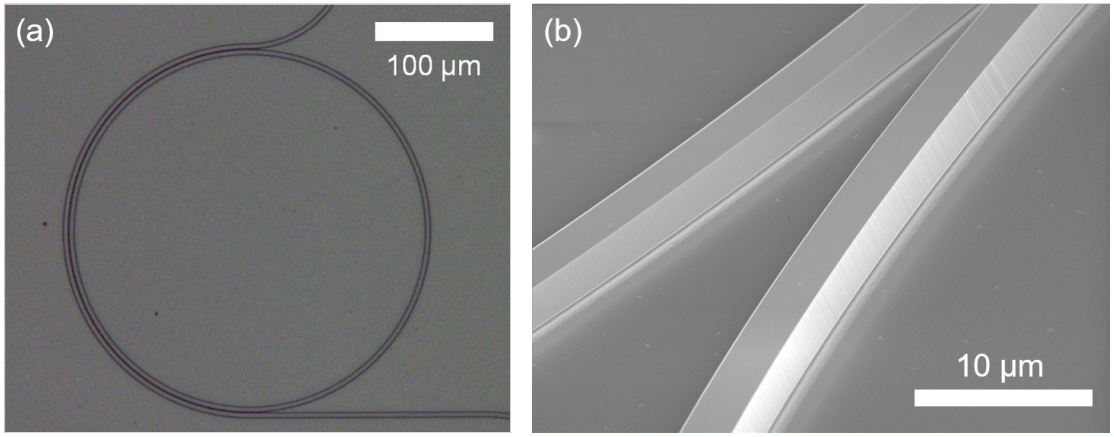

Figure 7.2: (a) Optical microscope image of air-clad SOI microring resonator. (b) SEM image of air-clad waveguides near the resonator coupling region.

7.3 High-Q Microresonator

We measure an intrinsic quality factor greater than 10^6 between a wavelength of 3.5 µm and 3.8 µm, which is the highest Q demonstrated to date in an integrated mid-IR platform. In order to measure the fabricated optical structures, we use as an input mid-IR laser source (Argos Model 2400 CW optical parametric oscillator) that is tunable from 3.2 to 3.8 µm and has a 100 kHz linewidth. After sending the beam through a variable attenuator and a polarization controller, we couple light into the chip through an aspheric lens. We measure an input coupling loss of 8 dB for TE polarization, likely due to an offset between the designed and fabricated dimensions. We collect light from the chip using another

aspheric lens, send it through a polarization filter, and detect using PbSe detector along with a lock-in amplifier and an optical chopper. To measure the Q factor, we modulate the laser wavelength using a triangular wave applied to an internal piezo actuator. We measure a resonance at 3790 nm wavelength (2639 cm^{-1}) and we fit to a lorentzian function. To find the intrinsic Q, we use Eq. 2.17. Assuming an under-coupled cavity condition, we find an intrinsic quality factor of $(1.1 \pm 0.08) \times 10^6$, shown in Fig. 7.3(a). The laser calibration is detailed below. The output polarization of this resonance is rotated away from TE, indicating some polarization rotation occurring inside the chip, likely from the transition into and out of the air-clad region. We measure intrinsic Q at several wavelengths from 3.5 µm to 3.8 µm using devices with varying coupling gaps. Measured results are shown in Fig. 7.3(b) as plotted circles. For comparison, we also measure the intrinsic Q of the oxide-clad resonators used in [59], with a cross-section of 500 nm x 1400 nm,.

7.4 Laser Calibration

For the Argos CW OPO, the piezo actuator acts to tune the pump laser wavelength (centered around 1064 nm) while the signal is held constant, thereby tuning the idler beam at mid-IR wavelengths. We measure the pump wavelength using a wavelength meter to an accuracy of 50 MHz and plot as a function of voltage applied to the piezo element. Performing a linear curve fit given this wavelength error, we extract the fitting error from the covariance matrix, yielding a standard deviation of 500 kHz/V on the slope, which is well within the measurement error.

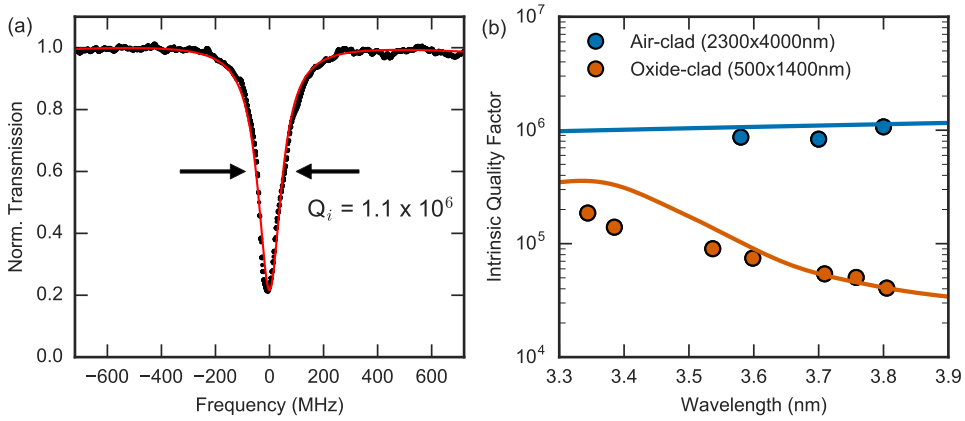

Figure 7.3: (a) Transmission spectrum of the air-clad microring resonator at 3.8 µm wavelength showing an intrinsic $Q \sim 10^6$. (b) Measured (circles) and simulated (solid lines) intrinsic Q as a function of wavelength for our air-clad waveguide geometry (2300 nm × 4000 nm), and for standard oxide-clad geometry (500 nm × 1400 nm). There is good agreement between the trends for simulated and measured Q. One can see that the intrinsic Q depends weakly on wavelength between 3 and 4 µm, in contrast to the standard oxide-clad waveguide geometries.

7.5 Transparency Window

For the geometry used here, we show that both the theoretical and measured intrinsic quality factor depends weakly on wavelength between 3.5 and 4.5 µm, in contrast to the standard oxide-clad waveguide geometries. The theoretical wavelength-dependence of intrinsic quality factor is plotted along with the measured data in Fig 7.3(b). We evaluate the intrinsic quality factor vs. wavelength by extracting the wavelength-dependent absorption from the FEM simulations and the wavelength-dependent scattering using the well-known theoretical model for waveguide scattering loss introduced by Payne and Lacey [155]. We assume loss due to absorption in the cladding and loss due to sidewall scattering to be the major contributions to the total loss. Therefore, given a repre-

sentative measured total loss at 3.8 μm and the relation between Q and loss rate given in Eq 2.16, scattering loss at 3.8 μm can be estimated to be 0.2 dB/cm. Using the Payne-Lacey model with our geometry, we can extract the approximate wavelength dependence of the scattering loss to be λ^{-2}. Thus, quality factor due to scattering loss scales proportional to the wavelength, λ. In Fig 7.3(b), plotted with the measured points are the theoretical wavelength dependent quality factor for both measured devices, considering both absorption and scattering, and see a good agreement between the trends for simulated and measured quality factor. The oxide-clad geometry is clearly absorption-limited, whereas our air-clad geometry remains flat across the spectrum, following closely to the theoretically scattering-limited regime. It is evident that our air-clad geometry achieves a high Q independent of the oxide absorption up to an order of magnitude higher than the traditional oxide-clad geometry, which exhibits a strong decrease in Q with increasing wavelength.

We show that the waveguide geometry used here extends the transparency window to a wavelength of 6 μm. In Fig. 7.4, we plot the wavelength-dependent Q due to absorption, scattering, and total loss for our air-clad geometry from 2 μm to 6 μm. There is a clear transition from the scattering-limited regime to the absorption-limited regime near 5 μm wavelength, while for the traditional oxide-clad geometry this transition occurs near 3 μm wavelength, illustrating a substantial extension of this silicon photonics platform. One can see that throughout the entire spectral region out to 6 μm, the total intrinsic Q remains above 10^5 (loss $\leq$ 1 dB/cm), and above 10^6 (loss $\leq$ 0.1 dB/cm) out to 5 μm, which is well suited for low-loss nonlinear applications. Furthermore, the scattering-limited Q is not fundamental, and can be increased through further optimization of side-wall roughness.

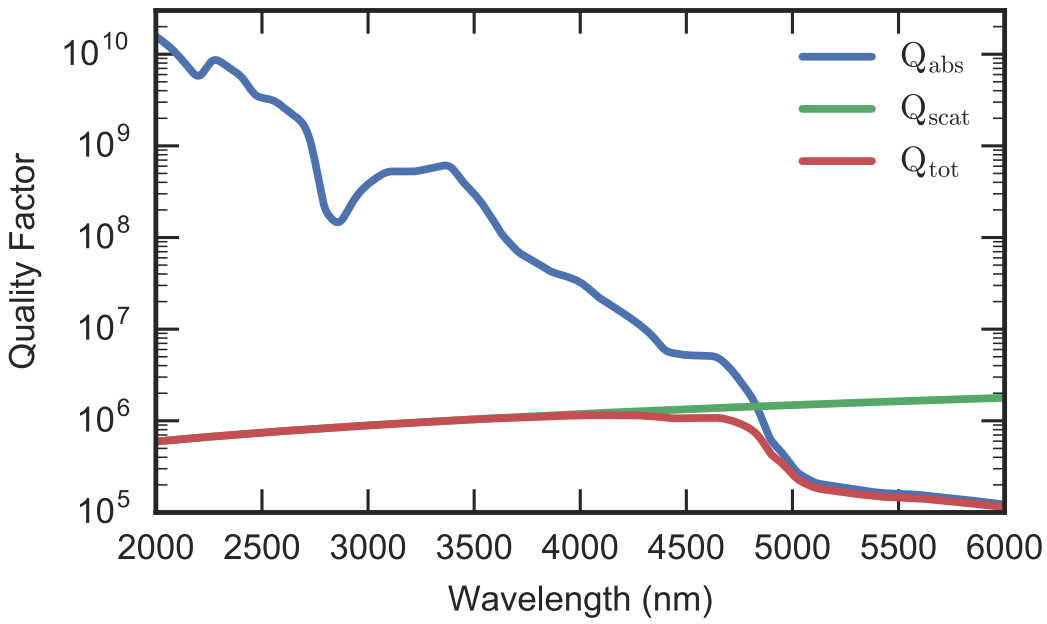

Figure 7.4: Wavelength dependence of microresonator Q (red), due to absorption loss (blue), scattering loss (green) for air-clad 2300 nm × 4000 nm waveguide. The intrinsic Q remains above 10^5 throughout the whole spectral range between 2 and 6 µm. Around 5 µm wavelength, the total intrinsic Q transitions from being scattering-limited to absorption-limited.

The waveguide geometry used here is highly confined, but maintains the ability to perform dispersion engineering necessary for nonlinear optics applications such as frequency comb generation. Parametric frequency comb generation has been extensively studied in a plethora of integrated platforms, both in the normal dispersion as well as the anomalous dispersion regime [10, 11, 20, 59, 60, 64–66, 69, 72]. Broadband frequency combs, which are advantageous for mid-IR sensing applications, require anomalous dispersion around the pump wavelength for proper phase-matching [61, 80, 156]. This is usually achieved via waveguide dispersion engineering, which requires certain waveguide confinement and dimensions [79]. If the waveguide is too small or too

large, the mode resides mostly in the cladding or the core, respectively, and exhibits mostly material dispersion properties that cannot be effectively engineered. Here we show that despite our modified geometry to minimize the waveguide loss, we retain the anomalous dispersion critical for comb generation. Figure 7.5 shows the dispersion for our air-clad waveguide geometry, which exhibits anomalous dispersion near a pump wavelength of 4 µm (2500 cm^{-1} wavenumber). This is equidistant in frequency between 3 µm (3333 cm^{-1}) and 6 µm (1667 cm^{-1}), which corresponds to an optimal pump wavelength for broadband comb generation spanning this wavelength range [95].

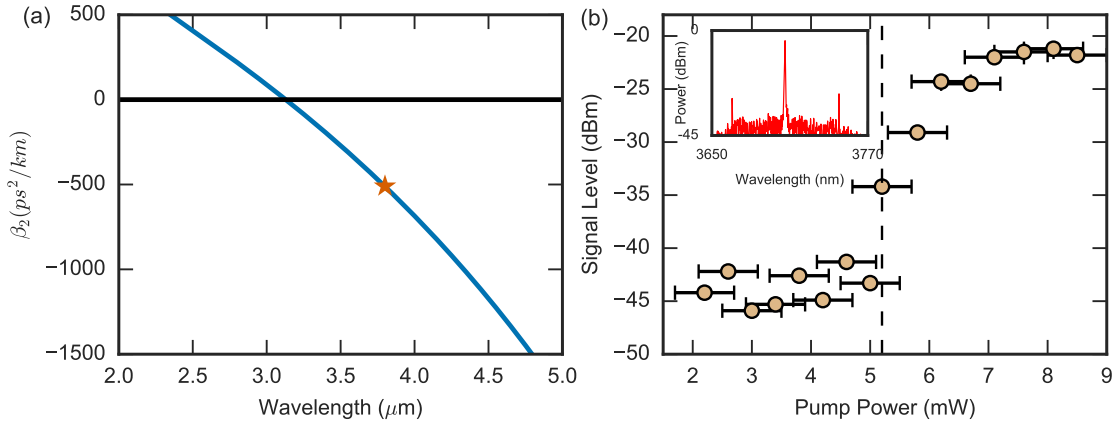

Figure 7.5: (a) Group velocity dispersion for the waveguide geometry used here (air-clad 2300 nm x 4000 nm). (b) Optical parametric oscillation (OPO) threshold measurement, indicating a 5.2 mW oscillation threshold. Inset shows the OPO sidebands generated just above threshold.

7.6 Frequency Comb Threshold Power

We demonstrate a low optical parametric oscillation threshold of 5.2 ± 0.5 mW using the proposed geometry, which is well within the operating power range

of currently available QCLs, enabling future chip-scale applications [126]. The parametric oscillation threshold is quadratically dependent on the loaded Q factor, making it a critical parameter for frequency comb generation [70, 157, 158]. In order to measure the threshold power of our microresonator, we use the same experimental setup outlined above, and use a Fourier-transform infrared spectrometer (FTIR) to monitor the mid-IR spectrum. We tune the laser wavelength into a high-Q resonance at 3.7 μm and observe parametric oscillation sidebands generated 10 free-spectral ranges (FSRs) away from the pump wavelength [Fig. 7.5 (b), inset]. In order to estimate the optical power in the bus waveguide, we assume that the measured output power level is approximately equal to the bus waveguide power inside the chip by collecting the output beam with a lens. We measure an oscillation threshold of 5.2 ± 0.5 mW [Fig. 7.5(b)]. By turning up the pump power to >50 mW, we generate a narrow band set of comb lines surrounding the pump (Fig. 7.6). The narrow comb span is due to the strong anomalous GVD value of the waveguide. The jagged envelope indicates possible mode coupling within the waveguide.

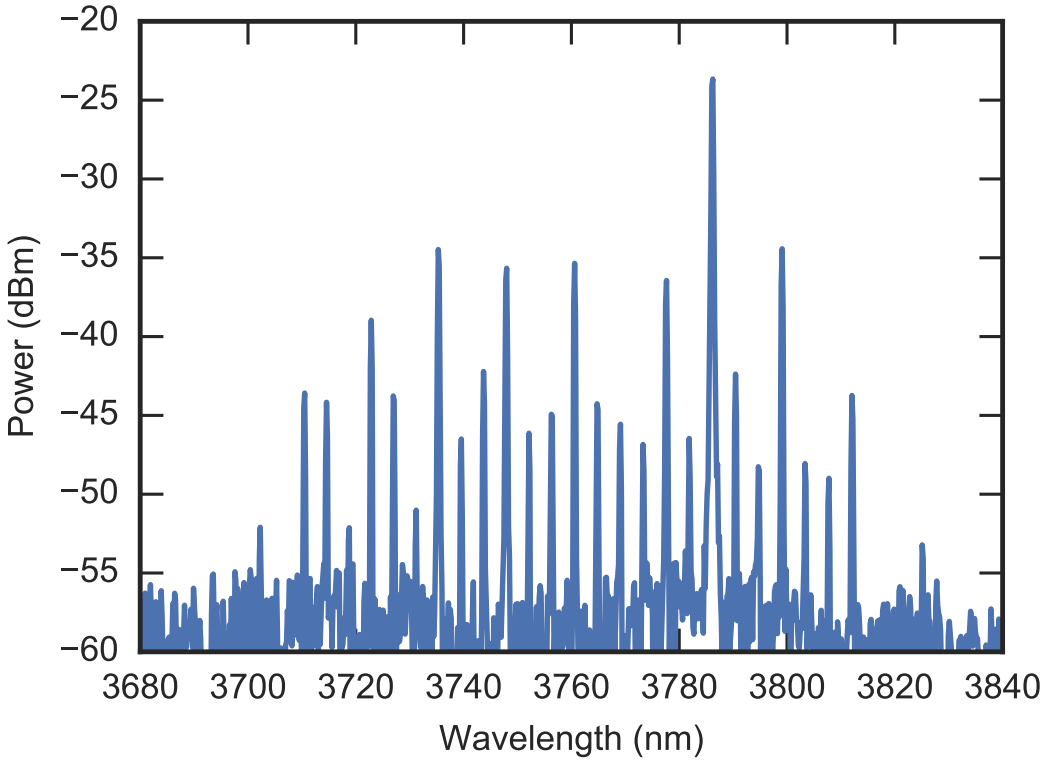

Figure 7.6: Frequency comb lines generated using air-clad geometry (2300 nm x 4000 nm). Narrow comb span is due to strong anomalous GVD value and jagged envelope indicates possible mode coupling within the waveguide.

CHAPTER 8

LOW-LOSS AIR-CLAD SUSPENDED SILICON PLATFORM FOR MID-INFRARED PHOTONICS

8.1 Introduction

In order to operate beyond 6 μm wavelength, we must turn to a fully-suspended silicon platform. Several suspended silicon devices have been demonstrated in which some or all cladding material is removed [147–149, 152]; however, minimizing high optical losses remains challenging. This is because the high refractive index contrast with air increases the effect of sidewall roughness on propagation loss compared to oxide-clad devices. For nonlinear applications, low losses and high optical quality resonators are needed. In the mid-IR, this is even more crucial than in the near-infrared since the optical structures are larger and therefore the threshold for nonlinear effects such as parametric oscillation is higher. High Q resonators also improve sensitivity for sensing applications. [1]

8.2 Device Design

To minimize the optical losses in our suspended platform we employ a low-loss air-clad suspended silicon mid-IR photonics platform using etchless processing. The etchless waveguide fabrication process has been previously used to demonstrate high confinement, high Q devices [18]. Instead of plasma etching, which introduces considerable side-wall roughness, we use thermal oxidation to de-

[1] Portions of this chapter are reproduced with permission from [159]

fine the waveguides, which leads to ultra smooth sidewalls, reducing scattering losses. When defining the waveguide we leave a thin slab surrounding the waveguide, which serves to support the suspended waveguides and resonator. To release the under-cladding, we etch holes into the slab running alongside the waveguide. A representation of the released cross-section is shown in Fig. 1(a).

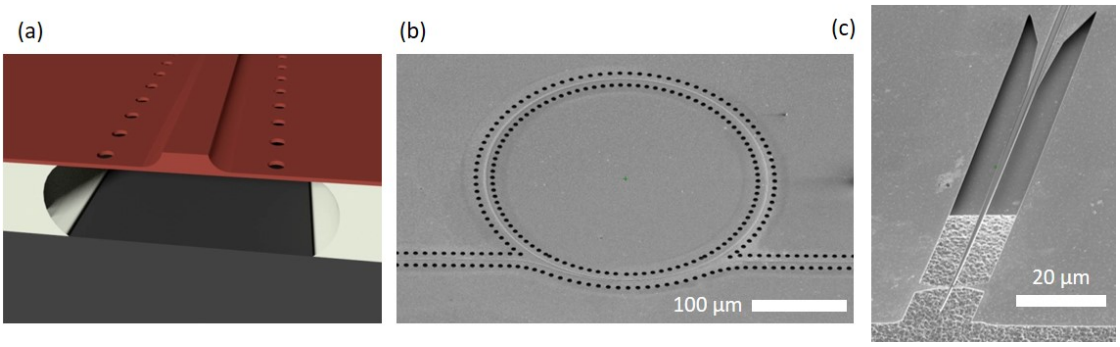

Figure 8.1: (a) Schematic of suspended etchless silicon waveguide platform with release holes. (b) Scanning electron microscope (SEM) image of suspended silicon microring resonator. (c) SEM image of suspended silicon nanotaper with support spokes. Etched substrate is visible below.

To ensure broadband input coupling, we use suspended inverse nanotapers supported by spokes designed to induce minimal losses. The challenge in this scheme is to remove the cladding via isotropic etching of multiple structures of very different dimensions that all etch at the same rate. This means the 400 nm wide nanotaper releases sooner than the microns-wide waveguide structures, but both must remain fully suspended. This suspended waveguide has strong air interaction, ideal for sensing as well as nonlinear applications requiring low loss.

We fabricate a fully air-clad high Q suspended silicon microring resonator and a suspended inverse nanotaper. The etchless process involves using ther-

mal oxidation to define the silicon waveguides after patterning a silicon nitride oxidation mask above a 500 nm thick high resistivity Float Zone SOI wafer. We perform sufficient thermal oxidation to leave a 200 nm silicon slab around 1.9 µm wide waveguides, and subsequently etch a series of holes following along either side of the waveguides for the release step. In order to define the nanotapers, we etch away the silicon slab surrounding the taper region where the taper will be suspended, as well as along all outer edges of the chip. We fabricate tapers both with and without support spokes. Finally we pattern the facet of the chip close to the taper with a small oxide gap and etch away the oxide down to the substrate. In order to efficiently couple light into the nanotaper, the substrate must not interact with the mode size at the end of the taper. Here, our largest mode size is approximately 8 m, whereas our buried oxide is only 2 m thick. Therefore, after dicing the chips, we use a xenon difluoride (XeF_2) isotropic silicon etch to laterally remove the substrate ~50 µm from the end of the taper to where the mode is well confined in the waveguide. The thermal oxidation process leaves an oxide cladding which protects the waveguides and slab from the XeF_2 etch. We then etch for 10 minutes in 49% liquid hydrofluoric acid (HF) to remove both the top thermal oxide as well as the buried oxide below the waveguide via the release holes. The silicon nitride etchless mask is also removed by the HF. Finally we dry using a standard critical point drying (CPD) process. The fully released suspended microring resonator and suspended nanotaper is shown in Fig. 1(b)-(c).

8.3 Experimental Results

Once released, we measure the suspended microring resonator to have an intrinsic Q of 83,000 at 3.79 μm wavelength. Our source is an Argos Model 2400 CW optical parametric oscillator which is tunable from 3.2 to 3.8 μm and has a 100 kHz linewidth. We use a lens to couple light into the suspended silicon nanotaper, exhibiting a coupling loss of 6-7 dB with no spokes and ~16 dB with spokes. We believe further design consideration can improve the spoke efficiency. After interacting with the ring resonator, we collect light from the chip using another lens and detect using a PbSe detector. To measure the Q, we modulate the laser wavelength using piezo modulation, and detect using a lock-in amplifier and an optical chopper in order to get a low-noise signal. We measure an intrinsic Q of 83,000 at 3.79 μm wavelength, shown in Fig. 2. This is an order of magnitude higher than previous demonstrations, representing a significant step toward enabling various low-loss mid-IR applications [148,149]. Even higher Q's can be achieved through optimized fabrication techniques, preventing issues such as sagging, coupling into the substrate, as well as complete removal of the silicon nitride oxidation mask.

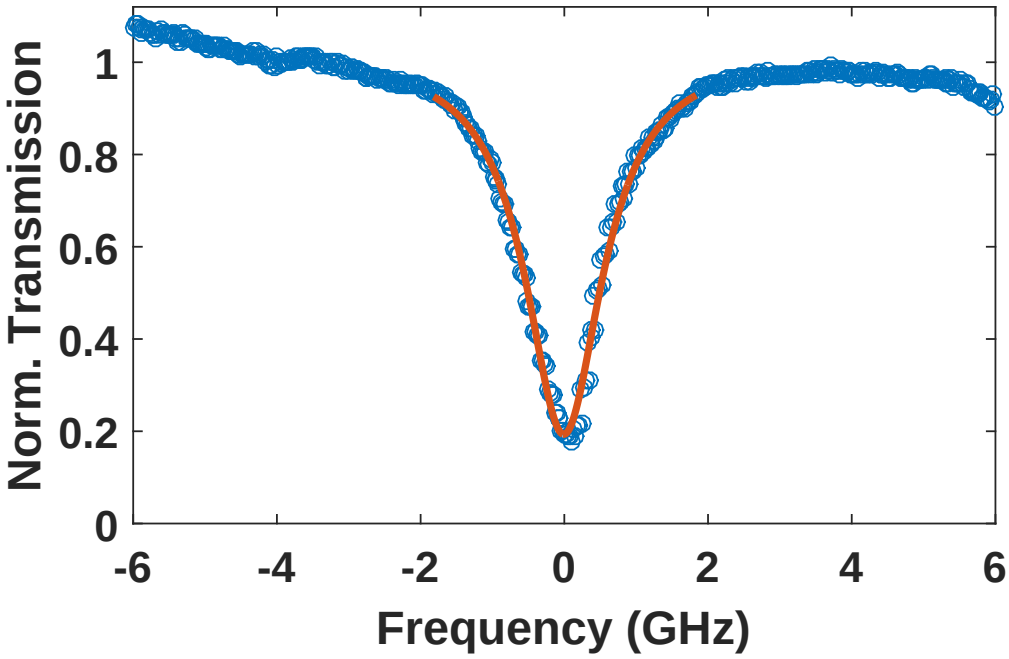

Figure 8.2: Transmission spectrum of suspended silicon microring resonator at 3.79 µm wavelength. Intrinsic Q factor measures 83,000.

CHAPTER 9

CONCLUSION

Microresonator frequency combs are an emerging technology that has the potential to influence many fields from optical clocks and astronomical calibration to spectroscopy and biomedical imaging. These combs began as a scientific curiosity but are now close to achieving real-world applications. In this work, we have taken steps toward broadening the wavelength range and expanding our electrical control over these combs in order to enable new and exciting applications. There are several avenues of future work that can continue the ongoing efforts beyond what we have accomplished in this thesis.

Despite our observations of second-order nonlinearities in silicon nitride, the community has yet to come to a consensus as to what is the true origin of these effects. Recently, a paper by Khurgin, et al. claims that stress in silicon nitride may have led silicon-nitrogen bonds to partially align, thereby giving amorphous silicon nitride some preferential dipole direction, yielding a non-zero $\chi^{(2)}$ coefficient [160]. Given this claim, it would be interesting to attempt to "pole" silicon nitride, or essentially to freeze the bonds in a preferential direction. One could imagine this being done either during deposition or a post anneal stage in which high temperatures allow the bonds to reorganize themselves in the presence of an orienting applied electric field. An enhanced $\chi^{(2)}$ from a poling process could be a game-changing discovery for integrated photonics.

Frequency combs truly in the visible range have remained somewhat elusive to date. Recently, several studies have found that strongly coupled microrings, either in a concentric or a double-layer stacked configuration, could lead to not only local modifications in dispersion but broadband dispersion shifts [161,162].

This ability is quite promising for broadband visible comb generation. However, the challenge of scattering remains, which limits high quality factors. Additionally, this strategy for dispersion engineering is particularly sensitive to geometry, which could hinder the repeatability and usefulness of such a device.

In the mid-IR, silicon itself is transparent to ~8 μm wavelength. Beyond this, however, there are several applications for sensing important molecules, including ammonia, ozone, glucose, as well as other large biochemical molecules. For these applications, germanium is a very attractive material platform, which is transparent out to 14 μm wavelength [9]. Germanium has an even higher refractive index and a higher nonlinear index than silicon, making it ideal for dispersion engineering and comb generation. There are commercially available Ge films epitaxially-grown on a silicon wafer which would be useful as a broadband waveguide, either as an airclad or suspended platform. Currently, material quality is a challenge preventing Ge films from achieving low losses. This will be an exciting broadband platform in the future.

Overall, this dissertation represents a significant step toward expanding the scope of microresonator frequency combs. Pushing toward new wavelength ranges and greater flexibility and control enables new applications previously unavailable. It is my hope that this work will lead to development of these chip-scale combs in real-world devices and systems for the environment, human health, communications, and fundamental physics.

BIBLIOGRAPHY

[1] H. A. Haus, *Waves and fields in optoelectronics*, Prentice-Hall series in solid state physical electronics (Prentice-Hall, Englewood Cliffs, NJ, 1984).

[2] P. Rabiei, W. H. Steier, C. Zhang, and L. R. Dalton, "Polymer micro-ring filters and modulators," Journal of Lightwave Technology **20**, 1968–1975 (2002).

[3] A. Yariv, Y. Xu, R. K. Lee, and A. Scherer, "Coupled-resonator optical waveguide:?a proposal and analysis," Opt. Lett., OL **24**, 711–713 (1999).

[4] F. Xia, M. Rooks, L. Sekaric, and Y. Vlasov, "Ultra-compact high order ring resonator filters using submicron silicon photonic wires for on-chip optical interconnects," Opt. Express, OE **15**, 11934–11941 (2007).

[5] N. Matsuda, T. Kato, K.-i. Harada, H. Takesue, E. Kuramochi, H. Taniyama, and M. Notomi, "Slow light enhanced optical nonlinearity in a silicon photonic crystal coupled-resonator optical waveguide," Opt. Express, OE **19**, 19861–19874 (2011).

[6] K. J. Vahala, "Optical microcavities," Nature **424**, 839–846 (2003).

[7] H. Lee, T. Chen, J. Li, K. Y. Yang, S. Jeon, O. Painter, and K. J. Vahala, "Chemically etched ultrahigh-Q wedge-resonator on a silicon chip," Nat Photon **6**, 369–373 (2012).

[8] D. K. Armani, T. J. Kippenberg, S. M. Spillane, and K. J. Vahala, "Ultra-high-Q toroid microcavity on a chip," Nature **421**, 925–928 (2003).

[9] R. Soref, "Mid-infrared photonics in silicon and germanium," Nat Photon **4**, 495–497 (2010).

[10] B. J. M. Hausmann, I. Bulu, V. Venkataraman, P. Deotare, and M. Lonar, "Diamond nonlinear photonics," Nat Photon **8**, 369–374 (2014).

[11] H. Jung, C. Xiong, K. Y. Fong, X. Zhang, and H. X. Tang, "Optical frequency comb generation from aluminum nitride microring resonator," Optics Letters **38**, 2810 (2013).

[12] J. Cardenas, M. Zhang, C. T. Phare, S. Y. Shah, C. B. Poitras, B. Guha, and M. Lipson, "High Q SiC microresonators," Opt. Express, OE **21**, 16882–16887 (2013).

[13] C. Wang, M. Zhang, B. Stern, M. Lipson, and M. Loncar, "Nanophotonic Lithium Niobate Electro-optic Modulators," arXiv:1701.06470 [cond-mat, physics:physics] (2017). ArXiv: 1701.06470.

[14] C. T. Phare, Y.-H. Daniel Lee, J. Cardenas, and M. Lipson, "Graphene electro-optic modulator with 30 GHz bandwidth," Nat Photon **9**, 511–514 (2015).

[15] X. Liu, T. Galfsky, Z. Sun, F. Xia, E.-c. Lin, Y.-H. Lee, S. Kna-Cohen, and V. M. Menon, "Strong lightmatter coupling in two-dimensional atomic crystals," Nat Photon **9**, 30–34 (2015).

[16] G. Cassabois, P. Valvin, and B. Gil, "Hexagonal boron nitride is an indirect bandgap semiconductor," Nat Photon **10**, 262–266 (2016).

[17] L.-W. Luo, G. S. Wiederhecker, J. Cardenas, C. Poitras, and M. Lipson, "High quality factor etchless silicon photonic ring resonators," Opt. Express, OE **19**, 6284–6289 (2011).

[18] A. Griffith, J. Cardenas, C. B. Poitras, and M. Lipson, "High quality factor and high confinement silicon resonators using etchless process," Opt. Express, OE **20**, 21341–21345 (2012).

[19] R. W. Boyd, *Nonlinear Optics, Third Edition* (Academic Press, 2008), 3rd ed.

[20] P. DelHaye, A. Schliesser, O. Arcizet, T. Wilken, R. Holzwarth, and T. J. Kippenberg, "Optical frequency comb generation from a monolithic microresonator," Nature **450**, 1214–1217 (2007).

[21] J. L. O'Brien, A. Furusawa, and J. Vukovi, "Photonic quantum technologies," Nat Photon **3**, 687–695 (2009).

[22] A. F. Fercher, W. Drexler, C. K. Hitzenberger, and T. Lasser, "Optical coherence tomography - principles and applications," Rep. Prog. Phys. **66**, 239 (2003).

[23] V. M. N. Passaro, C. d. Tullio, B. Troia, M. L. Notte, G. Giannoccaro, and

F. D. Leonardis, "Recent Advances in Integrated Photonic Sensors," Sensors **12**, 15558–15598 (2012).

[24] J. Faist, F. Capasso, D. L. Sivco, C. Sirtori, A. L. Hutchinson, and A. Y. Cho, "Quantum Cascade Laser," Science **264**, 553–556 (1994).

[25] C. Lecaplain, C. Javerzac-Galy, M. L. Gorodetsky, and T. J. Kippenberg, "Mid-Infrared ultra-high-Q resonators based on fluoride crystalline materials," arXiv:1603.07305 [physics] (2016). ArXiv: 1603.07305.

[26] A. A. Savchenkov, V. S. Ilchenko, F. D. Teodoro, P. M. Belden, W. T. Lotshaw, A. B. Matsko, and L. Maleki, "Generation of Kerr combs centered at 4.5 um in crystalline microresonators pumped with quantum-cascade lasers," Opt. Lett., OL **40**, 3468–3471 (2015).

[27] A. Spott, Y. Liu, T. Baehr-Jones, R. Ilic, and M. Hochberg, "Silicon waveguides and ring resonators at 5.5 um," Applied Physics Letters **97**, 213501 (2010).

[28] T. Baehr-Jones, A. Spott, R. Ilic, A. Spott, B. Penkov, W. Asher, and M. Hochberg, "Silicon-on-sapphire integrated waveguides for the mid-infrared," Optics Express **18**, 12127 (2010).

[29] F. Li, S. D. Jackson, C. Grillet, E. Magi, D. Hudson, S. J. Madden, Y. Moghe, C. OBrien, A. Read, S. G. Duvall, P. Atanackovic, B. J. Eggleton, and D. J. Moss, "Low propagation loss silicon-on-sapphire waveguides for the mid-infrared," Optics Express **19**, 15212 (2011).

[30] C. Y. Wong, Z. Cheng, X. Chen, K. Xu, C. K. Y. Fung, Y. M. Chen, and H. K. Tsang, "Characterization of Mid-Infrared Silicon-on-Sapphire Microring Resonators With Thermal Tuning," IEEE Photonics Journal **4**, 1095–1102 (2012).

[31] R. Shankar, I. Bulu, and M. Lonar, "Integrated high-quality factor silicon-on-sapphire ring resonators for the mid-infrared," Applied Physics Letters **102**, 051108 (2013).

[32] N. Singh, D. D. Hudson, Y. Yu, C. Grillet, S. D. Jackson, A. Casas-Bedoya, A. Read, P. Atanackovic, S. G. Duvall, S. Palomba, B. Luther-Davies, S. Madden, D. J. Moss, and B. J. Eggleton, "Midinfrared supercontinuum generation from 2 to 6 um in a silicon nanowire," Optica **2**, 797 (2015).

[33] S. Kalchmair, R. Shankar, S. Kita, C. Mittag, I. Bulu, and M. Loncar, "Cascaded Four-Wave Mixing in Silicon-on-Sapphire Microresonators at lambda=4.5 um," in "CLEO: 2015 (2015), paper STu2I.3," (Optical Society of America, 2015), p. STu2I.3.

[34] Y. Zou, S. Chakravarty, and R. T. Chen, "Mid-infrared silicon-on-sapphire waveguide coupled photonic crystal microcavities," Applied Physics Letters **107**, 081109 (2015).

[35] Y. Huang, Q. Zhao, S. K. Kalyoncu, R. Torun, and O. Boyraz, "Silicon-on-sapphire mid-IR wavefront engineering by using subwavelength grating metasurfaces," J. Opt. Soc. Am. B, JOSAB **33**, 189–194 (2016).

[36] H. Lin, L. Li, Y. Zou, S. Novak, K. Richardson, and J. Hu, "High-Q mid-infrared chalcogenide glass resonators for chemical sensing," arXiv:1612.04322 [cond-mat, physics:physics] (2016). ArXiv: 1612.04322.

[37] B. J. Eggleton, B. Luther-Davies, and K. Richardson, "Chalcogenide photonics," Nat Photon **5**, 141–148 (2011).

[38] N. Carlie, J. D. Musgraves, B. Zdyrko, I. Luzinov, J. Hu, V. Singh, A. Agarwal, L. C. Kimerling, A. Canciamilla, F. Morichetti, A. Melloni, and K. Richardson, "Integrated chalcogenide waveguide resonators for mid-IR sensing: leveraging material properties to meet fabrication challenges," Optics Express **18**, 26728 (2010).

[39] P. Ma, D.-Y. Choi, Y. Yu, X. Gai, Z. Yang, S. Debbarma, S. Madden, and B. Luther-Davies, "Low-loss chalcogenide waveguides for chemical sensing in the mid-infrared," Opt. Express, OE **21**, 29927–29937 (2013).

[40] Y. Zha, P. T. Lin, L. Kimerling, A. Agarwal, and C. B. Arnold, "Inverted-Rib Chalcogenide Waveguides by Solution Process," ACS Photonics **1**, 153–157 (2014).

[41] A. Gondarenko, J. S. Levy, and M. Lipson, "High confinement micron-scale silicon nitride high Q ring resonator," Opt. Express, OE **17**, 11366–11370 (2009).

[42] K. Luke, A. Dutt, C. B. Poitras, and M. Lipson, "Overcoming Si_3N_4 film stress limitations for high quality factor ring resonators," Opt. Express, OE **21**, 22829–22833 (2013).

[43] J. Cardenas, C. B. Poitras, K. Luke, L. W. Luo, P. A. Morton, and M. Lipson, "High Coupling Efficiency Etched Facet Tapers in Silicon Waveguides," IEEE Photonics Technology Letters **26**, 2380–2382 (2014).

[44] B. Desiatov, I. Goykhman, and U. Levy, "Demonstration of submicron square-like silicon waveguide using optimized LOCOS process," Opt. Express, OE **18**, 18592–18597 (2010).

[45] P. Drude, "Zur Elektronentheorie der Metalle," Ann. Phys. **306**, 566–613 (1900).

[46] Y. Liu, Y. Xuan, X. Xue, P.-H. Wang, S. Chen, A. J. Metcalf, J. Wang, D. E. Leaird, M. Qi, and A. M. Weiner, "Investigation of mode coupling in normal-dispersion silicon nitride microresonators for Kerr frequency comb generation," Optica, OPTICA **1**, 137–144 (2014).

[47] X. Xue, Y. Xuan, P.-H. Wang, Y. Liu, D. E. Leaird, M. Qi, and A. M. Weiner, "Normal-dispersion microcombs enabled by controllable mode interactions," Laser & Photonics Reviews **9**, L23–L28 (2015).

[48] T. Udem, R. Holzwarth, and T. W. Hnsch, "Optical frequency metrology," Nature **416**, 233–237 (2002).

[49] T. Steinmetz, T. Wilken, C. Araujo-Hauck, R. Holzwarth, T. W. Hnsch, L. Pasquini, A. Manescau, S. D'Odorico, M. T. Murphy, T. Kentischer, W. Schmidt, and T. Udem, "Laser Frequency Combs for Astronomical Observations," Science **321**, 1335–1337 (2008).

[50] S. A. Diddams, T. Udem, J. C. Bergquist, E. A. Curtis, R. E. Drullinger, L. Hollberg, W. M. Itano, W. D. Lee, C. W. Oates, K. R. Vogel, and D. J. Wineland, "An Optical Clock Based on a Single Trapped 199hg+ Ion," Science **293**, 825–828 (2001).

[51] I. Coddington, N. Newbury, and W. Swann, "Dual-comb spectroscopy," Optica, OPTICA **3**, 414–426 (2016).

[52] J. Pfeifle, V. Brasch, M. Lauermann, Y. Yu, D. Wegner, T. Herr, K. Hartinger, P. Schindler, J. Li, D. Hillerkuss, R. Schmogrow, C. Weimann, R. Holzwarth, W. Freude, J. Leuthold, T. J. Kippenberg, and C. Koos, "Coherent terabit communications with microresonator Kerr frequency combs," Nat Photon **8**, 375–380 (2014).

[53] T. J. Kippenberg, R. Holzwarth, and S. A. Diddams, "Microresonator-Based Optical Frequency Combs," Science **332**, 555–559 (2011).

[54] S. A. Diddams, D. J. Jones, J. Ye, S. T. Cundiff, J. L. Hall, J. K. Ranka, R. S. Windeler, R. Holzwarth, T. Udem, and T. W. Hnsch, "Direct Link between Microwave and Optical Frequencies with a 300 THz Femtosecond Laser Comb," Physical Review Letters **84**, 5102–5105 (2000).

[55] L. A. Lugiato and R. Lefever, "Spatial Dissipative Structures in Passive Optical Systems," Phys. Rev. Lett. **58**, 2209 (1987).

[56] S. Coen, H. G. Randle, T. Sylvestre, and M. Erkintalo, "Modeling of octave-spanning Kerr frequency combs using a generalized mean-field LugiatoLefever model," Opt. Lett., OL **38**, 37–39 (2013).

[57] M. R. E. Lamont, Y. Okawachi, and A. L. Gaeta, "Route to stabilized ultrabroadband microresonator-based frequency combs," Opt. Lett., OL **38**, 3478–3481 (2013).

[58] T. Carmon, L. Yang, and K. J. Vahala, "Dynamical thermal behavior and thermal self-stability of microcavities," Opt. Express, OE **12**, 4742–4750 (2004).

[59] A. G. Griffith, R. K. W. Lau, J. Cardenas, Y. Okawachi, A. Mohanty, R. Fain, Y. H. D. Lee, M. Yu, C. T. Phare, C. B. Poitras, A. L. Gaeta, and M. Lipson, "Silicon-chip mid-infrared frequency comb generation," Nat Commun **6**, 6299 (2015).

[60] W. Liang, A. A. Savchenkov, A. B. Matsko, V. S. Ilchenko, D. Seidel, and L. Maleki, "Generation of near-infrared frequency combs from a MgF_2 whispering gallery mode resonator," Optics Letters **36**, 2290 (2011).

[61] Y. Okawachi, K. Saha, J. S. Levy, Y. H. Wen, M. Lipson, and A. L. Gaeta, "Octave-spanning frequency comb generation in a silicon nitride chip," Optics Letters **36**, 3398 (2011).

[62] S. B. Papp and S. A. Diddams, "Spectral and temporal characterization of a fused-quartz-microresonator optical frequency comb," Phys. Rev. A **84**, 053833 (2011).

[63] K. Saha, Y. Okawachi, J. S. Levy, R. K. W. Lau, K. Luke, M. A. Foster, M. Lipson, and A. L. Gaeta, "Broadband parametric frequency comb

generation with a 1-m pump source," Opt. Express, OE **20**, 26935–26941 (2012).

[64] J. S. Levy, A. Gondarenko, M. A. Foster, A. C. Turner-Foster, A. L. Gaeta, and M. Lipson, "CMOS-compatible multiple-wavelength oscillator for on-chip optical interconnects," Nat Photon **4**, 37–40 (2010).

[65] X. Xue, Y. Xuan, Y. Liu, P.-H. Wang, S. Chen, J. Wang, D. E. Leaird, M. Qi, and A. M. Weiner, "Mode-locked dark pulse Kerr combs in normal-dispersion microresonators," Nat Photon **9**, 594–600 (2015).

[66] I. S. Grudinin, N. Yu, and L. Maleki, "Generation of optical frequency combs with a CaF_2 resonator," Optics Letters **34**, 878 (2009).

[67] P.-H. Wang, F. Ferdous, H. Miao, J. Wang, D. E. Leaird, K. Srinivasan, L. Chen, V. Aksyuk, and A. M. Weiner, "Observation of correlation between route to formation, coherence, noise, and communication performance of Kerr combs," Opt. Express, OE **20**, 29284–29295 (2012).

[68] S. B. Papp, K. Beha, P. DelHaye, F. Quinlan, H. Lee, K. J. Vahala, and S. A. Diddams, "Microresonator frequency comb optical clock," Optica, OPTICA **1**, 10–14 (2014).

[69] C. Y. Wang, T. Herr, P. DelHaye, A. Schliesser, J. Hofer, R. Holzwarth, T. W. Hnsch, N. Picqu, and T. J. Kippenberg, "Mid-infrared optical frequency combs at 2.5 um based on crystalline microresonators," Nat Commun **4**, 1345 (2013).

[70] J. Li, H. Lee, T. Chen, and K. J. Vahala, "Low-Pump-Power, Low-Phase-Noise, and Microwave to Millimeter-Wave Repetition Rate Operation in Microcombs," Phys. Rev. Lett. **109**, 233901 (2012).

[71] S.-W. Huang, H. Zhou, J. Yang, J. McMillan, A. Matsko, M. Yu, D.-L. Kwong, L. Maleki, and C. Wong, "Mode-Locked Ultrashort Pulse Generation from On-Chip Normal Dispersion Microresonators," Phys. Rev. Lett. **114**, 053901 (2015).

[72] M. Pu, L. Ottaviano, E. Semenova, and K. Yvind, "Efficient frequency comb generation in AlGaAs-on-insulator," Optica **3**, 823 (2016).

[73] L. Wang, L. Chang, N. Volet, M. H. P. Pfeiffer, M. Zervas, H. Guo, T. J. Kippenberg, and J. E. Bowers, "Frequency comb generation in the green using

silicon nitride microresonators," Laser & Photonics Reviews **10**, 631–638 (2016).

[74] Y. Millerioux, D. Touahri, L. Hilico, A. Clairon, R. Felder, F. Biraben, and B. de Beauvoir, "Towards an accurate frequency standard at 778 nm using a laser diode stabilized on a hyperfine component of the Doppler-free two-photon transitions in rubidium," Optics Communications **108**, 91–96 (1994).

[75] J. Vanier and C. Mandache, "The Passive Optically Pumped Rb Frequency Standard: the Laser Approach," in "2007 IEEE International Frequency Control Symposium Joint with the 21st European Frequency and Time Forum," (2007), pp. 1346–1351.

[76] J. Vanier, "Atomic clocks based on coherent population trapping: a review," Appl. Phys. B **81**, 421–442 (2005).

[77] E. A. Swanson, D. Huang, C. P. Lin, C. A. Puliafito, M. R. Hee, and J. G. Fujimoto, "High-speed optical coherence domain reflectometry," Opt. Lett., OL **17**, 151–153 (1992).

[78] S. Miller, K. Luke, Y. Okawachi, J. Cardenas, A. L. Gaeta, and M. Lipson, "On-chip frequency comb generation at visible wavelengths via simultaneous second- and third-order optical nonlinearities," Opt. Express, OE **22**, 26517–26525 (2014).

[79] A. C. Turner, C. Manolatou, B. S. Schmidt, M. Lipson, M. A. Foster, J. E. Sharping, and A. L. Gaeta, "Tailored anomalous group-velocity dispersion in silicon channel waveguides," Optics Express **14**, 4357 (2006).

[80] P. DelHaye, T. Herr, E. Gavartin, M. L. Gorodetsky, R. Holzwarth, and T. J. Kippenberg, "Octave Spanning Tunable Frequency Comb from a Microresonator," Phys. Rev. Lett. **107**, 063901 (2011).

[81] Y. Okawachi, M. R. E. Lamont, K. Luke, D. O. Carvalho, M. Yu, M. Lipson, and A. L. Gaeta, "Bandwidth shaping of microresonator-based frequency combs via dispersion engineering," Opt. Lett., OL **39**, 3535–3538 (2014).

[82] K. Luke, Y. Okawachi, D. O. Carvalho, M. R. Lamont, A. L. Gaeta, and M. Lipson, "Broadband Microresonator-Based Parametric Frequency Comb near Visible Wavelengths," in "CLEO: 2014 (2014), paper FW1D.3," (Optical Society of America, 2014), p. FW1D.3.

[83] A. A. Savchenkov, A. B. Matsko, W. Liang, V. S. Ilchenko, D. Seidel, and L. Maleki, "Kerr combs with selectable central frequency," Nat Photon **5**, 293–296 (2011).

[84] M. Cazzanelli, F. Bianco, E. Borga, G. Pucker, M. Ghulinyan, E. Degoli, E. Luppi, V. Vniard, S. Ossicini, D. Modotto, S. Wabnitz, R. Pierobon, and L. Pavesi, "Second-harmonic generation in silicon waveguides strained by silicon nitride," Nat Mater **11**, 148–154 (2012).

[85] T. Ning, H. Pietarinen, O. Hyvrinen, J. Simonen, G. Genty, and M. Kauranen, "Strong second-harmonic generation in silicon nitride films," Applied Physics Letters (2012).

[86] J. S. Levy, M. A. Foster, A. L. Gaeta, and M. Lipson, "Harmonic generation in silicon nitride ring resonators," Opt. Express, OE **19**, 11415–11421 (2011).

[87] D. F. Logan, A. B. A. Dow, D. Stepanov, P. Abolghasem, N. P. Kherani, and A. S. Helmy, "Harnessing second-order optical nonlinearities at interfaces in multilayer silicon-oxy-nitride waveguides," Applied Physics Letters (2013).

[88] L. C. Andreani, P. Andrich, M. Galli, D. Gerace, G. Guizzetti, R. L. Savio, S. L. Portalupi, L. O'Faolain, C. Reardon, K. Welna, and T. F. Krauss, "Nonlinear optics in Silicon photonic crystal cavities," in "2011 13th International Conference on Transparent Optical Networks," (2011), pp. 1–4.

[89] T. Ning, H. Pietarinen, O. Hyvrinen, R. Kumar, T. Kaplas, M. Kauranen, and G. Genty, "Efficient second-harmonic generation in silicon nitride resonant waveguide gratings," Opt. Lett., OL **37**, 4269–4271 (2012).

[90] E. F. Pecora, A. Capretti, G. Miano, and L. D. Negro, "Generation of second harmonic radiation from sub-stoichiometric silicon nitride thin films," Applied Physics Letters (2013).

[91] A. Kitao, K. Imakita, I. Kawamura, and M. Fujii, "An investigation into second harmonic generation by Si-rich SiN x thin films deposited by RF sputtering over a wide range of Si concentrations," J. Phys. D: Appl. Phys. **47**, 215101 (2014).

[92] B. Chmielak, C. Matheisen, C. Ripperda, J. Bolten, T. Wahlbrink, M. Waldow, and H. Kurz, "Investigation of local strain distribution and linear

electro-optic effect in strained silicon waveguides," Opt. Express, OE **21**, 25324–25332 (2013).

[93] D. J. Moss, R. Morandotti, A. L. Gaeta, and M. Lipson, "New CMOS-compatible platforms based on silicon nitride and Hydex for nonlinear optics," Nat Photon **7**, 597–607 (2013).

[94] R. W. Boyd, *Nonlinear optics* (Academic Press, Amsterdam ; Boston, 2008), 3rd ed.

[95] T. Herr, V. Brasch, J. D. Jost, C. Y. Wang, N. M. Kondratiev, M. L. Gorodetsky, and T. J. Kippenberg, "Temporal solitons in optical microresonators," Nat Photon **8**, 145–152 (2014).

[96] P. S. Londero, J. Levy, A. Slepkov, A. Bhagwat, K. Saha, V. Venkataraman, M. Lipson, and A. L. Gaeta, "Chip-Based Optical Interactions with Rubidium Vapor," in "Conference on Lasers and Electro-Optics 2010 (2010), paper QFE4," (Optical Society of America, 2010), p. QFE4.

[97] L. Stern, B. Desiatov, I. Goykhman, and U. Levy, "Nanoscale lightmatter interactions in atomic cladding waveguides," Nature Communications **4**, 1548 (2013).

[98] C. Xiong, W. H. P. Pernice, and H. X. Tang, "Low-Loss, Silicon Integrated, Aluminum Nitride Photonic Circuits and Their Use for Electro-Optic Signal Processing," Nano Lett. **12**, 3562–3568 (2012).

[99] S. Miller, Y. H. D. Lee, J. Cardenas, A. L. Gaeta, and M. Lipson, "Electro-optic effect in silicon nitride," in "CLEO: 2015 (2015), paper SF1G.4," (Optical Society of America, 2015), p. SF1G.4.

[100] Y. R. Shen, "Surface properties probed by second-harmonic and sum-frequency generation," Nature **337**, 519–525 (1989).

[101] C. Bao, L. Zhang, A. Matsko, Y. Yan, Z. Zhao, G. Xie, A. M. Agarwal, L. C. Kimerling, J. Michel, L. Maleki, and A. E. Willner, "Nonlinear conversion efficiency in Kerr frequency comb generation," Opt. Lett., OL **39**, 6126–6129 (2014).

[102] S. A. Miller, Y. Okawachi, S. Ramelow, K. Luke, A. Dutt, A. Farsi, A. L. Gaeta, and M. Lipson, "Tunable frequency combs based on dual microring resonators," Opt. Express, OE **23**, 21527–21540 (2015).

[103] X. Xue, Y. Xuan, P.-H. Wang, J. Wang, D. E. Leaird, M. Qi, and A. M. Weiner, "Tunable Frequency Comb Generation from a Microring with a Thermal Heater," in "CLEO: 2014 (2014), paper SF1I.8," (Optical Society of America, 2014), p. SF1I.8.

[104] L. Zhou and A. W. Poon, "Electrically reconfigurable silicon microring resonator-based filter with waveguide-coupled feedback," Opt. Express, OE **15**, 9194–9204 (2007).

[105] M. A. Popovic, T. Barwicz, F. Gan, M. S. Dahlem, C. W. Holzwarth, P. T. Rakich, H. I. Smith, E. P. Ippen, and F. X. Krtner, "Transparent Wavelength Switching of Resonant Filters," in "Conference on Lasers and Electro-Optics/Quantum Electronics and Laser Science Conference and Photonic Applications Systems Technologies (2007), paper CPDA2," (Optical Society of America, 2007), p. CPDA2.

[106] L. Chen, N. Sherwood-Droz, and M. Lipson, "Compact bandwidth-tunable microring resonators," Opt. Lett., OL **32**, 3361–3363 (2007).

[107] C. M. Gentry, X. Zeng, and M. A. Popovi, "Tunable coupled-mode dispersion compensation and its application to on-chip resonant four-wave mixing," Opt. Lett., OL **39**, 5689–5692 (2014).

[108] R. Boeck, N. A. F. Jaeger, N. Rouger, and L. Chrostowski, "Series-coupled silicon racetrack resonators and the Vernier effect: theory and measurement," Opt. Express, OE **18**, 25151–25157 (2010).

[109] W. S. Fegadolli, G. Vargas, X. Wang, F. Valini, L. A. M. Barea, J. E. B. Oliveira, N. Frateschi, A. Scherer, V. R. Almeida, and R. R. Panepucci, "Reconfigurable silicon thermo-optical ring resonator switch based on Vernier effect control," Opt. Express, OE **20**, 14722–14733 (2012).

[110] G. Griffel, "Vernier effect in asymmetrical ring resonator arrays," IEEE Photonics Technology Letters **12**, 1642–1644 (2000).

[111] T. Herr, K. Hartinger, J. Riemensberger, C. Y. Wang, E. Gavartin, R. Holzwarth, M. L. Gorodetsky, and T. J. Kippenberg, "Universal formation dynamics and noise of Kerr-frequency combs in microresonators," Nat Photon **6**, 480–487 (2012).

[112] W. W. Lui, T. Hirono, K. Yokoyama, and W.-P. Huang, "Polarization rotation in semiconductor bending waveguides: a coupled-mode theory formulation," Journal of Lightwave Technology **16**, 929–936 (1998).

[113] N. Somasiri and B. M. A. Rahman, "Polarization crosstalk in high index contrast planar silica waveguides with slanted sidewalls," Journal of Lightwave Technology **21**, 54–60 (2003).

[114] F. Morichetti, A. Melloni, and M. Martinelli, "Modelling of Polarization Rotation in Bent Waveguides," in "2006 International Conference on Transparent Optical Networks," , vol. 4 (2006), vol. 4, pp. 261–261.

[115] T. Herr, V. Brasch, J. Jost, I. Mirgorodskiy, G. Lihachev, M. Gorodetsky, and T. Kippenberg, "Mode Spectrum and Temporal Soliton Formation in Optical Microresonators," Phys. Rev. Lett. **113**, 123901 (2014).

[116] I. S. Grudinin, L. Baumgartel, and N. Yu, "Impact of cavity spectrum on span in microresonator frequency combs," Opt. Express, OE **21**, 26929–26935 (2013).

[117] D. T. Spencer, J. F. Bauters, M. J. R. Heck, and J. E. Bowers, "Integrated waveguide coupled Si_3N_4 resonators in the ultrahigh-Q regime," Optica, OPTICA **1**, 153–157 (2014).

[118] V. Brasch, M. Geiselmann, T. Herr, G. Lihachev, M. H. Pfeiffer, M. L. Gorodetsky, and T. Kippenberg, "Photonic Chip Based Optical Frequency Comb Using Soliton Induced Cherenkov Radiation," in "Nonlinear Optics (2015), paper NM1A.5," (Optical Society of America, 2015), p. NM1A.5.

[119] S. Ramelow, A. Farsi, S. Clemmen, J. S. Levy, A. R. Johnson, Y. Okawachi, M. R. E. Lamont, M. Lipson, and A. L. Gaeta, "Strong polarization mode coupling in microresonators," Opt. Lett., OL **39**, 5134–5137 (2014).

[120] J. S. Levy, K. Saha, Y. Okawachi, M. A. Foster, A. L. Gaeta, and M. Lipson, "High-Performance Silicon-Nitride-Based Multiple-Wavelength Source," IEEE Photonics Technology Letters **24**, 1375–1377 (2012).

[121] D. A. B. Miller, "Device Requirements for Optical Interconnects to Silicon Chips," Proceedings of the IEEE **97**, 1166–1185 (2009).

[122] M. J. R. Heck and J. E. Bowers, "Energy Efficient and Energy Proportional Optical Interconnects for Multi-Core Processors: Driving the Need for On-Chip Sources," IEEE Journal of Selected Topics in Quantum Electronics **20**, 332–343 (2014).

[123] K. Saha, Y. Okawachi, B. Shim, J. S. Levy, R. Salem, A. R. Johnson, M. A. Foster, M. R. E. Lamont, M. Lipson, and A. L. Gaeta, "Modelocking and femtosecond pulse generation in chip-based frequency combs," Opt. Express, OE **21**, 1335–1343 (2013).

[124] F. K. Tittel, D. Richter, and A. Fried, "Mid-Infrared Laser Applications in Spectroscopy," in "Solid-State Mid-Infrared Laser Sources," , D. I. T. Sorokina and D. K. L. Vodopyanov, eds. (Springer Berlin Heidelberg, 2003), no. 89 in Topics in Applied Physics, pp. 458–529. DOI: 10.1007/3-540-36491-9_11.

[125] A. Hugi, G. Villares, S. Blaser, H. C. Liu, and J. Faist, "Mid-infrared frequency comb based on a quantum cascade laser," Nature **492**, 229–233 (2012).

[126] A. Spott, J. Peters, M. L. Davenport, E. J. Stanton, C. D. Merritt, W. W. Bewley, I. Vurgaftman, C. S. Kim, J. R. Meyer, J. Kirch, L. J. Mawst, D. Botez, and J. E. Bowers, "Quantum cascade laser on silicon," Optica, OPTICA **3**, 545–551 (2016).

[127] M. Streshinsky, R. Ding, Y. Liu, A. Novack, C. Galland, A. E.-J. Lim, P. G.-Q. Lo, T. Baehr-Jones, and M. Hochberg, "The Road to Affordable, Large-Scale Silicon Photonics," Optics & Photonics News, OPN **24**, 32–39 (2013).

[128] A. E. J. Lim, J. Song, Q. Fang, C. Li, X. Tu, N. Duan, K. K. Chen, R. P. C. Tern, and T. Y. Liow, "Review of Silicon Photonics Foundry Efforts," IEEE Journal of Selected Topics in Quantum Electronics **20**, 405–416 (2014).

[129] R. A. Soref, S. J. Emelett, and W. R. Buchwald, "Silicon waveguided components for the long-wave infrared region," J. Opt. A: Pure Appl. Opt. **8**, 840 (2006).

[130] M. M. Miloevi, P. S. Matavulj, P. Y. Yang, A. Bagolini, and G. Z. Mashanovich, "Rib waveguides for mid-infrared silicon photonics," Journal of the Optical Society of America B **26**, 1760 (2009).

[131] R. Kitamura, L. Pilon, and M. Jonasz, "Optical constants of silica glass from extreme ultraviolet to far infrared at near room temperature," Appl. Opt., AO **46**, 8118–8133 (2007).

[132] G. Z. Mashanovich, M. M. Miloevi, M. Nedeljkovic, N. Owens, B. Xiong, E. J. Teo, and Y. Hu, "Low loss silicon waveguides for the mid-infrared," Optics Express **19**, 7112 (2011).

[133] C. Reimer, M. Nedeljkovic, D. J. M. Stothard, M. O. S. Esnault, C. Reardon, L. OFaolain, M. Dunn, G. Z. Mashanovich, and T. F. Krauss, "Mid-infrared photonic crystal waveguides in silicon," Optics Express **20**, 29361 (2012).

[134] M. M. Miloevi, M. Nedeljkovic, T. M. B. Masaud, E. Jaberansary, H. M. H. Chong, N. G. Emerson, G. T. Reed, and G. Z. Mashanovich, "Silicon waveguides and devices for the mid-infrared," Applied Physics Letters **101**, 121105 (2012).

[135] M. Nedeljkovic, A. Z. Khokhar, Y. Hu, X. Chen, J. S. Penades, S. Stankovic, H. M. H. Chong, D. J. Thomson, F. Y. Gardes, G. T. Reed, and G. Z. Mashanovich, "Silicon photonic devices and platforms for the mid-infrared," Opt. Mater. Express, OME **3**, 1205–1214 (2013).

[136] S. Khan, J. Chiles, J. Ma, and S. Fathpour, "Silicon-on-nitride waveguides for mid- and near-infrared integrated photonics," Applied Physics Letters **102**, 121104 (2013).

[137] G. Roelkens, U. Dave, A. Gassenq, N. Hattasan, C. Hu, B. Kuyken, F. Leo, A. Malik, M. Muneeb, E. Ryckeboer, S. Uvin, Z. Hens, R. Baets, Y. Shimura, F. Gencarelli, B. Vincent, R. Loo, J. Van Campenhout, L. Cerutti, J.-B. Rodriguez, E. Tourni, X. Chen, M. Nedeljkovic, G. Mashanovich, L. Shen, N. Healy, A. C. Peacock, X. Liu, R. Osgood, and W. Green, "Silicon-based heterogeneous photonic integrated circuits for the mid-infrared," Optical Materials Express **3**, 1523 (2013).

[138] S. Zlatanovic, J. S. Park, S. Moro, J. M. C. Boggio, I. B. Divliansky, N. Alic, S. Mookherjea, and S. Radic, "Mid-infrared wavelength conversion in silicon waveguides using ultracompact telecom-band-derived pump source," Nat Photon **4**, 561–564 (2010).

[139] Y.-C. Chang, V. Paeder, L. Hvozdara, J.-M. Hartmann, and H. P. Herzig, "Low-loss germanium strip waveguides on silicon for the mid-infrared," Optics Letters **37**, 2883 (2012).

[140] A. Malik, M. Muneeb, Y. Shimura, J. V. Campenhout, R. Loo, and G. Roelkens, "Germanium-on-silicon mid-infrared waveguides and Mach-Zehnder interferometers," in "2013 IEEE Photonics Conference," (2013), pp. 104–105.

[141] M. Brun, P. Labeye, G. Grand, J.-M. Hartmann, F. Boulila, M. Carras, and S. Nicoletti, "Low loss SiGe graded index waveguides for mid-IR applications," Optics Express **22**, 508 (2014).

[142] L. Carletti, P. Ma, Y. Yu, B. Luther-Davies, D. Hudson, C. Monat, R. Orobtchouk, S. Madden, D. J. Moss, M. Brun, S. Ortiz, P. Labeye, S. Nicoletti, and C. Grillet, "Nonlinear optical response of low loss silicon germanium waveguides in the mid-infrared," Optics Express **23**, 8261 (2015).

[143] L. Shen, N. Healy, C. J. Mitchell, J. S. Penades, M. Nedeljkovic, G. Z. Mashanovich, and A. C. Peacock, "Mid-infrared all-optical modulation in low-loss germanium-on-silicon waveguides," Optics Letters **40**, 268 (2015).

[144] U. Younis, S. K. Vanga, A. E.-J. Lim, P. G.-Q. Lo, A. A. Bettiol, and K.-W. Ang, "Germanium-on-SOI waveguides for mid-infrared wavelengths," Optics Express **24**, 11987 (2016).

[145] N. Singh, D. D. Hudson, and B. J. Eggleton, "Silicon-on-sapphire pillar waveguides for Mid-IR supercontinuum generation," Optics Express **23**, 17345 (2015).

[146] V. Singh, P. T. Lin, N. Patel, H. Lin, L. Li, Y. Zou, F. Deng, C. Ni, J. Hu, James Giammarco, A. P. Soliani, B. Zdyrko, I. Luzinov, S. Novak, J. Novak, Peter Wachtel, S. Danto, J. D. Musgraves, K. Richardson, L. C. Kimerling, and A. M. Agarwal, "Mid-infrared materials and devices on a Si platform for optical sensing," Sci. Technol. Adv. Mater. **15**, 014603 (2014).

[147] P. T. Lin, V. Singh, Y. Cai, L. C. Kimerling, and A. Agarwal, "Air-clad silicon pedestal structures for broadband mid-infrared microphotonics," Optics Letters **38**, 1031 (2013).

[148] Z. Cheng, X. Chen, C. Y. Wong, K. Xu, and H. K. Tsang, "Mid-infrared Suspended Membrane Waveguide and Ring Resonator on Silicon-on-Insulator," IEEE Photonics Journal **4**, 1510–1519 (2012).

[149] Y. Xia, C. Qiu, X. Zhang, W. Gao, J. Shu, and Q. Xu, "Suspended Si ring resonator for mid-IR application," Optics Letters **38**, 1122 (2013).

[150] J. Chiles, S. Khan, J. Ma, and S. Fathpour, "High-contrast, all-silicon waveguiding platform for ultra-broadband mid-infrared photonics," Applied Physics Letters **103**, 151106 (2013).

[151] J. Soler Penads, C. Alonso-Ramos, A. Z. Khokhar, M. Nedeljkovic, L. A. Boodhoo, A. Ortega-Moux, I. Molina-Fernndez, P. Cheben, and G. Z.

Mashanovich, "Suspended SOI waveguide with sub-wavelength grating cladding for mid-infrared," Optics Letters **39**, 5661 (2014).

[152] W. C. Jiang, J. Zhang, and Q. Lin, "Compact suspended silicon microring resonators with ultrahigh quality," Opt. Express, OE **22**, 1187–1192 (2014).

[153] Y. Chen, H. Lin, J. Hu, and M. Li, "Heterogeneously Integrated Silicon Photonics for the Mid-Infrared and Spectroscopic Sensing," ACS Nano **8**, 6955–6961 (2014).

[154] M. Borselli, T. J. Johnson, and O. Painter, "Measuring the role of surface chemistry in silicon microphotonics," Applied Physics Letters **88**, 131114 (2006).

[155] F. P. Payne and J. P. R. Lacey, "A theoretical analysis of scattering loss from planar optical waveguides," Opt Quant Electron **26**, 977–986 (1994).

[156] B. Kuyken, T. Ideguchi, S. Holzner, M. Yan, T. W. Hnsch, J. Van Campenhout, P. Verheyen, S. Coen, F. Leo, R. Baets, G. Roelkens, and N. Picqu, "An octave-spanning mid-infrared frequency comb generated in a silicon nanophotonic wire waveguide," Nat Commun **6**, 6310 (2015).

[157] A. B. Matsko, A. A. Savchenkov, D. Strekalov, V. S. Ilchenko, and L. Maleki, "Optical hyperparametric oscillations in a whispering-gallery-mode resonator: Threshold and phase diffusion," Phys. Rev. A **71**, 033804 (2005).

[158] F. Gholami, S. Zlatanovic, A. Simic, L. Liu, D. Borlaug, N. Alic, M. P. Nezhad, Y. Fainman, and S. Radic, "Third-order nonlinearity in silicon beyond 2350 nm," Applied Physics Letters **99**, 081102 (2011).

[159] S. Miller, A. Griffith, M. Yu, A. L. Gaeta, and M. Lipson, "Low-Loss Air-Clad Suspended Silicon Platform for Mid-Infrared Photonics," in "Conference on Lasers and Electro-Optics (2016), paper STu3Q.6," (Optical Society of America, 2016), p. STu3Q.6.

[160] J. B. Khurgin, T. H. Stievater, M. W. Pruessner, and W. S. Rabinovich, "On the origin of the second-order nonlinearity in strained SiSiN structures," J. Opt. Soc. Am. B, JOSAB **32**, 2494–2499 (2015).

[161] M. Soltani, A. Matsko, and L. Maleki, "Enabling arbitrary wavelength frequency combs on chip," Laser & Photonics Reviews **10**, 158–162 (2016).

[162] S. Kim, K. Han, C. Wang, J. A. Jaramillo-Villegas, X. Xue, Y. Xuan, A. Weiner, and M. Qi, "Frequency Comb Generation in 300 nm-Thick Si_3N_4 Concentric-Ring-Resonators," in "Advanced Photonics 2016 (IPR, NOMA, Sensors, Networks, SPPCom, SOF) (2016), paper IM2A.3," (Optical Society of America, 2016), p. IM2A.3.